

MULTI-ORGAN FINITE ELEMENT MODELING OF THE HUMAN HEART WITH  
VENTRICULAR-ARTERIAL INTERACTIONS

By

Sheikh Mohammad Shavik

A DISSERTATION

Submitted to  
Michigan State University  
in partial fulfillment of the requirements  
for the degree of

Mechanical Engineering – Doctor of Philosophy

2019

## ABSTRACT

### MULTI-ORGAN FINITE ELEMENT MODELING OF THE HUMAN HEART WITH VENTRICULAR-ARTERIAL INTERACTIONS

By

Sheikh Mohammad Shavik

Computer heart models with realistic description of cardiac geometry and muscle architecture have advanced significantly over the years. Despite these significant advancements, there are nevertheless, some unresolved issues and aspects that need improvements. The goal of this dissertation was to address some of those issues as well as to develop new computational modeling framework to understand the underlying mechanics in heart failure with preserved ejection fraction (HFpEF) and pulmonary arterial hypertension (PAH).

Clinical studies have found that global longitudinal strain is reduced in HFpEF, suggesting that LV contractility is impaired in this syndrome. This finding is, however, contradicted and confounded, respectively, by findings that end-systolic elastance ( $E_{es}$ ) and systolic blood pressure (SBP) are typically also increased in HFpEF. To reconcile these issues, we developed and validated a multiscale computational modeling framework consisting of detailed cell-based descriptors of the cross-bridge cycling against well-established organ-level physiological behaviors. This framework is then used to isolate the effects of HFpEF features in affecting systolic function metrics by quantifying the effects on  $E_{es}$  and myocardial strains due to 1) changes in LV geometry found in HFpEF patients, 2) active tension developed by the tissue ( $T_{ref}$ ), and 3) afterload. Our study suggests that it is likely that the LV contractility as indexed by the tissue's active tension is reduced in HFpEF patients.

Right ventricular assist device (RVAD) has been considered as a treatment option for the end-stage pulmonary arterial hypertension (PAH) patients, but, its effects on biventricular mechanics are, however, largely unknown. To address this issue, we developed an image-based modeling framework consisting of a biventricular finite element (FE) model that is coupled to a lumped model describing the pulmonary and systemic circulations in a closed-loop system. Our results showed that RVAD unloads the RV, improves cardiac output and increases septum curvature, which are more pronounced in the PAH patient with severe RV remodeling. These improvements, however, are also accompanied by an adverse increase in the PA pressure, suggesting that the RVAD implantation may need to be optimized depending on disease progression.

While it has long been recognized that bi-directional interaction between the heart and vasculature plays a critical role in the pathophysiological process of HFpEF and PAH, a comprehensive study of this interaction is hampered by a lack of modeling framework capable of simultaneously accommodating high-resolution models of the heart and vasculature. To address this issue, we developed a computational modeling framework that couples FE models of the LV and aorta to simulate ventricular-arterial coupling in the systemic circulation. We show that the model is able to capture the physiological behaviors in both the LV and aorta that are consistent with *in vivo* measurements. We also showed that the framework can reasonably predict the effects of changes in geometry and microstructural details the two compartments have on each other. The model is extended to accommodate a biventricular FE heart model together with FE models of the aorta and pulmonary artery to simulate the ventricular-vascular interactions in both systemic and pulmonary circulation.

# TABLE OF CONTENTS

<b>LIST OF TABLES</b> .....	vii
<b>LIST OF FIGURES</b> .....	viii
<b>CHAPTER 1</b> .....	1
<b>Introduction</b> .....	1
<b>1.1 General discussion</b> .....	1
<b>1.1.1 Anatomy of the heart</b> .....	1
<b>1.1.2 Pressure - volume relationship</b> .....	2
<b>1.1.3 Contractility, preload and afterload</b> .....	4
<b>1.2 Background of the theses</b> .....	6
<b>1.2.1 Multiscale validation of detailed cross-bridge cycling model</b> .....	7
<b>1.2.2 Understanding pathophysiological mechanism in heart failure with preserved ejection fraction (HFpEF)</b> .....	8
<b>1.2.3 Image-based biventricular model of pulmonary arterial hypertension (PAH)</b> .....	9
<b>1.2.4 Modeling framework with bidirectional ventricular-vascular interactions</b> .....	11
<b>1.3 Specific aims</b> .....	12
<b>CHAPTER 2</b> .....	14
<b>Organ - level validation of a left ventricular finite element model with detailed cross-bridge cycling descriptor</b> .....	14
<b>2.1 Introduction</b> .....	14
<b>2.2 Methods</b> .....	15
<b>2.2.1 Mechanical description of the left ventricle</b> .....	15
<b>2.2.2 Closed-loop circulatory model</b> .....	18
<b>2.2.3 End-systolic and end-diastolic pressure-volume relationships</b> .....	20
<b>2.2.4 Calculation of myocardial oxygen consumption</b> .....	22
<b>2.2.5 Calculation of myocardial strain</b> .....	22
<b>2.2.6 Calculation of left ventricular torsion</b> .....	23
<b>2.3 Results</b> .....	24
<b>2.3.1 Isometric twitch behavior</b> .....	24
<b>2.3.2 Pressure-volume loops</b> .....	25
<b>2.3.3 MVO<sub>2</sub>-PVA relationships</b> .....	27
<b>2.3.4 Myocardial strain</b> .....	29
<b>2.3.5 LV torsion</b> .....	32
<b>2.4 Discussion</b> .....	34
<b>2.4.1 Limitations</b> .....	37

<b>CHAPTER 3</b> .....	38
<b>Computational investigation of the pathophysiological mechanisms in heart failure with preserved ejection fraction (HFpEF)</b> .....	38
<b>3.1 Introduction</b> .....	38
<b>3.2 Methods</b> .....	39
<b>3.2.1 Computational modeling framework</b> .....	39
<b>3.2.2 Left ventricular geometry and boundary conditions</b> .....	39
<b>3.2.3 Simulation cases</b> .....	40
<b>3.2.4 Analysis of pressure-volume loops and strains</b> .....	42
<b>3.3 Results</b> .....	43
<b>3.3.1 Effects of changes in geometry, passive stiffness and preload</b> .....	43
<b>3.3.2 Effects of changes in active tension</b> .....	45
<b>3.3.3 Effects of changes in afterload resistance</b> .....	46
<b>3.3.4 Effects of simultaneous changes of both peripheral resistance and active tension</b> .....	47
<b>3.3.5 Comparison of geometry, hemodynamics and strains with clinical measurements</b> .....	48
<b>3.4 Discussion</b> .....	51
<b>3.4.1 Limitations</b> .....	54
<b>CHAPTER 4</b> .....	55
<b>Image based biventricular modeling framework of pulmonary arterial hypertension (PAH)</b> .....	55
.....	55
<b>4.1 Introduction</b> .....	55
<b>4.2 Methods</b> .....	56
<b>4.2.1 Image and data acquisition</b> .....	56
<b>4.2.2 Biventricular geometry and microstructure</b> .....	57
<b>4.2.3 Closed-loop circulatory model</b> .....	58
<b>4.2.4 Finite element formulation</b> .....	63
<b>4.2.5 Mechanical behavior of the cardiac tissue</b> .....	65
<b>4.2.6 Model parameterization and simulation of the cardiac cycles</b> .....	67
<b>4.2.7 Post processing of the septum curvature</b> .....	68
<b>4.3 Results</b> .....	69
<b>4.3.1 Comparison between simulations and measurements</b> .....	69
<b>4.3.2 Effect of RVAD on hemodynamics</b> .....	71
<b>4.3.3 Effect of RVAD on septum curvature</b> .....	73
<b>4.3.4 Effect of RVAD on myofiber stress</b> .....	73
<b>4.4 Discussion</b> .....	75
<b>4.4.1 Limitations</b> .....	78
<b>CHAPTER 5</b> .....	80
<b>Multi-organ finite element model for simulating ventricular-vascular interaction</b> .....	80
<b>5.1 Introduction</b> .....	80

<b>5.2 Methods</b> .....	81
<b>5.2.1 Closed-loop systemic circulatory model</b> .....	81
<b>5.2.2 Finite element formulation of the left ventricle and aorta</b> .....	84
<b>5.2.3 Geometry and microstructure of the LV</b> .....	86
<b>5.2.4 Constitutive law of the LV</b> .....	87
<b>5.2.5 Geometry and microstructure of the aorta</b> .....	89
<b>5.2.6 Constitutive law of the aorta</b> .....	89
<b>5.3 Results</b> .....	92
<b>5.3.1 Effect of a change in aorta wall thickness</b> .....	94
<b>5.3.2 Effect of changes in mass fractions of the aorta constituents</b> .....	96
<b>5.3.3 Effects of a change in LV contractility</b> .....	100
<b>5.3.4 Effects of a change in LV passive stiffness</b> .....	100
<b>5.4 Discussion</b> .....	100
<b>5.4.1 Limitations</b> .....	104
<b>5.5 Extension to biventricular model with ventricular-vascular interaction</b> .....	105
<b>5.5.1 Methods</b> .....	106
<b>5.5.2 Results</b> .....	108
<b>5.5.3 Future work</b> .....	109
 <b>CHAPTER 6</b> .....	 110
<b>Conclusions</b> .....	110
 <b>BIBLIOGRAPHY</b> .....	 112

## LIST OF TABLES

<b>Table 2.1.</b> Modified parameters of the Rice model <sup>133</sup> .....	17
<b>Table 2.2.</b> Modified parameters of the cellular electrophysiology model <sup>173</sup> which result change in the contractility .....	17
<b>Table 2.3.</b> Normal parameter values of the circulatory model.....	20
<b>Table 2.4.</b> Parameters of time varying elastance model for left atrium .....	20
<b>Table 2.5.</b> Parameters associated with ESPVR and EDPVR as found by the regression analysis .....	25
<b>Table 3.1.</b> Simulation cases in this study .....	41
<b>Table 3.2.</b> Left ventricular geometry at end-diastole .....	44
<b>Table 3.3.</b> Parameters related to ESPVR and EDPVR calculated by regression analysis .....	44
<b>Table 4.1.</b> Characteristics of the normal and PAH patients .....	57
<b>Table 4.2.</b> Model parameters for Normal and PAH cases.....	68
<b>Table 5.1.</b> Parameters of time varying elastance model for the left atrium .....	84
<b>Table 5.2.</b> Parameters of the closed loop lumped parameter circulatory framework.....	84
<b>Table 5.3.</b> Parameters of the LV model .....	89
<b>Table 5.4.</b> Parameters of the aorta model.....	92
<b>Table 5.5.</b> Mass fractions of the aorta constituents for different cases investigated in the study (For collagen fibers, the distribution of mass in four collagen fiber families was kept the same, i.e., $\phi_1 = 0.1\phi_c$ , $\phi_2 = 0.1\phi_c$ , $\phi_3 = 0.4\phi_c$ , $\phi_4 = 0.4\phi_c$ for all cases).....	92

## LIST OF FIGURES

<b>Figure 1.1.</b> Structure of the heart, and course of blood flow through the heart chambers and heart valves. Adapted from Guyton and Hall <sup>62</sup> .....	2
<b>Figure 1.2.</b> (A) A typical pressure – volume (PV) loop, (B) PV loop with identifiable physiological parameters, and (C) PV loop with ESPVR and EDPVR. Adapted from Burkhoff <sup>27</sup> .....	3
<b>Figure 1.3.</b> Effect of change in (A) contractility, (B) preload, and (C) afterload on PV loop. Adapted from Burkhoff <sup>27</sup> .....	5
<b>Figure 2.1.</b> (A) Model schematic showing the coupling of LV FE model to a closed-loop lumped parameter circulatory model, (B) Schematic showing the calculation of pressure-volume area (PVA), (C) Schematic showing the definition of LV torsion. ....	21
<b>Figure 2.2.</b> Isometric twitch profiles for different contractility cases. Force values were normalized by the maximum force of the baseline contractility case.....	24
<b>Figure 2.3.</b> Effects on pressure-volume loop by due to a change in (A) preload at a constant afterload, (B) afterload at a constant preload, (C) contractility (solid) c.f. baseline (dotted), Values indicate corresponding ejection fraction. ....	26
<b>Figure 2.4.</b> Myocardial oxygen consumption ( $MVO_2$ ) vs. pressure-volume area (PVA) relationship predicted by the model. Data points are calculated at different preload, afterload and contractility. ....	27
<b>Figure 2.5.</b> Longitudinal (first column), circumferential (second column), radial (third column) strain-time profiles. (A) Comparison of the model predictions with previously published <i>in vivo</i> 2D STE measurements <sup>37,52,65</sup> . Strain-time profiles predicted by the model with, (B) different preload (with constant afterload), (C) different afterload (with constant preload) and, (D) different contractility for a representative case (case P2 shown in Figure 2.3A and 2.3C). ....	28
<b>Figure 2.6.</b> Regional variation of (A) longitudinal, (B) circumferential and (C) radial strain profiles for a specific case corresponding with normal hemodynamic conditions (case P2, Figure 2.3A). ....	30
<b>Figure 2.7.</b> (A) Longitudinal, (B) circumferential, (C) radial strain profiles calculated using different strain definitions. ....	31

<b>Figure 2.8.</b> Left ventricular torsion for varying (A) preload, (B) afterload and (C) contractility (case P2 in Figure 2.3A and 2.3C) compared with echocardiographic measurements by Mondillo <i>et al.</i> <sup>116</sup> .....	33
<b>Figure 3.1.</b> (A) Schematic of the computational framework consisting of a LV FE model coupled to a closed loop lumped parameter circulatory model. For a detailed description of the model parameters, refer to Shavik <i>et al.</i> <sup>144</sup> , (B) Schematic of the normal and HFpEF unloaded LV geometry (all dimensions are in cm).....	40
<b>Figure 3.2.</b> (A) PV loops (numbers with percentage indicate EF), (B) global longitudinal, (C) circumferential and (D) radial strains for <i>normal</i> , <i>G</i> and <i>GSS</i> cases. Refer to Table 3.1 for description of the simulation cases. Case <i>GSS</i> has same geometry, active tension and afterload resistance as case <i>G</i> . Only passive stiffness <i>C</i> was decreased in case <i>GSS</i> (120Pa in case <i>GSS</i> vs. 155Pa in case <i>G</i> ) to determine its effect on PV loop and strains.....	45
<b>Figure 3.3.</b> (A) PV loops (numbers with percentage indicate EF), (B) global longitudinal, (C) circumferential and (D) radial strain waveforms for cases <i>GC1</i> , <i>GC2</i> and <i>GC3</i> when $T_{ref}$ was decreased by 30%, 50% and 70%, respectively. Dotted lines in (A) denote PV loops (at different preload) used for computing $E_{es}$ . .....	46
<b>Figure 3.4.</b> (A) PV loops (numbers with percentage indicate EF), (B) longitudinal, (C) circumferential and (D) radial strain for cases <i>GA1</i> , <i>GA2</i> and <i>GA3</i> when $R_{per}$ was increased by 100%, 150% and 200%, respectively. ....	47
<b>Figure 3.5.</b> Comparison of (A) PV loops (numbers with percentage indicate EF), (B) longitudinal, (C) circumferential and (D) radial strain of the <i>GCA</i> case (30% decrease of $T_{ref}$ + 15% increase in $R_{per}$ ) with cases <i>GC1</i> (30% decrease in $T_{ref}$ ), case <i>G</i> and <i>normal</i> . ....	48
<b>Figure 3.6.</b> Comparison of model predictions of EDV, ESV and EF from all the simulation cases with clinical measurements. <sup>93,112</sup> .....	49
<b>Figure 3.7.</b> Comparison of model predictions of SBP and DBP in all the simulation cases with clinical measurements. <sup>93,112</sup> .....	50
<b>Figure 3.8.</b> Comparison of model predictions of peak longitudinal strains with clinical measurements. <sup>93,118</sup> .....	50
<b>Figure 4.1.</b> Left: Biventricular FE geometry reconstructed from MR images with LVFW (red), septum (green), and RVFW (blue) material regions. Right: Unloaded FE geometry of normal, PAHN and PAHR cases respectively. ....	58

**Figure 4.2.** (A) Schematic of the coupled biventricular FE - closed loop modeling framework, (B) pump characteristics curve used to model the RVAD, (C) schematic showing the contours used to calculate the septum and LVFW local curvature in the LV endocardium in Cartesian coordinate.59

**Figure 4.3.** (A) Scatter plot of the simulated vs. measured volume (left) and pressure (right) at all cardiac time points for the three cases. A  $y = x$  line is also plotted to show the zero-error reference. (B) Measurements and model predictions of LV and RV PV loops (first row), volume waveforms (2<sup>nd</sup> row) and pressure waveforms (3<sup>rd</sup> row) for the normal, PAH patient with severe RV remodeling (PAHR) and PAH patient with normal RV (PAHN).....70

**Figure 4.4.** (A) RV, (B) LV PV loops, (C) RV, PA and RA pressure waveforms, (D) LV, SA and LA pressure waveforms for the PAHR and PAHN cases with different RVAD speed. Scattered points show the measurements.....72

**Figure 4.5.** (A) LVFW, septum and LV curvature for normal, PAHR and PAHN cases, (B) comparison of the normalized septum curvature between normal, PAHR and PAHN cases (left), normalized septum curvature for PAHR (middle) and PAHN (right) cases with different RVAD speeds, (C) mid-ventricular short-axis slice of the PAHR (left) and PAHN (right) cases showing the motion of septal wall with RVAD over a cardiac cycle. ....74

**Figure 4.6.** Average LVFW (left), Septum (middle) and RVFW (right) fiber stress (A) in the normal, PAHR and PAHN. (B) PAHR case with different RVAD speed. (C) PAHN case with different RVAD speed. (D) Myofiber stress shown by color map in long-axis slices at mid-ventricular level in Normal, PAHR and PAHN cases at end-systole. ....75

**Figure 5.1.** (A) Schematic diagram of the ventricular-arterial modeling framework, (B) unloaded aorta geometry with  $e_k$  ( $k = 1 - 4$ ) showing the directions of the four collagen fiber families, (C) unloaded LV geometry with fiber directions varying from  $60^\circ$  at the endocardium to  $-60^\circ$  at the epicardium wall (all dimensions are in cm).....81

**Figure 5.2.** Effects of a change in aorta wall thickness on (A) its *ex-vivo* pressure–diameter relationship, (B) LV pressure–volume loop and (C) pressure - diameter both operating *in-vivo*. 93

**Figure 5.3.** Pressure in LV, aorta and LA during cardiac cycle with increasing aorta wall thickness in ascending order from the Baseline to T<sub>3</sub> case.....94

**Figure 5.4.** Effects of active tone and aorta constituent mass fractions on (A) its *ex-vivo* pressure–diameter relationship, (B) LV pressure–volume loop and (C) pressure - diameter both operating *in-vivo*. (Refer to Table 5.5 for cases).....95

**Figure 5.5.** Pressure in LV, aorta and LA during cardiac cycle for different aorta constituent mass fractions and active tone. ....96

**Figure 5.6.** Effects of changes in LV contractility on (A) pressure-volume loop, (B) pressure waveform in LV, aorta and LA during cardiac cycle, and (C) peak stress in aorta. Contractility decreases in the following order: Baseline, C<sub>1</sub>, C<sub>2</sub>. ....98

**Figure 5.7.** Effects of changes in LV passive stiffness on (A) pressure-volume loop, (B) pressure waveform in LV, aorta and LA during cardiac cycle, and (C) peak stress in aorta. Passive stiffness increases in the following order: Baseline, P<sub>1</sub>, P<sub>2</sub>. ....99

**Fig. 5.8.** Schematic of the ventricular-vascular coupling modeling framework. Model consists of image-based high resolution biventricular, aorta and pulmonary artery FE models that are coupled to closed-loop lumped parameter model in systemic and pulmonary circulation. ....106

**Fig. 5.9.** (A) LV, (B) RV PV loops, (C) LV, aorta and LA pressure waveforms, and (D) RV, PA and RA pressure waveforms as predicted by the model. ....108

# CHAPTER 1

## Introduction

### 1.1 General discussion

#### 1.1.1 Anatomy of the heart

The heart is a muscular organ that pumps blood through the systemic and pulmonary vascular systems. The primary job of the heart and vasculature is to maintain an adequate supply of oxygen and nutrients to all of the tissues of the body under a wide range of operating conditions. The normal adult human heart is divided into four distinct muscular chambers, two atria and two ventricles, which are arranged to form functionally separate left and right heart pumps (**Fig. 1.1**). The left heart is composed of the left atrium and left ventricle which pumps blood from the pulmonary veins to the aorta. The human left ventricle has an axisymmetric, truncated ellipsoid shape with approximately 1 cm wall thickness. The right heart consists of right atrium and right ventricle that pumps blood from the vena cava to the pulmonary arteries. Less powerful than the left ventricle, the right ventricle is crescent-shaped and has a thinner wall. The heart wall is composed of myofibers that are arranged in a highly organized manner. The local myofiber orientation varies along the transmural direction from the inner (endocardium) to the outer (epicardium) wall, and is predominantly circumferential at the mid-wall. The tricuspid valve in the right heart and the mitral valve in the left heart separate the atria from their corresponding ventricle, and are arranged in a manner to ensure one-way flow through the heart and prohibits backward flow during the contraction of the ventricles. The aortic and pulmonary valve separate each ventricle from its arterial connection and ensure unidirectional flow by preventing blood from flowing from the artery back into the ventricle. The cardiovascular system is closed-loop.

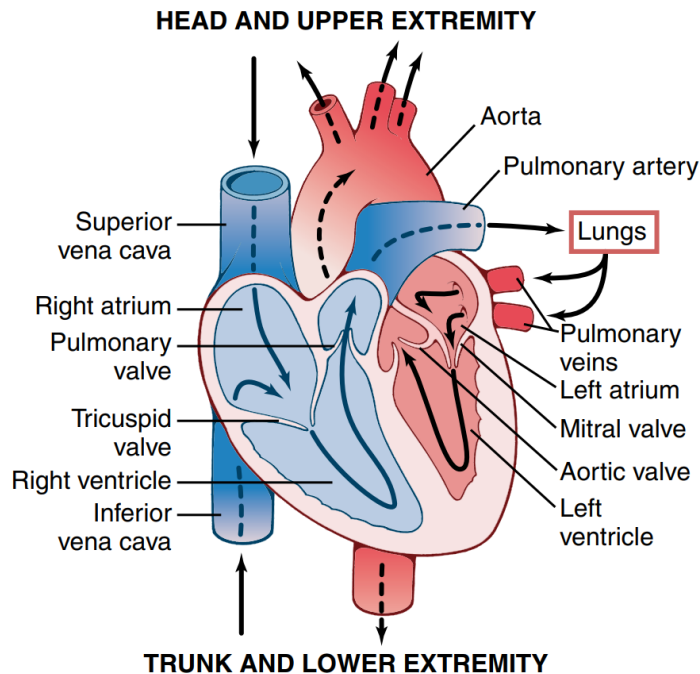


**Figure 1.1.** Structure of the heart, and course of blood flow through the heart chambers and heart valves. Adapted from Guyton and Hall<sup>62</sup>.

### 1.1.2 Pressure - volume relationship

The cardiac cycle is divided into two major phases, systole and diastole. In systole the ventricular muscles transform from its totally relaxed state to the point of maximal mechanical activation or force. On the other hand, diastole is the period of time during which the muscle relaxes from the end-systolic (maximally activated) state back towards its resting state. In each cardiac cycle, the ventricular wall contracts and relaxes. Correspondingly, mechanical properties of the ventricle are time-varying during a cardiac cycle. The time-varying mechanical properties are related to the pressure-volume relationship of the ventricle over the cardiac cycle (**Fig. 1.2A**), which is a convenient way to interpret the ventricular function.

As time proceeds in cardiac cycle, the PV points go around the loop in a counter clockwise direction. Point **A** denotes the end of diastole or, start of the systole. Using this point as a reference,

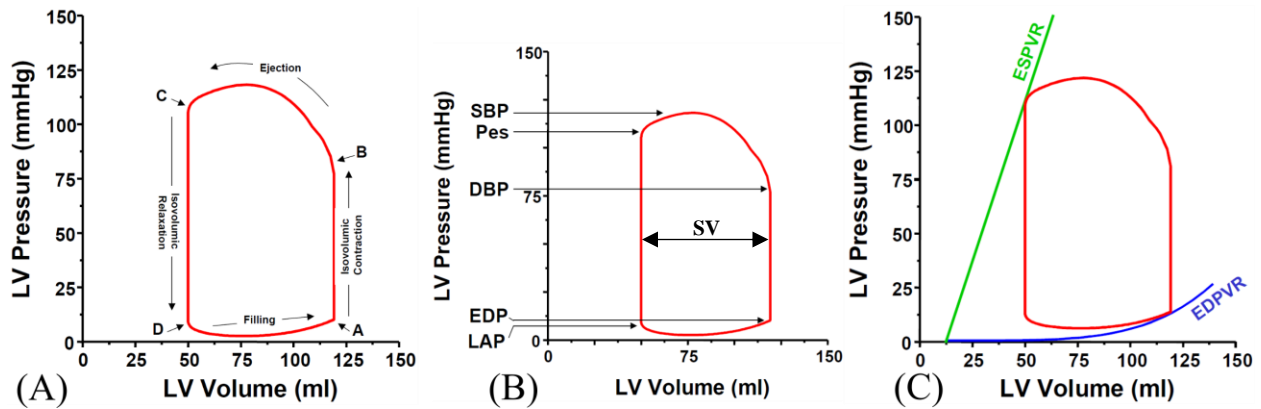


**Figure 1.2.** (A) A typical pressure – volume (PV) loop, (B) PV loop with identifiable physiological parameters, and (C) PV loop with ESPVR and EDPVR. Adapted from Burkhoff<sup>27</sup>.

pressure rises but volume stays the same in the first part of the cycle, which is known as the isovolumic contraction phase where the ventricle contracts with both valves remaining closed. Ultimately ventricular pressure rises above the aortic pressure, the aortic valve opens (**B**), ejection begins and volume starts to decrease during the ejection phase. After the ventricle reaches its maximum activated state (**C**, upper left corner of PV loop), the ventricular pressure falls below aortic pressure, following which the aortic valve closes and isovolumic relaxation commences. Finally, filling begins when the mitral valve opens (**D**, bottom left corner) and ceases when the valve closes (**A**) and the cycle repeats.

Several parameters and variables of physiologic importance can be obtained from analysis of the PV loop (**Fig 1.2B**). Specifically, the maximum volume of the cardiac cycle is referred as the end-diastolic volume (EDV), which can be readily determined from point **A** (Fig. 1.2A). Also, the minimum volume known as the end-systolic volume (ESV) can be retrieved from point **D**, which is the ventricular volume at the end of the ejection phase. The difference between EDV and ESV represents the amount of blood ejected during the cardiac cycle and is referred as the stroke volume (SV). Near the top right of the loop we can identify the point at which the ventricle begins to eject (the point at which ventricular pressure just exceeds aortic pressure and volume starts to

decrease). This pressure therefore reflects the pressure existing in the aorta at the onset of ejection and is called the diastolic blood pressure (DBP). During the ejection phase, aortic and ventricular pressures are essentially equal. Therefore, the point of greatest pressure on the loop also represents the greatest pressure in the aorta which is called the systolic blood pressure (SBP). The end-systolic pressure ( $P_{es}$ ) is identified as the pressure of the left upper corner of the loop. The pressure of the point at the bottom right corner (point **D** in Fig. 1.2A) of the loop is the pressure in the ventricle at the end of the cardiac cycle and is called the end-diastolic pressure (EDP).

Ventricular filling occurs along the end-diastolic pressure-volume relationship (EDPVR), or passive filling curve for the ventricle. The curvature of this line is determined by the mechanical properties of the muscle as well as the structural and geometrical features of the ventricle (e.g., wall thickness). The maximal pressure that can be developed by the ventricle is defined by the end-systolic pressure-volume relationship (ESPVR). Example of a PV loop bounded by the ESPVR and EDPVR are shown in **Fig. 1.2C**. The upper left-hand corner (end-systolic point) of each loop falls on the ESPVR, while the bottom right part of the loop falls on the EDPVR. The slope of the ESPVR is known as the end-systolic elastance,  $E_{es}$  which is a measure of the ventricular contractility.

### **1.1.3 Contractility, preload and afterload**

Contractility, preload and afterload are three important concepts that are related to the ventricular function. Contractility refers to the intrinsic strength of the ventricle or cardiac muscle. It represents the intrinsic ability of the cardiac muscle to generate force that is independent of external loads or stretch. Myocardial contractility results from the excitation-contraction coupling, the sequence of events that lead to myocardial contraction triggered by electrical depolarization of the cells. Myocardial contractility can be changed by altering one or combination of events (for

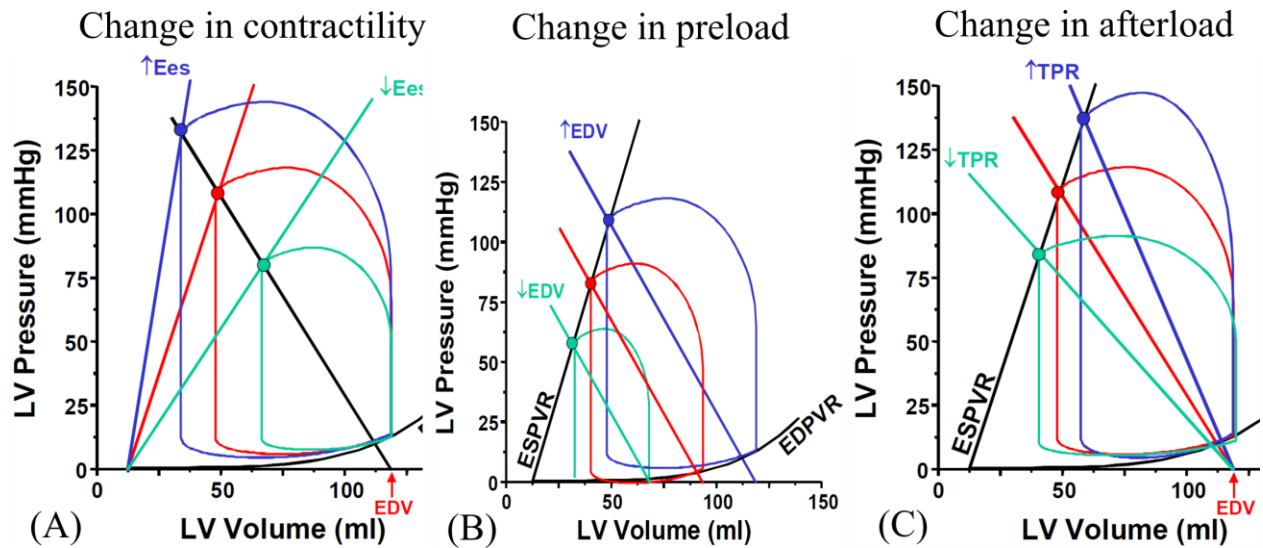


**Figure 1.3.** Effect of change in (A) contractility, (B) preload, and (C) afterload on PV loop. Adapted from Burkhoff<sup>27</sup>.

instance, the amount of calcium released, number of myofilaments available to participate in the contraction process, etc.) related to the excitation-contraction coupling process. The end systolic elastance  $E_{es}$  is considered to be an index of contractility as it varies with the ventricular contractility (**Fig. 1.3A**) but is not affected by the changes in the arterial system (preload and afterload).

Preload is the hemodynamic load or stretch on the myocardial wall at the end of diastole just before contraction begins. Ventricular preload can be estimated by measuring 1) EDP, 2) EDV, 3) wall stress at end-diastole and 4) end-diastolic sarcomere length. In the clinical setting, EDP probably provides the most meaningful measure of preload in the ventricle which is assessed by measuring the pulmonary capillary wedge pressure (PCWP) using a catheter that is placed through the right ventricle into the pulmonary artery. A change in preload influences the SV and pressure but end systolic elastance  $E_{es}$  remains same (**Fig. 1.3B**).

Afterload is the hydraulic load imposed on the ventricle during ejection. This load is usually imposed on the heart by the arterial system. There are several measures of afterload that

are used in different settings, namely, 1) aortic pressure, 2) total peripheral resistance (TPR), 3) arterial impedance and, 4) myocardial peak wall stress. The change in afterload also influences the SV and pressure of the ventricle but the Ees remains unchanged (**Fig. 1.3C**).

## **1.2 Background of the theses**

Heart disease is one of the major causes of the death in the United States. According to Centers for Disease Control and Prevention (CDC), about 610,000 people die every year in heart disease in the United States, that is 1 in every 4 deaths<sup>32</sup>. Computational models are used increasingly to better understand the mechanics of the normal as well as diseased heart. Specifically, finite element (FE) modeling of the intact heart having realistic geometry and architectural assembly of cardiac muscle descriptor has advanced significantly over the years. Such models are now capable of describing the coupling between electrophysiology and mechanics<sup>60,85,156</sup>, as well as long-term remodeling of the heart<sup>49,84,100,101</sup>. Although animal and clinical studies were predominantly used to understand the mechanisms and effects of novel treatments and diseases in the past, computer models are increasingly used to elucidate the pathophysiology of heart diseases and mechanisms of treatments such as cardiac resynchronization therapy<sup>68,81</sup> and surgical ventricular restoration<sup>103</sup>. Because of their versatility and low cost, computational models are increasingly used to supplement the animal and clinical studies. Often only a limited number of parameters can be manipulated in animal studies without affecting the others, which makes it very difficult to distinguish between the contributions of different factors that may affect the pathophysiology of heart diseases. On the other hand, computer heart models that are validated based on physiological principles are reproducible and allow one to investigate the isolated effects of each parameter without the confounding effects of others<sup>16,82</sup>. However, despite the continuous efforts that have substantially improved the computational heart models over the years, much remain to be done.

There are some unresolved issues and aspects that need improvements. Moreover, accurate heart models could be very useful to address important unanswered questions about human heart diseases that cannot be resolved through experimentation. We have identified some of those issues, which are discussed in detail in the subsequent sections.

### **1.2.1 Multiscale validation of detailed cross-bridge cycling model**

Accurate description of ventricular active contraction behavior is particularly important in ensuring that the model predictions are consistent with well-established physiological principles at the whole heart level. Available contraction models vary in sophistication and detail depending on the number of intermediate cross-bridge states used in dynamically modeling muscle fiber shortening. Such descriptions range from being purely phenomenological<sup>56,83</sup> that do not model the different states of the cross-bridge cycle, to detailed models<sup>26,71,133</sup> that describe some (if not all) the states of the cross-bridge cycle. For the latter case, models were usually developed based on small-sample measurements of force-calcium and force-velocity relationships under different loading conditions using multicellular (papillary or trabecular muscles), intact single-cell or skinned fiber preparations. Although able to recapitulate key features found in these small-scale measurements, it is unknown if these descriptors, when scaled up with realistic ventricular geometry and muscle fiber organization in the ventricular wall, can reproduce key features of measurements made at the whole organ level. Correspondingly, there exists a question as to whether the gap between sub-cellular and tissue-organ level phenomena can be bridged by simply applying these detailed cross-bridge models to describe the mechanical behavior of the whole heart.

For instance, a widely used detailed cross-bridge cycling descriptor developed by Rice *et al.*<sup>133</sup> was originally calibrated using experimental data from rats. This model has been adopted

subsequently in many multiscale computational frameworks that were used to investigate diseases and treatments in relation to data acquired from other species, such as humans<sup>1-3,67</sup> and canine<sup>34,60,68,105</sup>. While model predictions using this cross-bridge descriptor have been compared to some myocardial strain and single pressure-volume (PV) loop measurements<sup>31,60,160</sup> in the past, there are no existing studies investigating whether the model can reproduce features found in an analysis of human heart behavior in the face of varying preload and afterload, such as a linear, relatively load-independent end-systolic pressure-volume relationship (ESPVR). It is also not known whether the Rice cross-bridge descriptor, when scaled up to organ-level, is able to reproduce the experimentally observed linear relationship between total myocardial oxygen consumption (MVO<sub>2</sub>) and total mechanical work (indexed by the pressure-volume area, PVA).

### **1.2.2 Understanding pathophysiological mechanism in heart failure with preserved ejection fraction (HFpEF)**

Heart failure with preserved ejection fraction (HFpEF) is a syndrome accounting for about one-half of all chronic heart failure (HF) patients.<sup>18,123</sup> The incidence and prevalence of HFpEF are increasing at a rate of about 1%/year,<sup>23,123</sup> with mortality rates comparable to HF with reduced ejection fraction (HFrEF).<sup>123,151,161</sup> Compared to HFrEF, patients diagnosed with HFpEF are older and have a higher prevalence rate of hypertension.<sup>123</sup> While new therapies have been proposed,<sup>11,107,150,158,175</sup> no proven treatment option currently exists for HFpEF patients.<sup>126,135</sup>

Because of the presence of many pathological features impairing LV filling<sup>140</sup> (e.g., slow LV relaxation,<sup>178</sup> cardiomyocyte stiffening,<sup>178</sup> concentric hypertrophy<sup>166</sup>), diastolic dysfunction was initially believed to be the sole mechanism underlying HFpEF, which was previously referred to as diastolic HF.<sup>23,179</sup> Mounting evidence, however, has suggested that myocardial contractility in HFpEF patients may also be impaired, thus calling into question the original notion that systolic

function is preserved in this syndrome.<sup>93,118,142,180</sup> However, seemingly contradictory observations have been challenging to reconcile and resolve the question of myocardial contractility in HFpEF. On the one hand, studies have shown that end-systolic elastance ( $E_{es}$ ) and LV ejection fraction (EF) are normal or increased in HFpEF (suggesting preserved or increased global *ventricular* contractility).<sup>22,76</sup> On the other hand, these hearts exhibit decreased global longitudinal strain, suggesting decreased *myocardial* contractility. These seemingly conflicting observations (normal or increased chamber contractility but decreased myocardial motion) are difficult to resolve purely through basic or clinical experimental studies. This difficulty arises because of the differing influences of increased vascular resistance (afterload), altered LV geometry, increased LV mass (all encountered in HFpEF patients) on longitudinal strain, which potentially confound the link between longitudinal strain and myocardial contractility.

Computational modeling has the inherent advantage to isolate factors affecting LV function and motion in HFpEF patients so as to clarify their individual role(s) and contribution(s). There are, however, only a few prior studies that have explored the use of computational modeling to understand ventricular mechanics in HFpEF.<sup>3,36,45,109</sup> Seemingly conflicting observations and multiple confounding factors as described above, to the best of our knowledge, have not been resolved in any of those studies.

### **1.2.3 Image based biventricular model of pulmonary arterial hypertension (PAH)**

Pulmonary arterial hypertension (PAH) is a cardio-pulmonary disease that is characterized by an abnormally elevated pulmonary artery (PA) pressure ( $> 25$  mmHg), which can be due to idiopathic reasons or caused by other conditions (e.g., presence of ventricular septal defect). Without treatment, PAH progresses rapidly and adversely affects the right ventricular (RV) function, eventually leading to right heart failure and death<sup>69</sup>. There are currently no effective treatments for

PAH, and existing therapies for this disease have been mostly palliative<sup>72</sup>. Given the success of left ventricular assist device (LVAD) as a treatment for left heart failure, right ventricular assist device (RVAD) is recently proposed as a therapeutic option for PAH patients, especially when the disease is refractory to vasodilator therapy<sup>128</sup>. Unlike its LVAD counterpart, however, the effects of this device on RV mechanics are not well understood. Moreover, our understanding on the effects of PAH on RV mechanics in humans is also lacking as most patient studies of this disease are based largely on measuring regional myocardial deformation or kinematics from clinical images<sup>42</sup>.

Computational models are increasingly developed to improve our understanding on the effects of PAH on RV mechanics, although the number of models is significantly lesser compared to those developed to study left ventricular (LV) mechanics<sup>33,102,144,167</sup>. While able to produce insights of PAH, existing computational heart models developed to investigate this disease currently suffer from one or more of the following limitations: (a) not calibrated based on human data<sup>13,51</sup>, (b) focusing only on RV passive mechanics and ignore active mechanics<sup>12</sup>, and (c) do not couple both systemic and pulmonary circulatory systems<sup>13,51,174</sup>. Specifically, the latter limitation places a restriction on our ability to fully assess how alterations in the pulmonary circulation consisting of the RV, such as by RVAD implantation, can impact the systemic circulation (including LV mechanics), and vice versa. On the other hand, while it is possible to use a simplified lumped circulatory modeling framework<sup>128</sup> to simulate the effects and interactions of RVAD with the systemic and pulmonary circulations in PAH, this approach cannot be used to quantify the effects of RVAD and its different operating configurations on important physiological quantities such as septal curvature and RV myofiber stress, which is directly related to oxygen consumption<sup>152</sup>.

#### **1.2.4 Modeling framework with bidirectional ventricular-vascular interaction**

The heart and vasculature are both key components of the cardiovascular system and they operate in tandem to accomplish the very important task of delivering oxygen and nutrients to the human body. Physiological adaptation, deterioration, and/or malfunctioning of one component often affects the operation of the other. Indeed, optimal ventricular-arterial interaction (or coupling) is critical to the normal functioning of the cardiovascular system. Any deviations from optimal ventricular-arterial interaction in the cardiovascular system (as indexed by the ratio between arterial stiffness and ventricular elastance) are usually associated with heart diseases<sup>21</sup>. For instance, in the systemic circulatory system, heart failure with preserved ejection fraction (HFpEF) has been associated with a progressively impaired ventricular-arterial interaction between the left ventricle (LV) and the systemic arteries<sup>21,76</sup>. Ventricular-arterial interaction is also reflected at the microstructural level. In particular, remodeling of the vasculature found in these diseases (e.g., smooth muscle hypertrophy/ proliferation and deposition of the collagen)<sup>48,146</sup> are often accompanied by similar remodeling in the heart (e.g., myocyte hypertrophy and cardiac fibrosis)<sup>64,129,154</sup>.

Computational modeling is particularly useful for understanding ventricular-arterial interaction, especially when there are potentially many parameters that can affect this interaction bi-directionally. While ventricular-arterial interactions may be described using electrical analog (or lumped parameter) models of the cardiovascular system<sup>10,148</sup>, the heart and vasculature in such models are represented using highly idealized electrical circuit elements such as resistor, capacitor and voltage generator. It is difficult, if not impossible, to separate or distinguish between geometrical, material, and microstructural changes from the parameters of these electrical elements. Previous finite element (FE) modeling efforts of the cardiovascular system, however,

have focused on either the heart or the vasculature. Specifically, FE models of the heart were developed either in isolation<sup>44,46,103,172</sup>, or coupled to an electrical analog of the circulatory system in open<sup>101,160,164,168,174</sup> or closed loop fashions<sup>83,145</sup>. In an open-loop circulatory modeling framework, the FE ventricular model is generally coupled to a Windkessel model via outlet boundary conditions to simulate the ejection of blood, while the filling and isovolumic phases are, respectively, simulated by increasing and constraining the ventricular cavity volume. Parameters in the modeling framework are then adjusted so that the four distinct cardiac phases form a closed pressure-volume loop. On the other hand, coupling the FE ventricular model to a closed loop circulatory modeling framework is (arguably) more physical since the total blood volume is naturally conserved in the cardiovascular system. Simulation of multiple cardiac cycles is required, however, to obtain a steady state solution. Conversely, FE models of the vasculature were developed either in isolation<sup>66,177</sup> or coupled to simplified representation of the heart based on a time-varying elastance function<sup>88,99</sup>. Although able to describe the heart or vasculature in greater details, these FE modeling frameworks cannot be used to simulate detailed bidirectional ventricular-arterial interactions e.g., how changes in the vasculature mechanical properties affect the deformation and function of the heart and vice versa. Therefore, a modeling framework with the ability of describing the bidirectional ventricular-vascular coupling could be very useful to elucidate the detailed bidirectional interactions between the vasculature and heart.

### **1.3 Specific aims**

In this dissertation, we seek to overcome the issues and limitations discussed earlier, namely,

1. We have validated a detailed cross-bridge cycling descriptor against well-established organ-level physiological behaviors using a left ventricular finite element modeling framework. The model is discussed in detail in **chapter 2**.

2. We have used our methodically validated model discussed in **chapter 2** to understand the pathophysiological mechanisms that affect systolic functions in Heart Failure with Preserved Ejection Fraction (HFpEF) patients as discussed in detail in **chapter 3**.
3. We have developed an image based biventricular FE modeling framework that is coupled to a lumped parameter model describing both the pulmonary and systemic circulations in a closed-loop system. We have calibrated this model against measurements from a normal subject as well as pulmonary arterial hypertension (PAH) patients as well as investigated the effects of right ventricular assist device (RVAD) on ventricular hemodynamics and mechanics in PAH patients. The methodology and results are discussed in **chapter 4**.
4. We have formulated a modeling framework accommodating the bidirectional ventricular-arterial interactions in systemic circulation. The model has been calibrated to reproduce the physiological behavior of normal human and able to successfully simulate the bidirectional changes in the functional behaviors of both left ventricle (LV) and aorta when geometrical or, material parameter(s) were changed that are consistent with experimental observations. The model is discussed in **chapter 5**. This model is extended to accommodate a biventricular FE heart model together with FE models of the aorta and pulmonary artery to simulate the ventricular-vascular interactions in both systemic and pulmonary circulation which is described at the end of this chapter.

## CHAPTER 2

### **Organ - level validation of a left ventricular finite element model with detailed cross-bridge cycling descriptor**

#### **2.1 Introduction**

High-resolution left ventricular (LV) finite element (FE) models are useful in understanding ventricular mechanics associated with normal and abnormal heart functions<sup>59,61,83,121</sup>. These models are usually constructed using active contraction models that are developed based on experimental data at the cellular level. As such, it is unknown if these models are able to reproduce physiological behavior at the organ level. To the best of our knowledge, there have been no rigorous attempts to show that the models can simultaneously reproduce key organ-level physiology measured in the intact heart, specifically,

1. a linear load-independent end-systolic pressure volume relationship (ESPVR) and, a curvilinear end-diastolic pressure volume relationship (EDPVR) generated from PV loops of different loading conditions,
2. a linear, load-independent myocardial oxygen consumption ( $MVO_2$ ) and pressure-volume area (PVA) relationship.
3. a consistent strain-time profile.

Here, we have filled this void and showed that a LV FE model based on the active contraction descriptor of Rice *et al.*<sup>133</sup>, with appropriate adjustment of model parameters, was able to reproduce these measured physiological features when coupled to a closed-loop lumped parameter circulatory model. The content of this chapter has been published in the journal *physiological reports*<sup>144</sup>.

## 2.2 Method

### 2.2.1. Mechanical description of the left ventricle

The mechanical behavior of the left ventricle (LV) was modeled using a previously described cell-based coupled cardiac electromechanics model<sup>156</sup>. Given that the focus here is on the mechanics, homogeneous activation of the LV was employed via prescribed stimulus current  $I_s$  throughout the ventricle. Consequently, the resultant model can be expressed by the following system of ordinary differential equations and partial differential equations:

$$\frac{\partial \mathbf{s}}{\partial t} = f(v, \mathbf{s}, \lambda), \quad (2.1a)$$

$$\frac{\partial v}{\partial t} + I_{ion}(v, \mathbf{s}, \lambda) = I_s, \quad (2.1b)$$

$$\nabla \cdot \boldsymbol{\sigma} = 0. \quad (2.1c)$$

Equations (2.1a, b) consist of a system of ordinary differential equations describing the local coupling between the cellular electrophysiology<sup>173</sup> and cross-bridge cycling<sup>133</sup>. Here,  $v$  is the transmembrane potential,  $\mathbf{s}$  denotes a vector of state variables consisting of various membrane channels and intracellular ionic concentrations,  $I_{ion}$  is the total ionic current that is scaled with the membrane capacitance, and  $\lambda$  is the myofiber stretch. Equation (2.1c) enforces local mechanical equilibrium of the LV with  $\boldsymbol{\sigma}$  denoting the Cauchy stress tensor. The stress tensor  $\boldsymbol{\sigma}$  was additively decomposed into a passive component  $\boldsymbol{\sigma}_p$  and an active component  $\boldsymbol{\sigma}_a$ , allowing for dynamic changes in the tissue during the cross-bridge cycling process, i.e.,

$$\boldsymbol{\sigma} = \boldsymbol{\sigma}_p + \boldsymbol{\sigma}_a(\mathbf{s}, \lambda, \dot{\lambda}; T_{ref}). \quad (2.2)$$

The active stress  $\boldsymbol{\sigma}_a$ , applied along the local fiber orientation, was based on the active descriptor by Rice *et al.*<sup>133</sup>, and depends on the time evolution of the state variables  $\mathbf{s}$ , myofiber stretch  $\lambda$ , rate

of myofiber stretch  $\dot{\lambda}$  and the reference tension  $T_{ref}$ . Parameter values of the Rice descriptor were modified to obtain a twitch profile with a longer time to peak duration and a reasonable relaxation behavior (cf. to that computed using the original values) that are both necessary to reproduce the *in-vivo* strain-time profile measured in healthy humans. These parameters are associated to the Ca-binding with troponin (Ca-based activation) and transition rate between different states in the cross-bridge cycle. Some of these parameters were also adjusted in a previous study<sup>127</sup> to reproduce end-systolic pressure and pressure twitch recorded experimentally in the canine. The modified parameters are tabulated in **Table 2.1**. Contractility was varied by scaling the calcium transient through adjusting the maximum RyR channel Ca-flux  $v_1$ , scaling factor of Ca-ATPase  $K_{SR}$ , and maximum sarcolemmal Ca-pump current  $\bar{I}_{p(Ca)}$  in the electrophysiology model<sup>173</sup> as listed in **Table 2.2**. Modified parameters of the electrophysiology model (**Table 2.2**) reflect the corresponding changes in the isometric twitch profiles (**Figure 2.2**) for different contractility.

On the other hand, the passive stress  $\sigma_p$  was described using a Fung-type transversely-isotropic hyperelastic constitutive model<sup>57</sup> with the strain energy function given by

$$\Psi = \frac{1}{2}C(e^Q - 1) + C_{compr}(J \ln J - J + 1), \quad (2.3a)$$

where,

$$Q = b_{ff}E_{ff}^2 + b_{xx}(E_{ss}^2 + E_{nn}^2 + E_{sn}^2 + E_{ns}^2) + b_{fx}(E_{fn}^2 + E_{nf}^2 + E_{fs}^2 + E_{sf}^2). \quad (2.3b)$$

In the above equation,  $E_{ij}$  with  $(i, j) \in (f, s, n)$  are components of the Green-Lagrange strain tensor  $\mathbf{E}$  with  $f, s, n$  denoting the myocardial fiber, sheet and sheet normal directions, respectively. Furthermore,  $J = \det(\mathbf{F})$  is the Jacobian of the deformation gradient tensor  $\mathbf{F}$ . Material parameters

**Table 2.1.** Modified parameters of the Rice model<sup>133</sup>

Parameter	Unit	Value
perm50	Unitless	0.38
$n_{perm}$	Unitless	13
$k_{on}$	$\mu\text{M}^{-1}\text{s}^{-1}$	60
$k_{n_p}$	$\text{s}^{-1}$	15
$k_{p_n}$	$\text{s}^{-1}$	550
$g_{app}$	$\text{s}^{-1}$	10
$h_f$	$\text{s}^{-1}$	750
$h_b$	$\text{s}^{-1}$	70
$g_{xb}$	$\text{s}^{-1}$	20

**Table 2.2.** Modified parameters of the cellular electrophysiology model<sup>173</sup> which result change in the contractility

Parameter	Unit	Baseline contractility	Lower contractility	Higher contractility
$V_1$	$\text{ms}^{-1}$	1.8	1.2	4.2
$K_{SR}$	unitless	1.3	0.7	1.4
$I_{p(\text{Ca})\text{max}}$	$\mu\text{A}\mu\text{F}^{-1}$	0.05	0.3	0.008

of the passive constitutive model are denoted by  $C_{\text{compr}}$ ,  $C$ ,  $b_{ff}$ ,  $b_{xx}$  and  $b_{fx}$ . The passive stress tensor depends on this strain energy function by

$$\boldsymbol{\sigma}_p = \frac{1}{J} \mathbf{F} \frac{\partial \psi}{\partial \mathbf{E}} \mathbf{F}^T. \quad (2.4)$$

The governing equations describing the LV mechanical behavior were solved using the FE method.

An idealized prolate ellipsoid was used to describe the LV geometry, which was discretized using 960 quadratic tetrahedral elements. The LV base was constrained from moving out of the plane and the epicardial edge was fixed<sup>46,171</sup>. Based on previous experimental measurements<sup>153</sup>, myofiber helix angle was prescribed to vary with a linear transmural variation from  $60^\circ$  at the endocardium to  $-60^\circ$  at the epicardium in the LV wall.

### 2.2.2 Closed-loop circulatory model

The LV FE model was coupled to a closed-loop lumped parameter circulatory model (**Fig. 2.1A**).

The total mass of blood for the closed-loop system needs to be conserved, so, the rate of change of volume for the cardiac chambers (LV and LA) and blood vessels (Aorta and vena cava) can be related to the flowrates by the following equations,

$$\frac{dV_{LA}}{dt} = q_{ven} - q_{mv} \quad (2.5a)$$

$$\frac{dV_{LV}}{dt} = q_{mv} - q_{ao} \quad (2.5b)$$

$$\frac{dV_{art}}{dt} = q_{ao} - q_{per} \quad (2.5c)$$

$$\frac{dV_{ven}}{dt} = q_{per} - q_{ven} \quad (2.5d)$$

Flowrates at different sections are given by,

$$q_{ao} = \begin{cases} \frac{P_{LV} - P_{art}}{R_{ao}} & \text{when, } P_{LV} \geq P_{art} \\ 0 & \text{when, } P_{LV} < P_{art} \end{cases} \quad (2.6a)$$

$$q_{per} = \frac{P_{art} - P_{ven}}{R_{per}} \quad (2.6b)$$

$$q_{ven} = \frac{P_{ven} - P_{LA}}{R_{ven}} \quad (2.6c)$$

$$q_{mv} = \begin{cases} \frac{P_{LA} - P_{LV}}{R_{mv}} & \text{when, } P_{LA} \geq P_{LV} \\ 0 & \text{when, } P_{LA} < P_{LV} \end{cases} \quad (2.6d)$$

For blood vessels, pressure is found from the following equations,

$$P_{art} = \frac{V_{art} - V_{art,0}}{C_{art}} \quad (2.7)$$

$$P_{ven} = \frac{V_{ven} - V_{ven,0}}{C_{ven}} \quad (2.8)$$

where,  $V_{art,0}$  and  $V_{ven,0}$  are resting volumes of the blood vessels and both are constants.

In this model, time-varying elastance model was used to describe atrial contraction by relating the instantaneous atrial pressure  $P_{LA}(t)$  to the instantaneous atrial volume  $V_{LA}(t)$  using the following equations,

$$P_{LA}(t) = e(t)P_{es,LA}(V_{LA}) + (1 - e(t))P_{ed,LA}(V_{LA}) \quad (2.9)$$

where,

$$P_{es,LA}(V_{LA}) = E_{es,LA}(V_{LA} - V_{0,LA}) \quad (2.10a)$$

$$P_{ed,LA}(V_{LA}) = A_{LA} (e^{B_{LA}(V_{LA} - V_{0,LA})} - 1) \quad (2.10b)$$

and,

$$e(t) = \begin{cases} \frac{1}{2} \left( \sin \left[ \left( \frac{\pi}{T_{max}} \right) t - \frac{\pi}{2} \right] + 1 \right); & 0 < t \leq 3/2 T_{max} \\ \frac{1}{2} e^{-(t - 3/2 T_{max})/\tau}; & t > 3/2 T_{max} \end{cases} \quad (2.10c)$$

In the above,  $E_{es,LA}$  is the end-systolic elastance,  $V_{0,LA}$  is the volume axis intercept of the ESPVR, and both  $A_{LA}$  and  $B_{LA}$  are parameters of the EDPVR. The driving function  $e(t)$  is described in Eq. (2.10c), where  $T_{max}$  is the point of maximal chamber elastance,  $\tau$  is the time constant of relaxation and  $t$  is the time during the cardiac cycle. The values of  $E_{es,LA}$ ,  $V_{0,LA}$ ,  $A_{LA}$ ,  $B_{LA}$ ,  $T_{max}$  and  $\tau$  that are used in this model are listed in **Table 2.4**.

The initial volume states ( $V_{ven}$ ,  $V_{art}$ ) and the circulatory parameters were adjusted so that the steady-state PV loop is consistent with that found in a typical normal human LV operating under resting conditions. Preload of the LV was varied by changing the venous volume  $V_{ven,0}$  to

**Table 2.3.** Normal parameter values of the circulatory model

Parameter	Unit	Values
Aortic valve resistance, $R_{ao}$	Pa ms ml <sup>-1</sup>	5500
Peripheral resistance, $R_{per}$	Pa ms ml <sup>-1</sup>	140000
Venous resistance, $R_{ven}$	Pa ms ml <sup>-1</sup>	2000
Mitral valve resistance, $R_{mv}$	Pa ms ml <sup>-1</sup>	2500
Aortic compliance, $C_{art}$	ml Pa	0.014
Venous compliance, $C_{ven}$	ml Pa	0.3
Resting volume for artery, $V_{art,0}$	ml	580
Resting volume for vein, $V_{ven,0}$	ml	3300

**Table 2.4.** Parameters of time varying elastance model for left atrium

Parameter	Unit	Values
End-systolic elastance, $E_{es,LA}$	Pa/ml	60
Volume axis intercept, $V_{0,LA}$	ml	10
Scaling factor for EDPVR, $A_{LA}$	Pa	58.67
Exponent for EDPVR, $B_{LA}$	ml <sup>-1</sup>	0.049
Time to end-systole, $T_{max}$	msec	200
Time constant of relaxation, $\tau$	msec	25

simulate vena cava occlusion. On the other hand, afterload was varied by altering the peripheral resistance  $R_{per}$  to simulate the constriction of vessels in the systemic vasculature. A steady-state pressure-volume loop for each loading condition was established by running the simulation over several cardiac cycles, each with a cycle time of 900ms (equivalent to 67 bpm).

### 2.2.3 End-systolic and end-diastolic pressure-volume relationships

After obtaining PV loops at different preload and afterload, end-systolic and end-diastolic pressure-volume relationships (ESPVR and EDPVR, respectively) were obtained by performing regression on the following relationships:

$$P_{ESPVR}(V) = E_{es}(V - V_0), \quad (2.11a)$$

$$P_{EDPVR}(V) = A(e^{B(V-V_0)} - 1), \quad (2.11b)$$

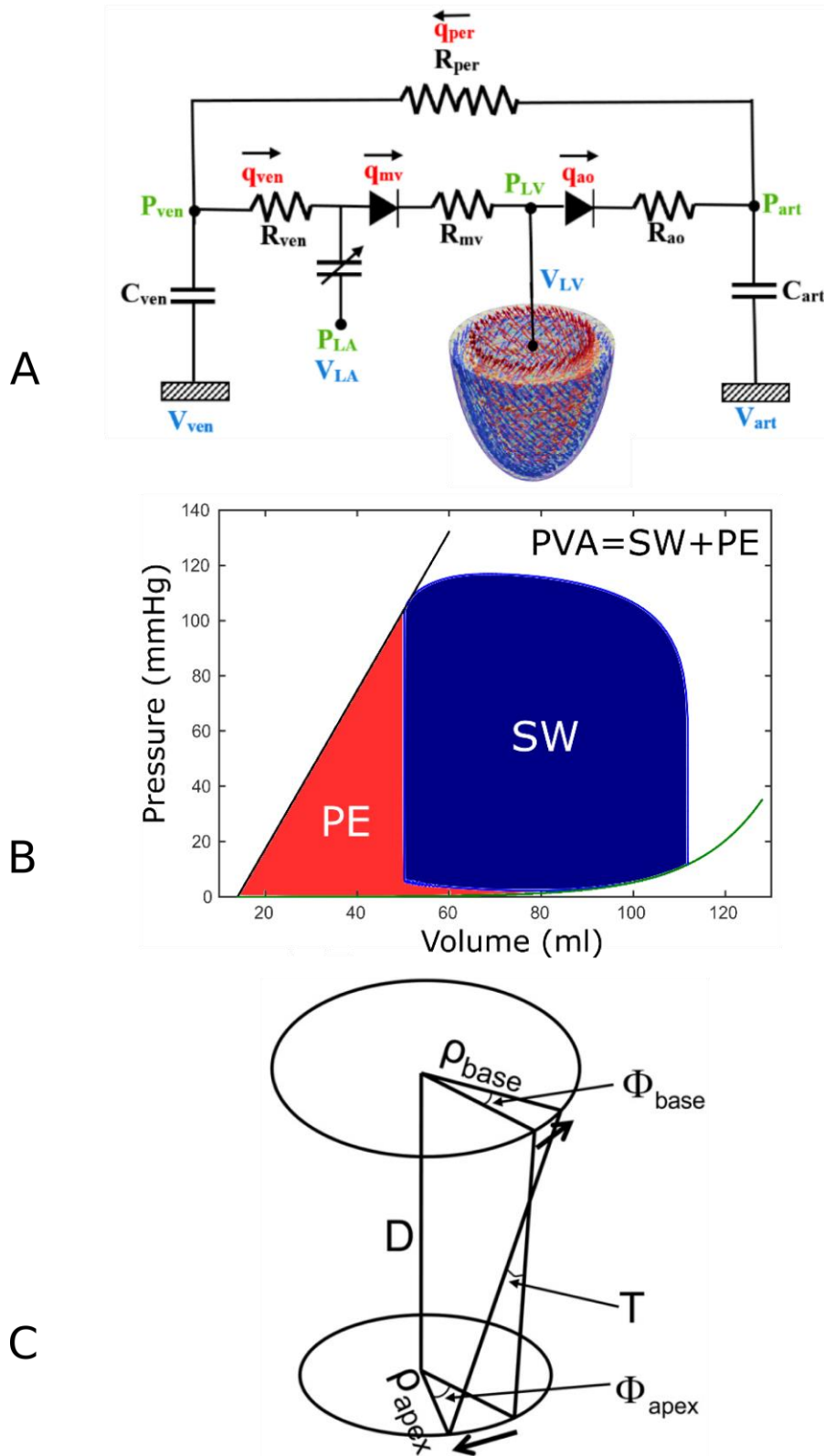


**Figure 2.1.** (A) Model schematic showing the coupling of LV FE model to a closed-loop lumped parameter circulatory model, (B) Schematic showing the calculation of pressure-volume area (PVA), (C) Schematic showing the definition of LV torsion.

where,  $E_{es}$  is the ESPVR slope,  $V_0$  is the volume-intercept, and  $A, B$  are parameters for the curvilinear EDPVR.

#### 2.2.4 Calculation of myocardial oxygen consumption

The local adenosine triphosphate (ATP) consumption during cross-bridge cycling have been estimated by a previously<sup>68</sup> described method. The local ATP consumption rate was calculated from the Rice *et al.* model<sup>133</sup> by multiplying the cross-bridge detachment rate by the single-overlap fraction of the thick filament and the probability that the cross-bridge is in the post-rotated force-generating state. In mathematical terms,

$$ATP = g_{xbT} X B_{PostR} SOVF_{thick}(x) \quad (2.12)$$

where,  $g_{xbT}$  is the cross-bridge detachment rate,  $X B_{PostR}$  is the probability that the cross-bridge is in the post-rotated force-generating state,  $SOVF_{thick}(x)$  is the single-overlap function for the thick filament,  $x$  is the sarcomere length as described in detail in Rice *et al.* model<sup>133</sup>.

Myocardial oxygen consumption was quantified using the total ATP consumption, which was computed by integrating the local ATP consumption rate over the entire LV through a complete cardiac cycle. The  $MVO_2$  at each loading case was related to the corresponding PVA, which is defined by the sum of the stroke work (i.e., external work done by the LV) and the end-systolic potential energy (i.e., mechanical energy stored within elastic elements of the contractile proteins at the end of systole) (**Figure 2.1B**).

#### 2.2.5. Calculation of myocardial strain

Regional three-dimensional strains in the longitudinal, circumferential and radial directions were calculated using end-diastole as the reference configuration. Specifically, myofiber stretch in these directions were expressed as:

$$\lambda_i = \sqrt{\mathbf{e}_i \cdot \mathbf{C} \cdot \mathbf{e}_i}, \quad (2.13)$$

where,  $\mathbf{C} = \mathbf{F}^T \mathbf{F}$  is the right Cauchy-Green deformation tensor, and  $\mathbf{e}_i$  with  $i \in (l, c, r)$  are the unit vectors in the longitudinal  $l$ , circumferential  $c$  and radial  $r$  directions, respectively. The radial direction  $\mathbf{e}_r$  is defined to be normal to the LV wall. The circumferential direction  $\mathbf{e}_c$  is defined to be orthogonal to  $\mathbf{e}_r$  and the apex-base direction. Finally, the longitudinal direction,  $\mathbf{e}_l$  is defined to be orthogonal to the both  $\mathbf{e}_r$  and  $\mathbf{e}_c$ . This longitudinal direction is therefore tangential to the LV cavity wall surface. Different strain metrics, namely, the Biot, Green-Lagrange strain and Euler-Almansi strains were calculated using the following respective definitions:

$$\varepsilon_i = \lambda_i - 1, \quad (2.14a)$$

$$E_i = \frac{1}{2}(\lambda_i^2 - 1), \quad (2.14b)$$

$$e_i = \frac{1}{2}\left(1 - \frac{1}{\lambda_i^2}\right). \quad (2.14c)$$

### 2.2.6 Calculation of left ventricular torsion

Left ventricular torsion  $T$ , which describes the amount of twisting the LV undergoes as it contracts, was calculated based on the relative rotation between the basal and the apical short axis slices (**Figure 2.1C**) using the following equation<sup>4</sup>:

$$T = \frac{(\phi_{apex} - \phi_{base})(\rho_{apex} + \rho_{base})}{2D}. \quad (2.15)$$

In Eq. (2.15),  $\rho_{apex}$  and  $\rho_{base}$  are the mean radius of curvature of the basal and apical slices respectively and,  $D$  is the distance between apical and basal slices. The angle of rotation at the apex  $\phi_{apex}$  and base  $\phi_{base}$  were calculated by tracking the motion of the nodal points at the apex and

base respectively. Because the rotation varies across the LV wall, an average value of  $T$  was calculated using points on both the epicardial and endocardial surface.

## 2.3 Results

### 2.3.1 Isometric twitch behavior

Isometric twitch profile computed using the adjusted rate constants (**Table 2.1**) shows that the time to peak value is  $\sim 170$ ms (cf. to  $\sim 100$ ms found in the original model using parameters calibrated using rat data) (**Figure 2.2**). This value is consistent with the isometric twitch profile found in normal human<sup>98</sup>. On the other hand, scaling of the calcium transient in the electrophysiology model (**Table 2.2**) produces isometric twitch profiles that are self-similar to each other.

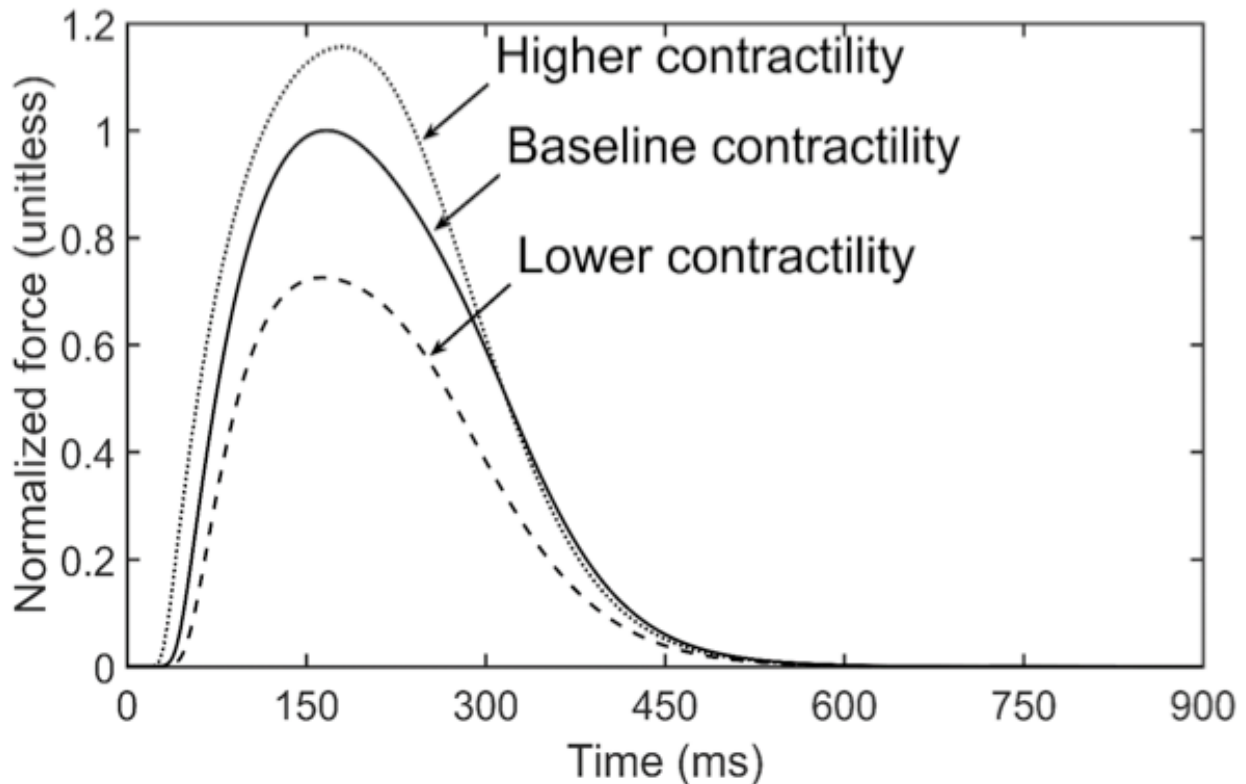


**Figure 2.2.** Isometric twitch profiles for different contractility cases. Force values were normalized by the maximum force of the baseline contractility case.

### 2.3.2 Pressure-volume loops

Steady-state PV loops of the LV under different loading conditions and contractilities were obtained from the FE model (**Figure 2.3**). Increasing preload while maintaining a constant afterload resistance led to an increase in peak systolic pressure and shifted both the end-systolic volume (ESV) and end-diastolic volume (EDV) rightward towards larger volumes (**Figure 2.3A**). Ejection fraction (EF), however, remained relatively constant between 58 and 59%. On the other hand, increasing afterload with a constant preload volume led to an increase in peak systolic pressure and ESV, with decreasing EF (**Figure 2.3B**). In both cases (varying preload and afterload), the series of end-systolic and end-diastolic points derived from the PV loops produced a linear ESPVR and a curvilinear EDPVR. Also, an increase (or decrease) in contractility led to a corresponding increase (or decrease) in peak systolic pressure, EF, and the slope of the ESPVR (**Figure 2.3C**).

Parameter values of  $E_{es}$ ,  $V_0$ ,  $A$  and  $B$  were calculated via regression analysis using Eq. (2.5) applied to these data points (**Table 2.5**). The volume-intercept  $V_0$  remained relatively constant in all the cases. On the other hand, the ESPVR slope  $E_{es}$  changed substantially (from the baseline case) only with varying contractility and changed only a little in the case when afterload was varied.

**Table 2.5.** Parameters associated with ESPVR and EDPVR as found by the regression analysis.

Parameter	Varying preload at			Varying afterload at baseline contractility
	baseline contractility	lower contractility	higher contractility	
Slope of ESPVR, $E_{es}$ (mmHg/ml)	3.67	2.51	5.54	3.81
Volume axis intercept, $V_0$ (ml)	18.0	17.7	19.5	19.5
Scaling factor for EDPVR, $A$ (mmHg)	0.021	0.021	0.021	0.021
Exponent for EDPVR, $B$ (ml <sup>-1</sup> )	0.065	0.065	0.065	0.065

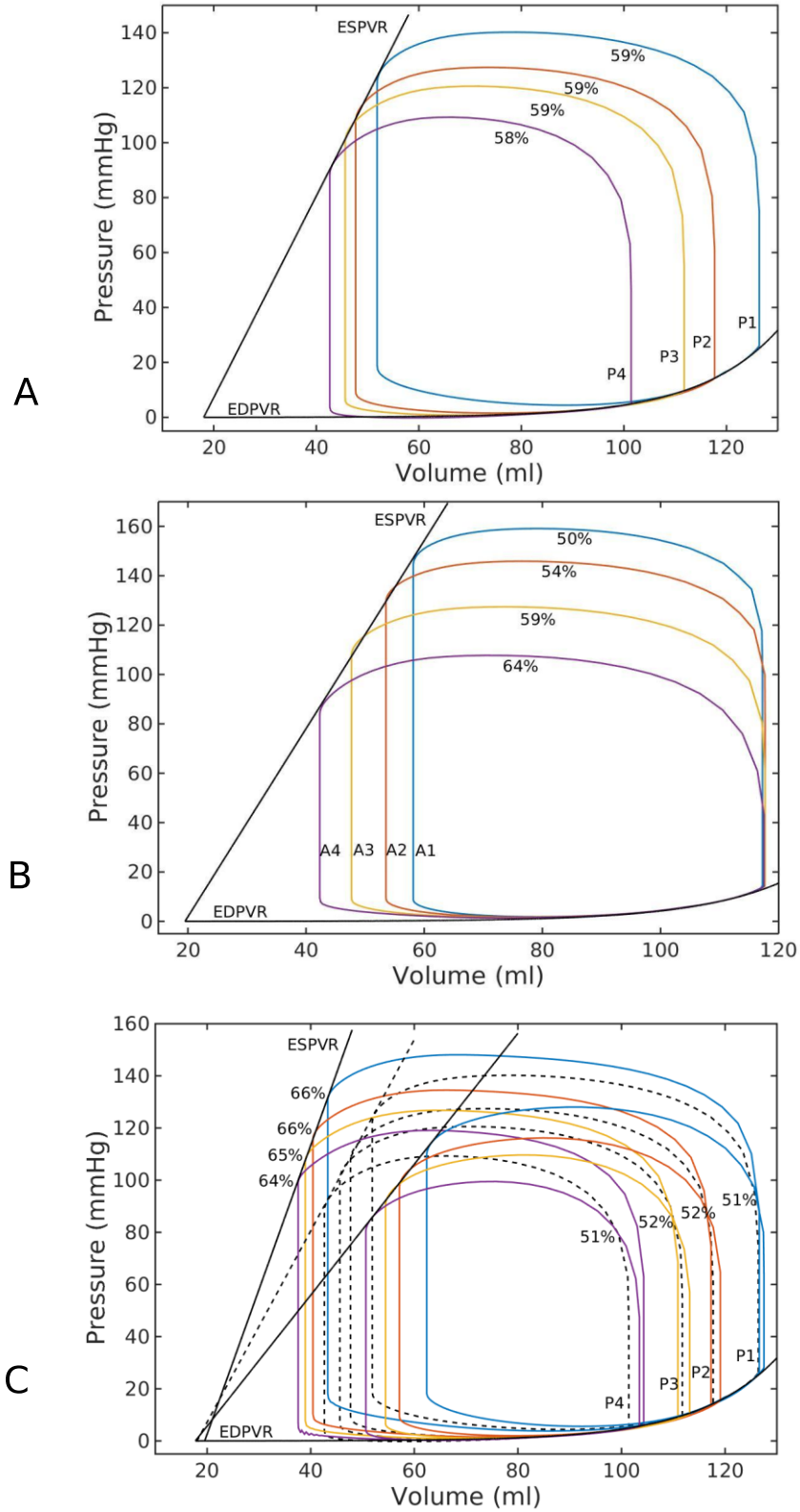


**Figure 2.3.** Effects on pressure-volume loop by due to a change in (A) preload at a constant afterload, (B) afterload at a constant preload, (C) contractility (solid) c.f. baseline (dotted), Values indicate corresponding ejection fraction.

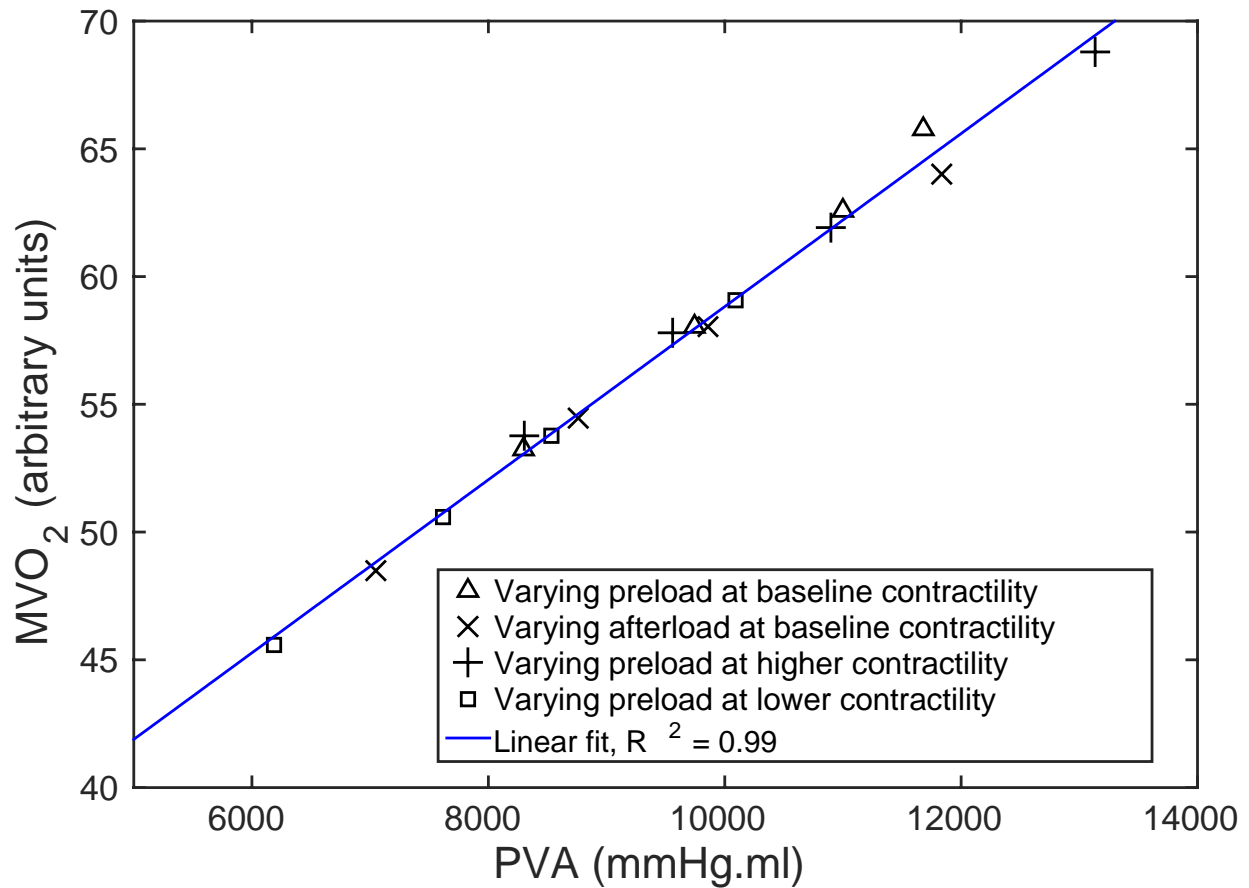


**Figure 2.4.** Myocardial oxygen consumption (MVO<sub>2</sub>) vs. pressure-volume area (PVA) relationship predicted by the model. Data points are calculated at different preload, afterload and contractilities.

### 2.3.3 MVO<sub>2</sub>-PVA Relationships

The relationship between PVA and the total LV ATP consumption in a cardiac cycle that is directly related to MVO<sub>2</sub> were computed for different loading conditions and contractilities. The MVO<sub>2</sub> – PVA data calculated in all the cases having different preload, afterload and contractilities clustered around a straight line (**Figure 2.4**). Regression performed on the data showed that the MVO<sub>2</sub> – PVA relationship is linear ( $R^2 = 0.99$ ).

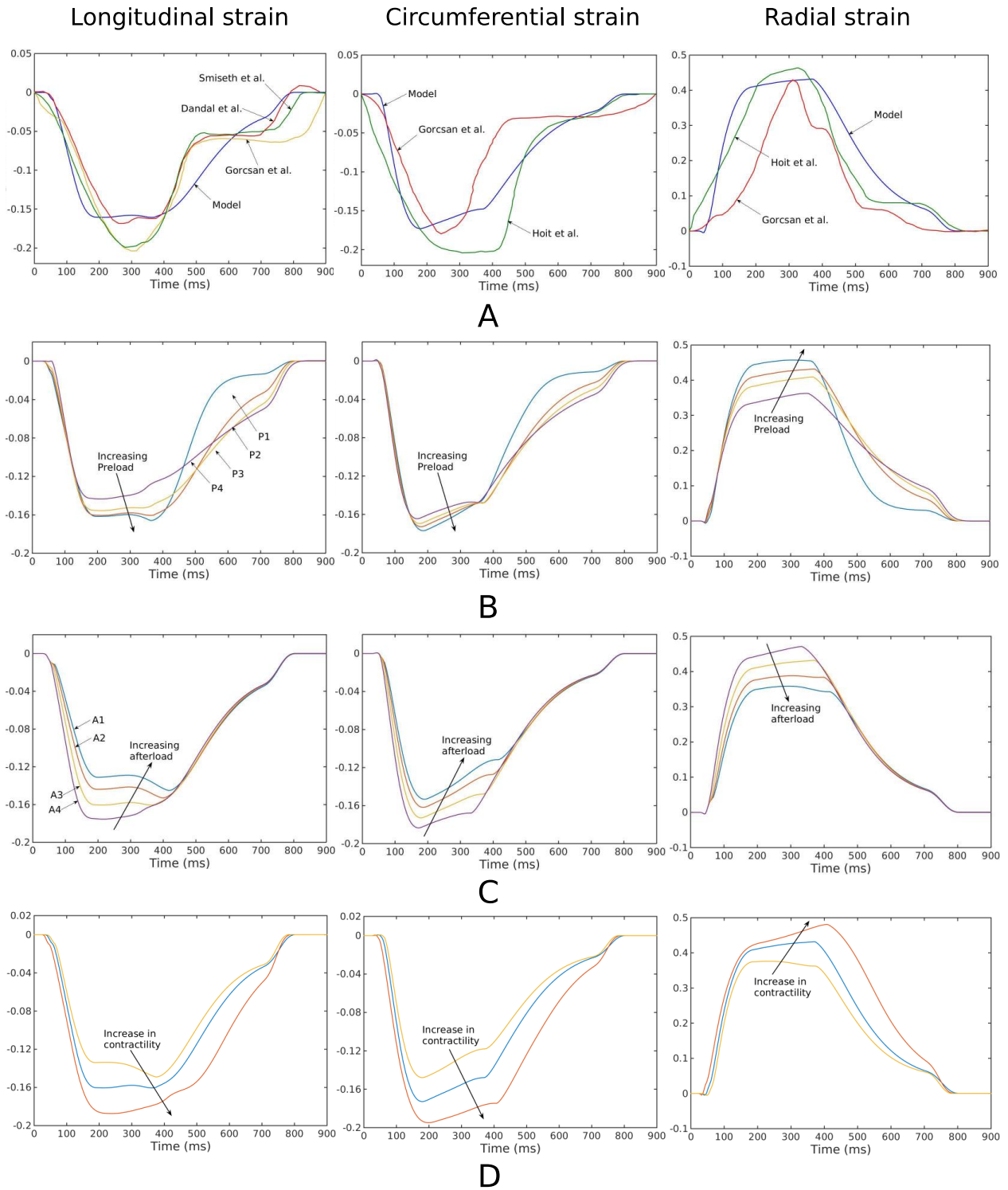


**Figure 2.5.** Longitudinal (first column), circumferential (second column), radial (third column) strain-time profiles. (A) Comparison of the model predictions with previously published *in vivo* 2D STE measurements<sup>37,52,65</sup>. Strain-time profiles predicted by the model with, (B) different preload (with constant afterload), (C) different afterload (with constant preload) and, (D) different contractility for a representative case (case P2 shown in Figure 2.3A and 2.3C).

### 2.3.4 Myocardial strain

Longitudinal, circumferential and radial strain-time profiles computed for different loading conditions and contractilities were compared to those measured in normal humans using speckle tracking echocardiography (STE)<sup>37,52,65</sup> (**Figure 2.5**). Under all loading conditions, the predicted strain-time profiles were consistent with measurements in humans. Specifically, comparable features include a time-to-peak strain of about 200 ms during systole and a rapid change in strain at late diastole (~ 700 ms) arising from the contraction of left-atrium (i.e. ‘atrial kick’). Peak strain values predicted by the model (~ -16%, -18% and 40% in longitudinal, circumferential and radial directions) were also comparable to those measured in normal humans.

Generally, peak circumferential and longitudinal strains were less sensitive to the loading conditions than radial strain. Varying preload filling pressure (by ~ 20 mm Hg) at baseline contractility led to little change in the peak longitudinal strain (~2% absolute) or circumferential strain (~1% absolute). Peak radial strain, however, was substantially increased (~10% absolute) with increasing preload. On the other hand, peak strains were slightly more sensitive to variations in afterload than preload, where a 50 mmHg increase in afterload pressure was associated with reduced peak longitudinal, circumferential and radial strain of 4%, 3% and 12% (absolute), respectively. An increase in contractility (with respect to baseline) led to an increase in the peak values of longitudinal (2.7% absolute), circumferential (2.2% absolute) and radial (5% absolute) strain with similar strain-time characteristics. Similarly, the peak values of longitudinal (1.5% absolute), circumferential (2.5% absolute) and radial (6% absolute) strain decreased with a decrease in contractility with no change in strain-time characteristics.

Regional variation of strain profiles under different loading conditions followed a consistent pattern, shown in a representative case in **Figure 2.6**. Longitudinal strain was highest

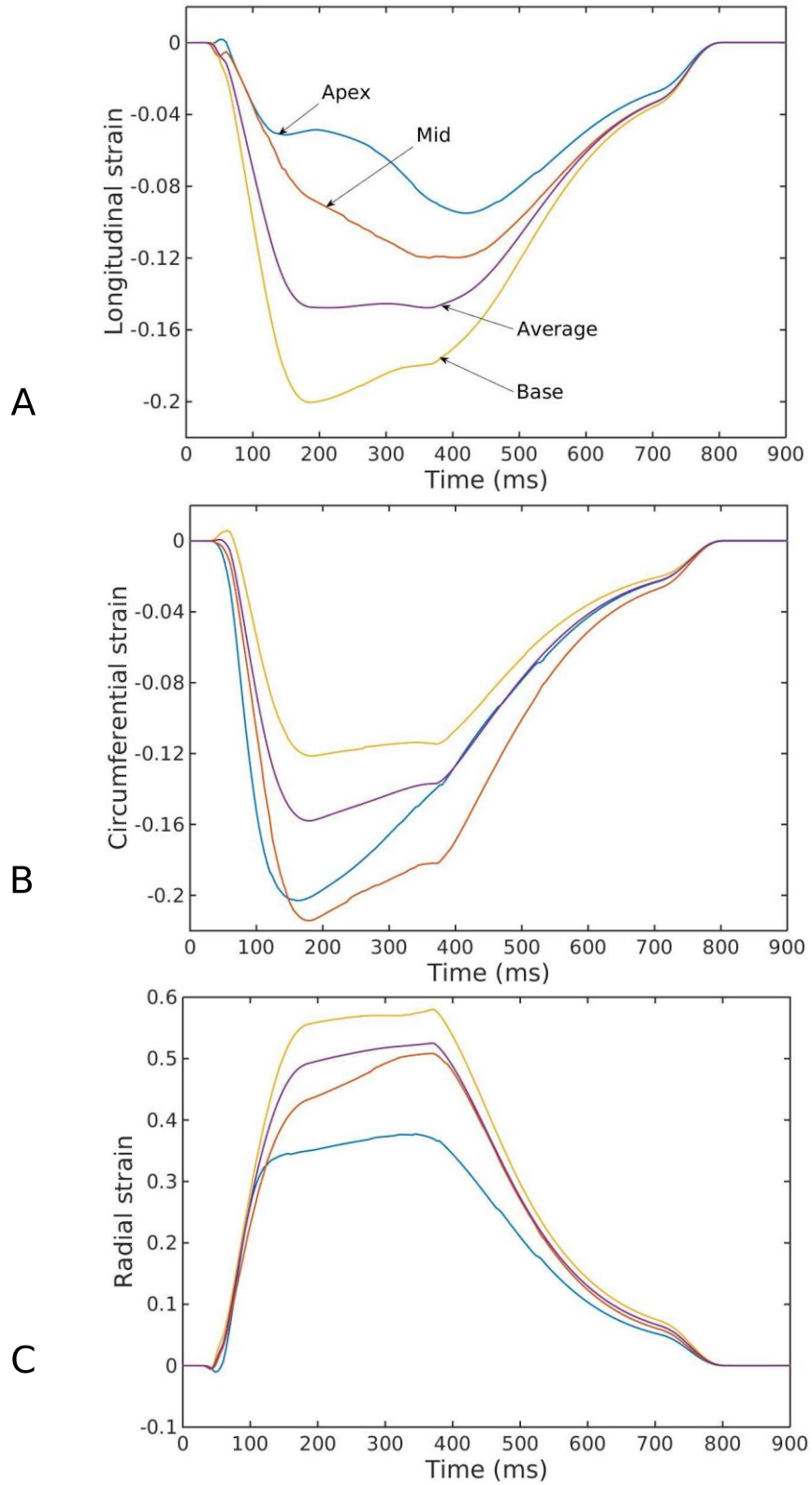


**Figure 2.6.** Regional variation of (A) longitudinal, (B) circumferential and (C) radial strain profiles for a specific case corresponding with normal hemodynamic conditions (case P2, Figure 2.3A).

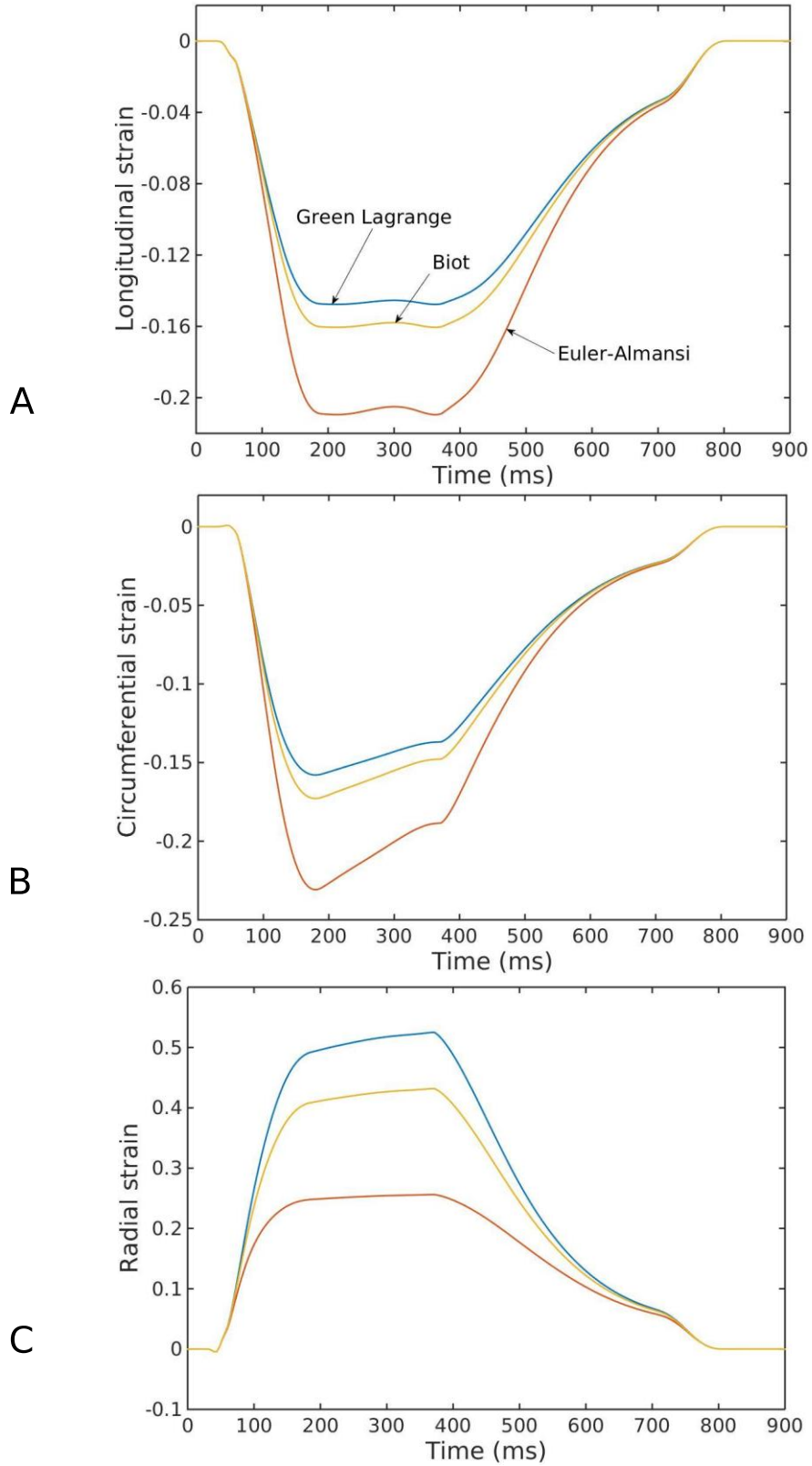


**Figure 2.7.** (A) Longitudinal, (B) circumferential, (C) radial strain profiles calculated using different strain definitions.

at the basal region and lowest at the apical region with a difference of about 10% (absolute). The same pattern was also found in the radial strain, where the difference between the highest strain (at the basal region) and the lowest strain (at the apical region) was about 20%. Regional variation of the circumferential strain was comparatively similar to the longitudinal strain, about 10%, with the highest value found at the mid LV and the lowest value found at the basal region.

Using different strain definitions can lead to a substantial variation in the reported strain values (**Figure 2.7**). Longitudinal and circumferential strains computed using the Euler-Almansi definition were the largest followed by those computed using the Biot and Green-Lagrange definitions. The reverse was found in the radial strain component, in which strains calculated using the Green-Lagrange definition were the largest. The difference between these various strain definitions can be as large as ~27%, ~6% and ~7% in the radial, longitudinal and circumferential directions, respectively.

### **2.3.5 LV torsion**

The time-variation of LV torsion over a cardiac cycle was compared to the measurements made in normal human using echocardiography (**Figure 2.8**)<sup>116</sup>. Our model prediction of the peak LV torsion was close to that found in normal humans (~15 degrees). Finally, LV torsion was also found to be relatively independent of the loading conditions. Similar to the effects of contractility on strains, a change in contractility (increase or decrease) led to a corresponding change in the peak value of LV torsion.

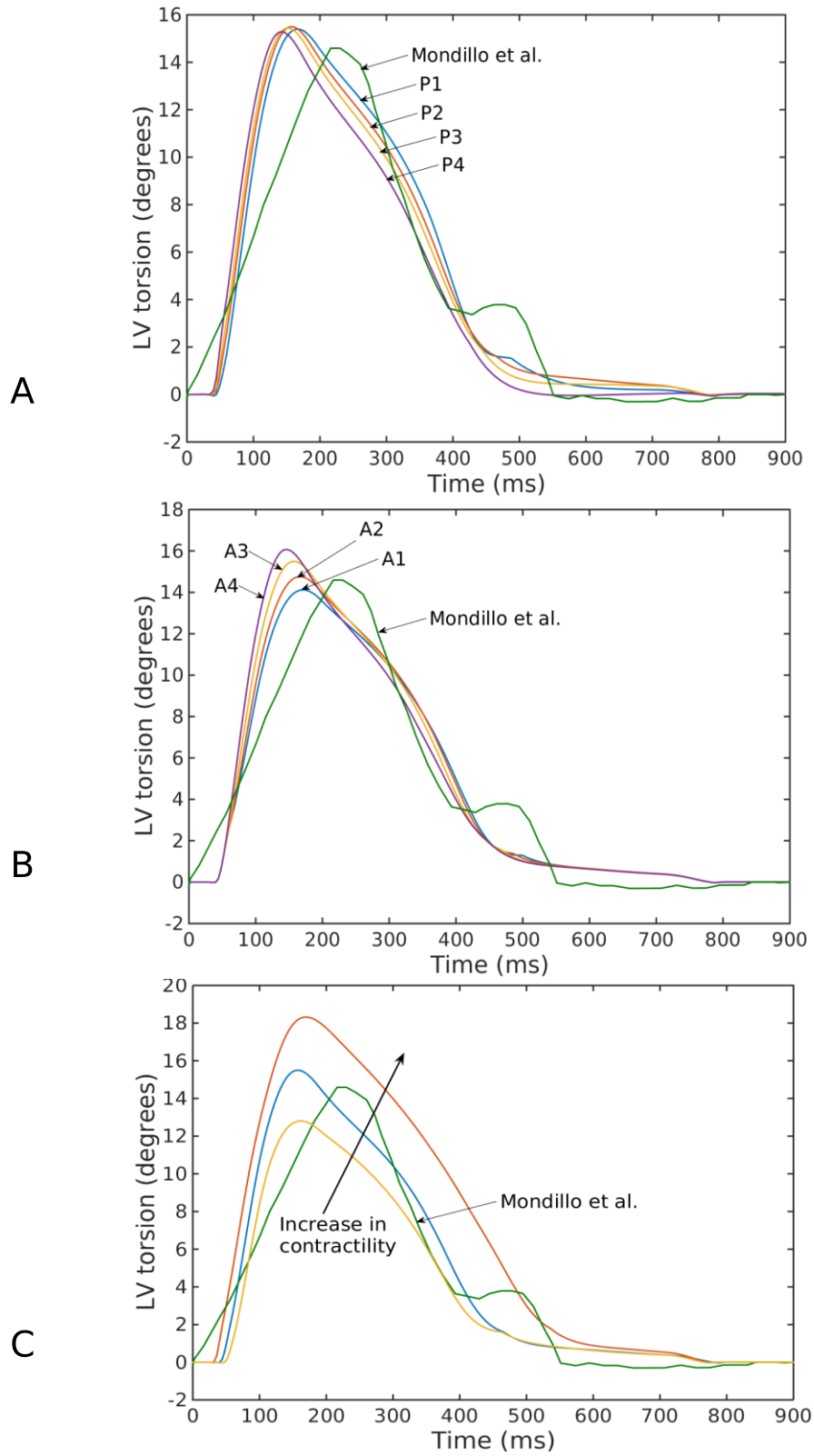


**Figure 2.8.** Left ventricular torsion for varying (A) preload, (B) afterload and (C) contractility (case P2 in Figure 2.3A and 2.3C) compared with echocardiographic measurements by Mondillo *et al.*<sup>116</sup>.

## 2.4 Discussion

Finite element models simulating the LV mechanical behavior during a cardiac cycle have been developed using a variety of active contraction models<sup>59,61,83,121</sup>. To the best of our knowledge, however, there have been no rigorous attempts to show that the models are able to simultaneously reproduce key organ-level physiology measured in the intact heart, specifically, (1) linear, load-independent ESPVRs generated from PV loops of different loading conditions, (2) a linear, load-independent  $MVO_2 - PVA$  relationship and (3) a consistent strain-time profile. Here, we have filled this void and showed that a LV FE model based on the active contraction descriptor of Rice *et al.*<sup>133</sup>, with appropriate adjustment of model parameters, was able to reproduce these measured physiological features when coupled to a closed-loop lumped parameter circulatory model.

Specifically, we demonstrated that both the slope and volume-intercept of the linear ESPVR generated by varying preload and afterload are close to one another. The fitted values of  $E_{es}$  and  $V_0$  are also comparable to those measured in humans<sup>113</sup>. Statistical analysis performed on the regressed values of  $E_{es}$  (**Table 2.3**) shows that the difference in values obtained for the varying preload and afterload cases (at the same baseline contractility) is not significant (p value = 0.57, 95% confidence interval). When contractility is varied (increased or decreased), however, the change in  $E_{es}$  (with respect to the baseline contractility cases) becomes significant (p value = 0.003, 95% confidence interval). As opposed to using pure phenomenological descriptors of active contraction<sup>83</sup>,  $MVO_2$  of the LV can be estimated here using the 4-state active contraction descriptor by calculating the total ATP consumption required to uncouple the actin-myosin bonds over a cardiac cycle, a reasonable estimate as approximately 90% of ATP generation is derived from aerobic metabolism. As  $MVO_2$  was estimated here solely from the cellular-scale quantities in the 4-state active contraction descriptor, correlating this calculated  $MVO_2$  to PVA, an organ-scale

quantity, serves as a rigorous and independent validation for the multiscale model. Consistent with the physiological measurements across species<sup>29,155,170</sup>, our model predicts a linear relationship between MVO<sub>2</sub> and PVA with varying preload, afterload and contractility.

In terms of deformation, our model predicted LV torsion as well as circumferential, longitudinal and radial strain-time profiles that are agreeable with measurements from studies using echocardiography<sup>37,52,65,116,122</sup>. Although these measurements showed significant variability, our model was able to reproduce key features, such as similar peak strains, time-to-peak-strain as well as the rapid change in strain during atrial contraction at late-diastole.

Using our model, we also compared the strains calculated using different definitions, namely, the Green-Lagrange, Biot and Euler-Almansi strain definitions. We showed that the difference could be as large as 27% in the radial direction and 6% in the longitudinal and circumferential directions when comparing between strains calculated using the Green-Lagrange and Euler-Almansi definitions. Circumferential and longitudinal strains computed using the Euler-Almansi definition are larger than those calculated using the Green-Lagrange definition whereas the opposite is true for radial strain (**Figure 2.7**). This is consistent with the fact that the normalizing reference length used in the Green-Lagrange definition is based on the ED configuration, at which length segments are at their longest in the circumferential and longitudinal directions and shortest in the radial direction. While most magnetic resonance (MR) based studies are explicit about the strain definition with Green-Lagrange strain being the most commonly used metric<sup>106,117</sup>, echo-based studies are less clear concerning the type of metric used in computing myocardial strains. A number of echo-based studies have described Lagrangian and Eulerian strain<sup>37,147</sup>. The definition of Lagrangian strain ( $\varepsilon = \Delta L/L = \lambda - 1$ ) in those studies, however, is more commonly referred to as the Biot strain by the continuum mechanics community and differs

from the Green-Lagrange strain that is frequently used in MR studies. The substantial disparity in strain computed using these two metrics (especially in computing radial strain) underscore the importance of using a consistent strain metric when comparing strain between different imaging modalities or between simulations and experiments.

We have also investigated the effects of preload and afterload on myocardial strains and have showed that the strains are sensitive to changes in loading conditions at a fixed LV contractility. The radial strain is found to be the most sensitive, and all three strains are found to be sensitive to changes in afterload resistance that translated to relatively large changes in the peak LV pressures and EF. This result underscores the importance of not equating an evaluation of strains to an evaluation of myocardial contractility<sup>132</sup>, especially when myocardial strains are increasingly used in diagnosing heart diseases such as myocardial ischemia, heart failure with preserved ejection fraction (HFpEF) and mechanical dyssynchrony<sup>37,147</sup>.

Particularly for HFpEF, a recent clinical study<sup>93</sup> has shown that the global longitudinal and circumferential strains are impaired in this patient population, and are about 5% points lower than those measured in normal humans (longitudinal: 20% vs. 14.6% absolute; circumferential: 27.1% vs. 22.9%, absolute). Stratifying HFpEF patients into categories with different ranges of LV EF, that study also showed a positive correlation between LV EF and both longitudinal and circumferential strains. A similar positive correlation between LV EF and the strains can also be found from our simulation results with varying afterload. In our simulation, the ESP ranges between 105 – 140 mmHg, which is equivalent to a systolic blood pressure range of 117 – 156 mmHg based on the empirical formula  $ESP = 0.9 \times SBP$ <sup>77</sup>. Systolic blood pressure measured in the clinical study was only slightly higher in HFpEF patients (90% are hypertensive) than the normal subjects (136 vs. 130 mm Hg). Our study therefore suggests that an increase in afterload

may contribute, at least partially, to the decrease in longitudinal and circumferential strains found in HFpEF compared to normals. More study is clearly needed to separate the effects of a higher afterload from that of a decrease in contractility in contributing to the reduced longitudinal and circumferential strains in HFpEF patients.

#### **2.4.1 Limitations**

There are some limitations associated with the model. First, an idealized prolate ellipsoid was used to describe the LV geometry, which ignores any asymmetrical geometrical differences. Second, the model assumes that the LV contracts homogeneously and neglects any regional activation patterns. Third, a rule-based myofiber orientation was prescribed in this model, in which the myofiber helix angle varied linearly in the transmural direction from endocardium to epicardium. The myofiber orientation, in reality, may be more complex. Last, mechanical effects associated with the right ventricle (RV) and pulmonary circulation was neglected. Although cavity pressure in the RV is substantially lower than the LV, its presence may, nevertheless, affect the LV mechanics through the septum.

## CHAPTER 3

### Computational investigation of the pathophysiological mechanisms in heart failure with preserved ejection fraction (HFpEF)

#### 3.1 Introduction

Heart failure with preserved ejection fraction (HFpEF) is a syndrome that accounts for about one-half of all chronic heart failure with increasing incidence and prevalence rates<sup>18,123</sup>. Diastolic dysfunction is a common feature (e.g., slow LV relaxation,<sup>178</sup> cardiomyocyte stiffening,<sup>178</sup> concentric hypertrophy<sup>166</sup>) found in HFpEF patients which was initially believed to be the sole mechanism underlying HFpEF. Recent evidence has suggested, however, that systolic function may be also impaired in this disease<sup>93,118,142,180</sup>. Specifically, clinical studies have found that the longitudinal and circumferential strains in left ventricle (LV) of HFpEF patients are reduced, suggesting that myocardial contractility may also be impaired. On the other hand, studies have shown that end-systolic elastance ( $E_{es}$ ) and LV ejection fraction (EF) are normal or increased in HFpEF (suggesting preserved or increased global *ventricular* contractility)<sup>22,76</sup>. These seemingly conflicting observations (normal or increased chamber contractility but decreased myocardial motion) are difficult to resolve purely through basic or clinical experimental studies because multiple confounding factors such as influences of increased vascular resistance (afterload), altered LV geometry, increased LV mass are involved. Therefore, it is very difficult to isolate factors affecting LV function and motion in HFpEF patients so as to clarify their individual role(s) and contribution(s).

Accordingly, the purpose of this study was to determine whether decreased longitudinal strain encountered in HFpEF is truly a reflection of decreased myocardial contractility or is this simply due to altered LV mass, geometry or afterload resistance. To do so, we employed a previously validated computational modeling framework<sup>144</sup> (discussed in detail in chapter 2)

whose parameters were adjusted to replicate key characteristics of heart and vascular properties in HFpEF to independently assess the roles of these contributing factors. Resolution of this question is important because of its implication for the development of new therapies.

## **3.2 Methods**

### **3.2.1 Computational modeling framework**

A previously described coupled left ventricle (LV) – closed-loop circulatory computational modeling framework<sup>144</sup> (**Figure 3.1A**) was used to simulate the effects of HFpEF. In this framework, the LV was modeled using the finite element (FE) method, in which descriptors of tissue-level passive mechanical behavior<sup>57</sup> and active cellular-level cross-bridge cycling<sup>133</sup> were applied to a realistic 3D ventricular geometry to simulate a beating LV. This framework has been validated against key organ-level physiological behaviors such as a load-independent linear end-systolic pressure–volume relationship (ESPVR), a load-independent linear myocardial oxygen consumption (MVO<sub>2</sub>) vs pressure–volume area (PVA) relationship, and a strain waveform that is consistent with *in-vivo* measurements. Details of this modeling framework are given in chapter 2.

### **3.2.2 Left ventricular geometry and boundary conditions**

An idealized prolate ellipsoid was used to model the LV typical of that found in normal humans and hypertensive HFpEF patients. Clinical studies have shown that for hypertensive HFpEF patients, the LV has both increased wall thickness to cavity diameter (internal dimension) ratio and apex-to-base length compared to healthy subjects.<sup>112,141</sup> To reflect these differences, the unloaded LV geometry (that corresponds to zero cavity pressure) applied in the modeling framework to simulate HFpEF also had a thicker wall and a longer length compared to that used

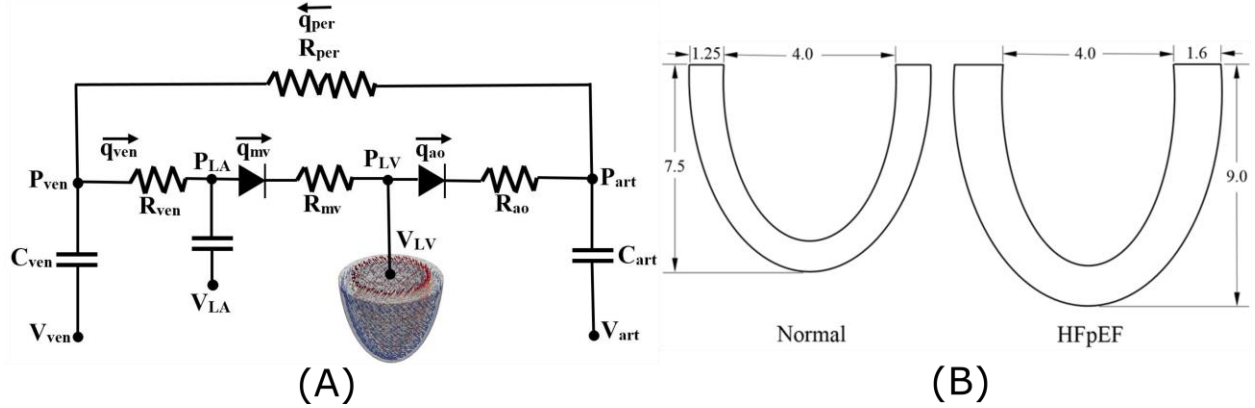


**Figure 3.1.** (A) Schematic of the computational framework consisting of a LV FE model coupled to a closed loop lumped parameter circulatory model. For a detailed description of the model parameters, refer to Shavik *et al.*<sup>144</sup>, (B) Schematic of the normal and HFpEF unloaded LV geometry (all dimensions are in cm).

to simulate the LV of normal humans (**Figure 3.1B**). The same boundary conditions as in previous computational models<sup>46,171</sup> were applied in all simulations. The myofiber direction (helix angle) was varied transmurally across the LV wall with a linear variation from  $60^\circ$  at the endocardium to  $-60^\circ$  at the epicardium based on a previous experimental measurement.<sup>153</sup>

### 3.2.3 Simulation cases

A *normal* case was first simulated so that the LV geometrical features at end-diastole and end-systole, hemodynamics and global longitudinal strain were close (within 1 standard deviation) to the values reported in controls subjects in the clinical studies.<sup>63,93,112</sup> We then simulated a number of cases to isolate the effects of both hypothesized and established factors deemed to affect longitudinal strain in HFpEF, namely, changes in 1) active tension developed by the tissue (i.e., myocardial contractility), 2) ventricular afterload as indexed by arterial resistance, 3) LV geometry and passive stiffness and 4) combinations of these factors. LV geometry was changed as described above. Active tension and afterload were changed, respectively, by scaling the active stress ( $T_{ref}$ ) generated during the cross-bridge cycling process and the peripheral resistance ( $R_{per}$ ) as described

**Table 3.1.** Simulation cases in this study.

Case	Change(s) relative to normal	Prescribed parameter value			
		Passive stiffness $C$ (Pa)	Active tension $T_{ref}$ (kPa)	Peripheral resistance $R_{per}$ (kPa ms ml <sup>-1</sup> )	
<i>Normal</i>	N/A	110	400	155	
HFpEF	<i>G</i>	Geo; ↑ passive stiffness	155	NC	NC
	<i>GC1</i>	Geo; ↑ passive stiffness; 30% ↓ tension		280	NC
	<i>GC2</i>	Geo; ↑ passive stiffness; 50% ↓ tension		200	NC
	<i>GC3</i>	Geo; ↑ passive stiffness; 70% ↓ tension		120	NC
	<i>GA1</i>	Geo; ↑ passive stiffness; 100% ↑ resistance		NC	310
	<i>GA2</i>	Geo; ↑ passive stiffness; 150% ↑ resistance		NC	387.5
	<i>GA3</i>	Geo; ↑ passive stiffness; 200% ↑ resistance		NC	465
	<i>GCA</i>	Geo; ↑ passive stiffness; 30% ↓ tension; 15% ↑ resistance		200	201.5

\*Geo: geometrical changes in Fig. 3.1B; NC: No change.

in Shavik *et al.*<sup>144</sup> All simulation cases are summarized with labels in **Table 3.1**. In case *G*, we considered only the effects of changes in the LV geometry and passive mechanical behavior typically found in HFpEF patients;  $T_{ref}$  and  $R_{per}$  had the same values as in the *normal* case. Because diastolic dysfunction accompanied by cardiac fibrosis is a hallmark of HFpEF patients<sup>8,24,178</sup>, the end-diastolic pressure-volume relationship (EDPVR) found in HFpEF patients is typically steeper compared to that found in normal humans. To model this effect, the passive stiffness scaling factor of the LV FE model ( $C$  parameter in Eq. 3 of Shavik *et al.*<sup>144</sup>) was prescribed to be higher than the value in the *normal* case (155 Pa vs. 110 Pa). Additionally, preload in this case was also prescribed to be higher than that in the *normal* case by setting a lower venous resting volume<sup>144</sup> ( $V_{ven,0} = 2900$  vs. 3400 ml) in the lumped circulatory model to match the clinically measured end-diastolic volume (EDV). An additional case *GSS* was considered with slightly higher passive stiffness scaling factor (120 Pa vs. 110 Pa) to determine the effects of passive stiffness on PV loops and

myocardial strains (**Figure 3.2**) In cases *GC1*, *GC2* and *GC3*, active tension  $T_{\text{ref}}$  was reduced by 30%, 50% and 70%, respectively, from the value in the *normal case* in addition to changes in the LV geometry, passive mechanical behavior and preload as described in case *G*. Peripheral resistance  $R_{\text{per}}$  (i.e., afterload) in these 3 cases had the same value as in the *normal case*. Conversely in cases *GA1*, *GA2* and *GA3*,  $R_{\text{per}}$  was increased by 100%, 150% and 200%, respectively, from the value in the *normal case* in addition to changes in the LV geometry, passive mechanical behavior and preload as described in the case *G*. Active tension of the tissue  $T_{\text{ref}}$  in these 3 cases had the same value as in the *normal case*. Finally, for case *GCA*, active tension  $T_{\text{ref}}$  and peripheral resistance  $R_{\text{per}}$  were both reduced and increased by 30% and 15%, respectively from their values in the *normal case* in addition to the changes in LV geometry, passive mechanical behavior and preload as in the case *G*. Heart rate was set constant at 67 bpm for all simulations, consistent with data reported in prior studies (e.g., 69.5 vs. 66 bpm in Kraigher-Krainer *et al*<sup>93</sup> and 68 vs. 67 bpm in Maurer *et al*<sup>112</sup>).

### 3.2.4 Analysis of pressure-volume loops and strains

Pressure-volume loops were obtained for each simulation case over a range of preload pressures, from which we could define end-systolic and end-diastolic pressure-volume relationships (ESPVR and EDPVR, respectively). ESPVRs were linear, whereas EDPVRs were nonlinear, and these relationships were fit to the following regression equations:

$$P_{\text{ESPVR}}(V) = E_{\text{es}}(V - V_0), \quad (3.1a)$$

$$P_{\text{EDPVR}}(V) = A(e^{B(V-V_0)} - 1). \quad (3.1b)$$

In the above equations,  $E_{\text{es}}$  (mmHg/ml) is the end-systolic elastance (i.e., slope of ESPVR),  $V_0$  (ml) is the volume-intercept,  $V$  (ml) is the LV cavity volume, whereas  $A$  (mmHg) and  $B$  (ml<sup>-1</sup>) are,

respectively, the scaling and exponent parameters describing the EDPVR.

Global longitudinal, circumferential and radial strains were calculated using the method described in Shavik *et al*<sup>144</sup> with end-diastole serving as the reference configuration. Myofiber stretch in the longitudinal, circumferential and radial directions, denoted respectively by  $e_l$ ,  $e_c$  and  $e_r$ , were first computed by

$$\lambda_i = \sqrt{\mathbf{e}_i \cdot \mathbf{C} \cdot \mathbf{e}_i}. \quad (3.2)$$

In the above equation,  $\mathbf{C} = \mathbf{F}^T \mathbf{F}$  is the right Cauchy-Green deformation tensor,  $\mathbf{F}$  is the deformation gradient tensor and  $\mathbf{e}_i$  with  $i \in (l, c, r)$  are the unit vectors in the longitudinal  $l$ , circumferential  $c$  and radial  $r$  directions, respectively. The radial direction  $\mathbf{e}_r$  was defined to be normal to the LV wall, whereas the circumferential direction  $\mathbf{e}_c$  was defined to be orthogonal to  $\mathbf{e}_r$  and the apex to base direction. The longitudinal direction  $\mathbf{e}_l$  was then defined to be orthogonal to both  $\mathbf{e}_r$  and  $\mathbf{e}_c$ . The Biot strain, which is more akin to the strain reported in echo-based studies,<sup>144</sup> was then calculated using:

$$\varepsilon_{ii} = (\lambda_i - 1) \times 100\%. \quad (3.3)$$

### 3.3 Results

#### 3.3.1 Effects of changes in geometry, passive stiffness and preload

Model predictions of LV geometrical features at end-diastole of the *normal* and altered geometry (i.e.,  $G$ ) cases compared to those measured in clinical studies<sup>63,112</sup> are summarized in **Table 3.2**. The model predictions were largely consistent with measurements, which show an increase in both LV wall thickness and apex-to-base length that were accompanied by a small change in internal chamber diameter.

**Table 3.2.** Left ventricular geometry at end-diastole.

Parameter	Normal			Case <i>G</i>		
	Model	Clinical		Model	Clinical	
		Maurer et al. <sup>112</sup>	He et al. <sup>63</sup>		Maurer et al. <sup>112</sup>	He et al. <sup>63</sup>
Internal diameter (cm)	4.8	4.7±0.5	4.5±0.3	4.7	4.6±0.5	4.7±0.6
Length (cm)	8.1	10.6±1.1	NR	9.6	11.4±1.2	NR
Wall thickness (cm)	1.0	1.0±0.1*	0.9±0.1*	1.25	1.3±0.3*	1.1±0.2*

\*Posterior wall thickness; NR = Not reported

**Table 3.3.** Parameters related to ESPVR and EDPVR calculated by regression analysis.

Parameter	Normal	HFpEF					
		<i>G</i>	<i>GC1</i>	<i>GC2</i>	<i>GC3</i>	<i>GA1-3</i>	<i>GCA</i>
End-systolic elastance $E_{es}$ (mmHg/mL)	3.9	5.2	4.1	2.8	1.8	5.2	4.1
Volume intercept of ESPVR, $V_0$ (mL)	10.0	13.0	13.0	13.0	13.0	13.0	13.0
Scaling factor of EDPVR $A$ (mmHg)	0.012				0.026		
Exponent of EDPVR $B$ (ml <sup>-1</sup> )	0.07				0.07		

Pressure-volume loops of the LV for the *normal* and altered geometry (*G*) cases revealed that purely changing LV geometry and passive stiffness to those found in HFpEF patients resulted in slightly steeper ESPVR and EDPVR with slightly increased  $V_0$  (**Figure 3.2A, Table 3.3**). Since there were simultaneous increases of both  $E_{es}$  and  $V_0$  in case *G*, the net shifts of the ESPVR and EDPVR compared to the normal case were relatively subtle. Changing the geometry, passive stiffness and preload to those found in HFpEF patients also produced slight increases in the peak longitudinal and circumferential strains by 1% (absolute) and 0.4% (absolute), respectively (**Figure 3.2B and 3.2C**). In addition, peak radial strain decreased by 1.4% (**Figure 3.2D**) compared to the *normal* case. Comparison of the cases *G* and *GSS* shows that the effect of passive stiffness on strains and PV loop is small in HFpEF.

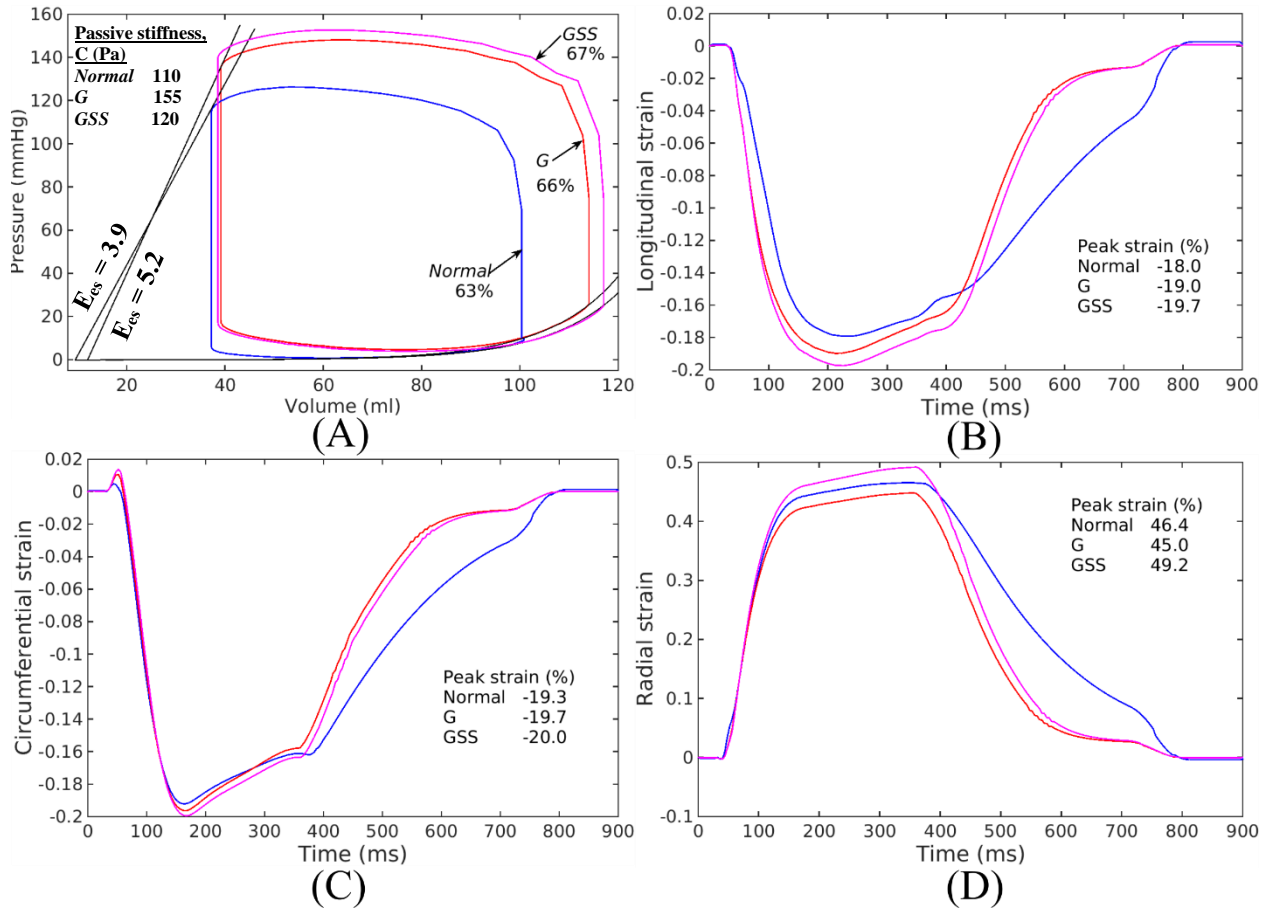


**Figure 3.2** (A) PV loops (numbers with percentage indicate EF), (B) global longitudinal, (C) circumferential and (D) radial strains for *normal*, *G* and *GSS* cases. Refer to Table 3.1 for description of the simulation cases. Case *GSS* has same geometry, active tension and afterload resistance as case *G*. Only passive stiffness *C* was decreased in case *GSS* (120Pa in case *GSS* vs. 155Pa in case *G*) to determine its effect on PV loop and strains.

### 3.3.2 Effects of changes in active tension

The impact of decreasing myocardial contractility by decreasing active tension ( $T_{ref}$ ) by 30% (case GC1), 50% (case GC2) and 70% (case GC3) in addition to changes in LV geometry produced PV loops with less pressure generation (decreased height) and with less stroke volume (decreased width). Correspondingly, end-systolic volumes (ESV) increased while EF,  $E_{es}$  and all 3 strain components decreased (**Figure 3.3**). Actual changes of the EFs and strains are indicated in the figure insets.

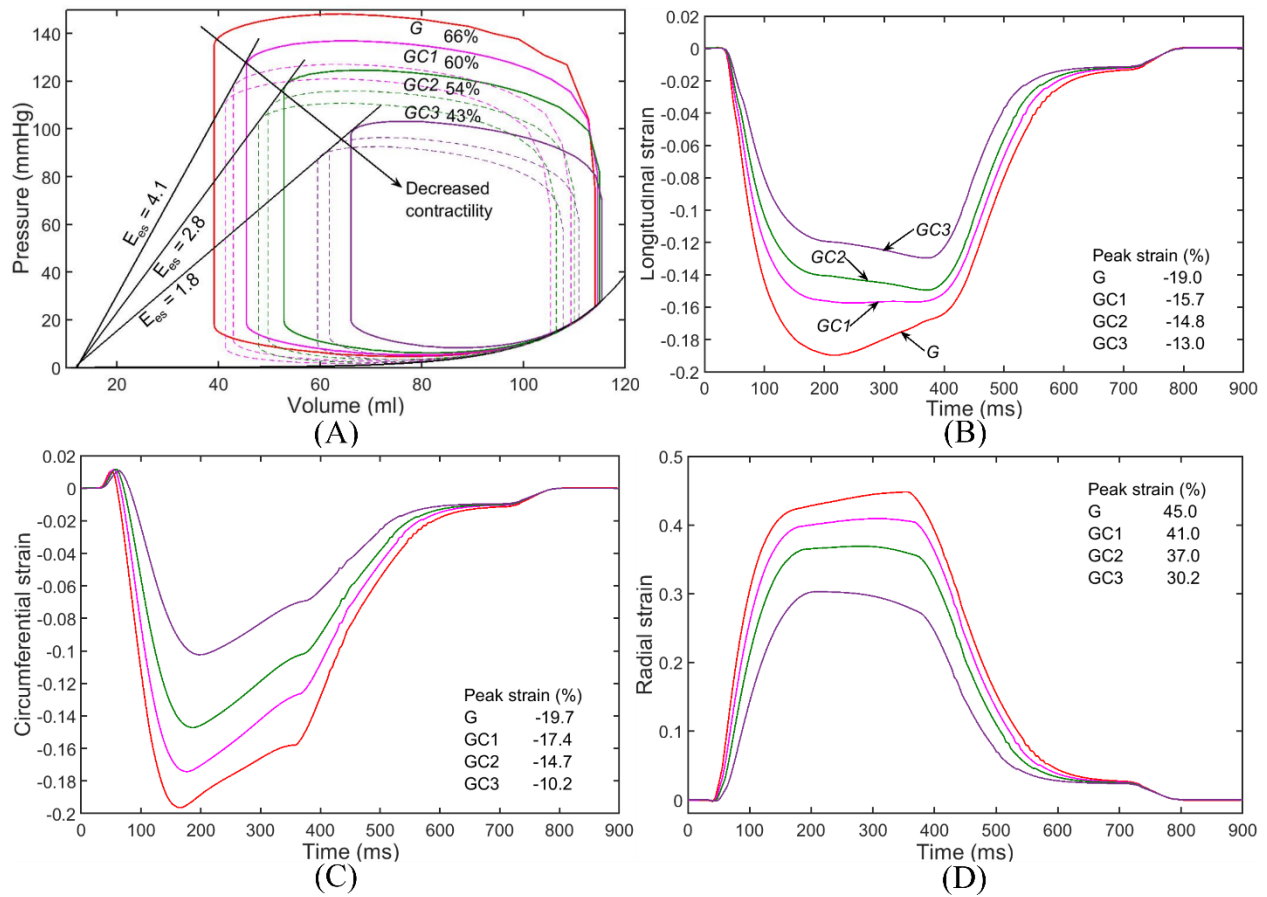


**Figure 3.3.** (A) PV loops (numbers with percentage indicate EF), (B) global longitudinal, (C) circumferential and (D) radial strain waveforms for cases *GC1*, *GC2* and *GC3* when  $T_{ref}$  was decreased by 30%, 50% and 70%, respectively. Dotted lines in (A) denote PV loops (at different preload) used for computing  $E_{es}$ .

### 3.3.3 Effects of changes in afterload resistance

Increasing peripheral resistance  $R_{per}$  (i.e., afterload) by 100% (case *GA1*), 150% (case *GA2*) and 200% (case *GA3*) while keeping active tension  $T_{ref}$  at the original value as in the *normal* case led to progressive increases in pressure generation as well as decreases in both stroke volume and EF compared to case *G* (**Figure 3.4A**). However, ESPVRs and EDPVRs were not affected by changes in peripheral resistance since these are load independent measures of ventricular chamber properties. Myocardial strains were also all reduced with increasing  $R_{per}$  (**Figures 3.4B, C and D**; quantitative details are summarized in figure insets). Importantly, increasing  $R_{per}$  over this broad

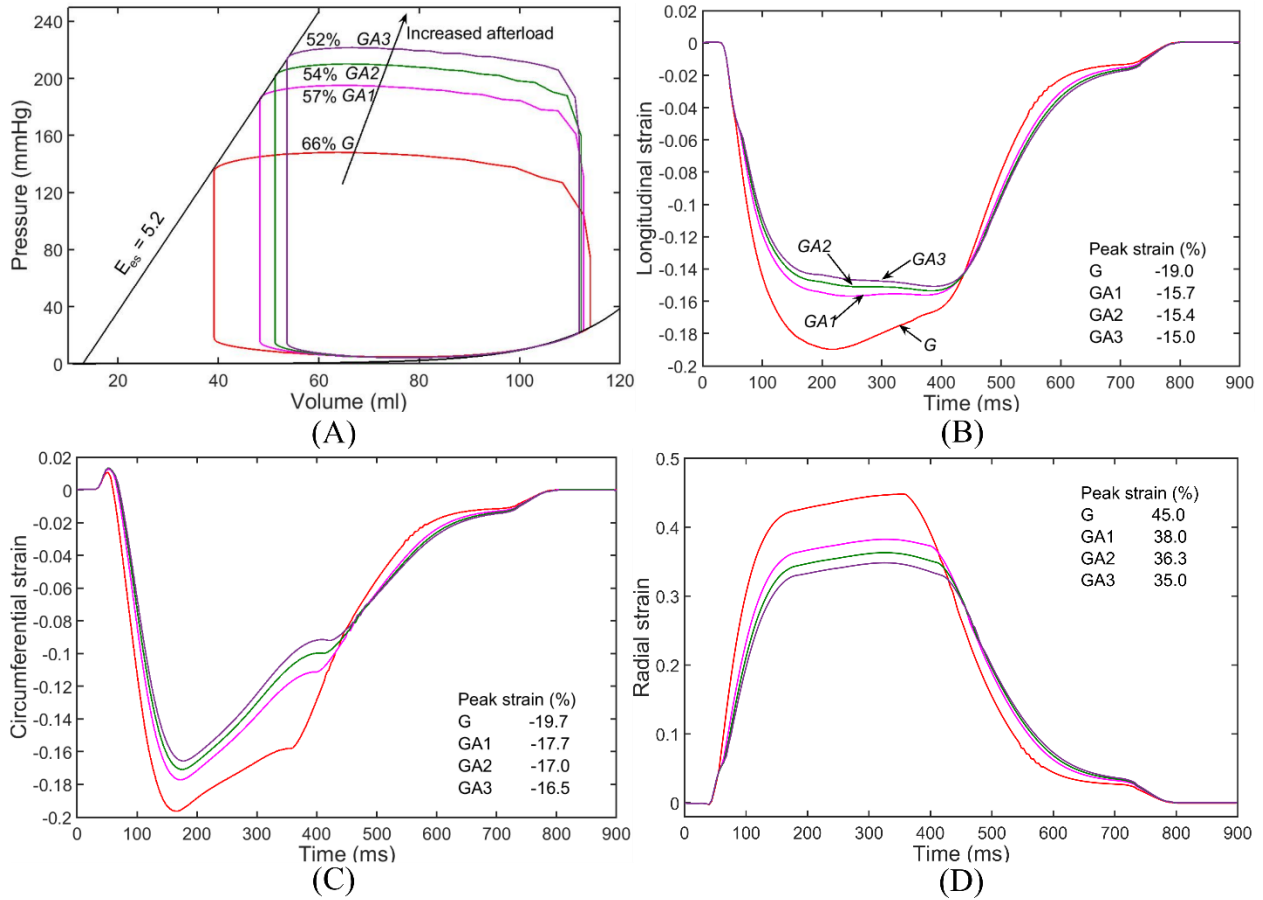


**Figure 3.4.** (A) PV loops (numbers with percentage indicate EF), (B) longitudinal, (C) circumferential and (D) radial strain for cases *GA1*, *GA2* and *GA3* when  $R_{per}$  was increased by 100%, 150% and 200%, respectively.

range had significantly less effects on the myocardial strains compared to when active tension was decreased (**Figure 3.3**).

### 3.3.4 Effects of simultaneous changes of both peripheral resistance and active tension

As will be detailed further in the next section and based on the insights derived from the simulations presented above, we simultaneously modified parameter values to closely simulate conditions (volume, EF, strains, blood pressures) encountered in HFpEF patients reported in the literature. We arrived at a solution based on a simultaneous decrease of  $T_{ref}$  by 30% and an increase of  $R_{per}$  by 15% (case *GCA*) (**Figure 3.5**).

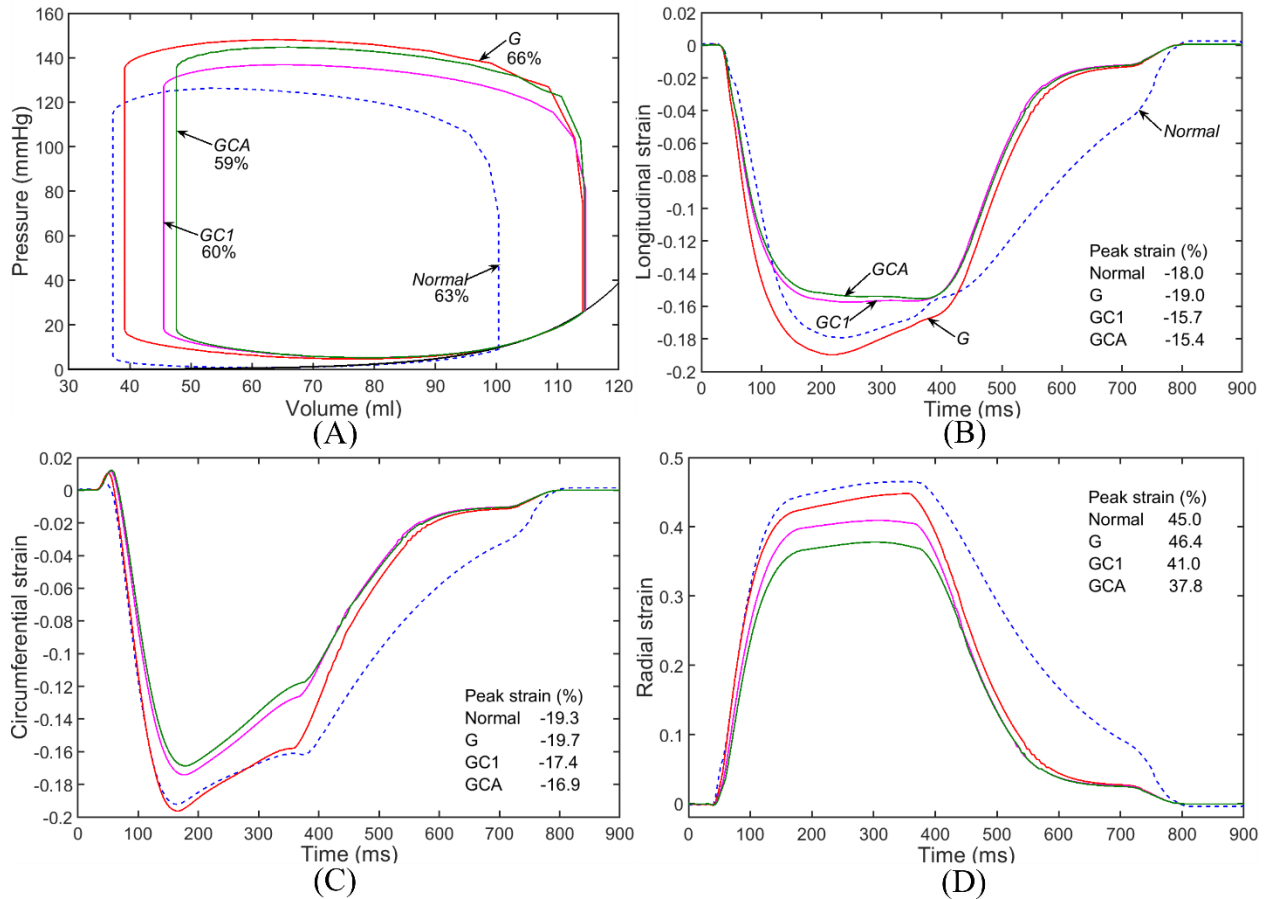


**Figure 3.5.** Comparison of (A) PV loops (numbers with percentage indicate EF), (B) longitudinal, (C) circumferential and (D) radial strain of the *GCA* case (30% decrease of  $T_{ref}$  + 15% increase in  $R_{per}$ ) with cases *GC1* (30% decrease in  $T_{ref}$ ), case *G* and *normal*.

### 3.3.5 Comparison of geometry, hemodynamics and strains with clinical measurements

Model predictions of EDV and ESV for the *normal* and HFpEF cases all fell within the range of clinical measurements (**Figure 3.6**). Similar to what is observed in the clinics where hypertensive HFpEF patients have larger EDVs and ESVs compared to normal subjects,<sup>93,112</sup> the model also predicted the EDV and ESV to be larger in all the HFpEF cases. Other than case *GC3*, all other HFpEF cases have EF greater than or equal to 50% and were within the range measured clinically in patients.

In terms of LV hemodynamics (**Figure 3.7**), only cases *G*, *GC2* and *GCA* had both systolic blood pressure (SBP) and diastolic blood pressure (SBP) within 1 standard deviation of the clinical

measurements made in HFpEF patients. While case *GC1* had SBP within the clinical range, its DBP was slightly higher than the measurements. Out of these 3 cases that had hemodynamic measurements within the clinical range, only cases *GC2* and *GCA*, in which active tension  $T_{ref}$  was reduced, had peak global longitudinal strains that were within one standard deviation of the mean values measured in HFpEF patients (**Figure 3.8**). While the global longitudinal strain in the simulation cases with increased afterload (*GA1*, *GA2* and *GA3*) were all within one standard deviation of the clinically measured value, their peak SBP (195 – 225 mmHg) and DBP (135 – 165 mmHg) blood pressure were both well beyond the range measured clinically (**Figure 3.7**).

Thus, the only scenario that simultaneously matched LV EF, systolic and diastolic blood pressures and longitudinal strain was case *GCA*, in which the HFpEF geometry was combined with increased afterload resistance and decreased myocardial force generation.

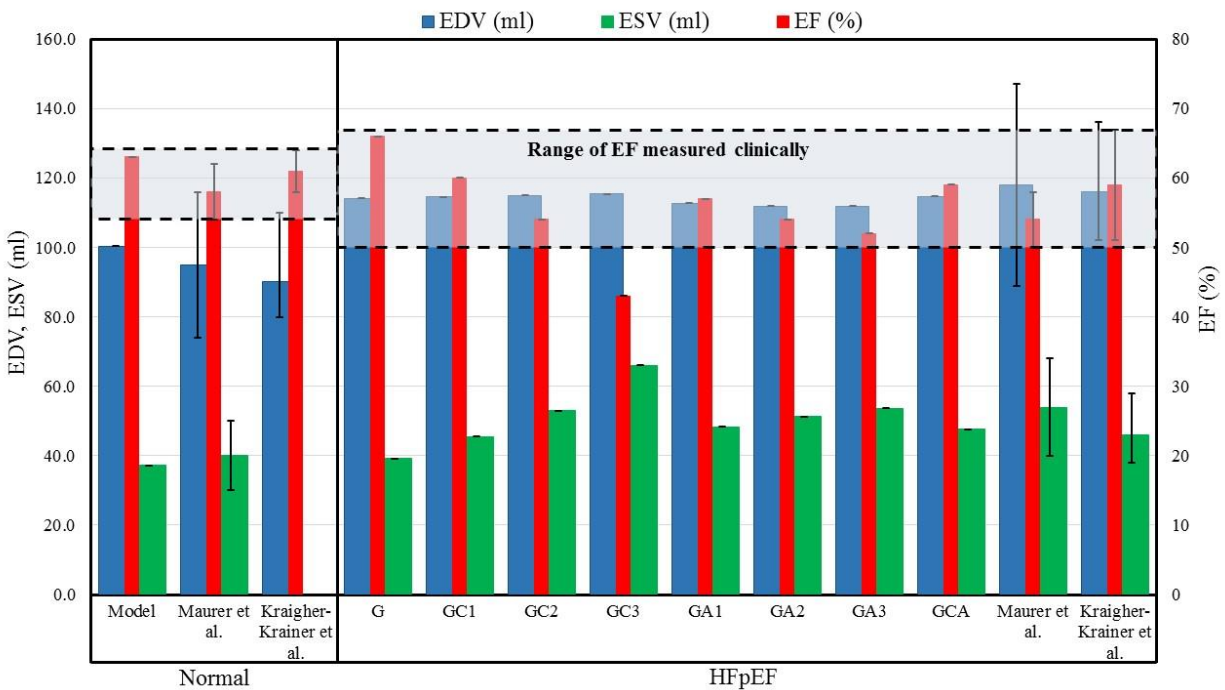


**Figure 3.6.** Comparison of model predictions of EDV, ESV and EF from all the simulation cases with clinical measurements.<sup>93,112</sup>

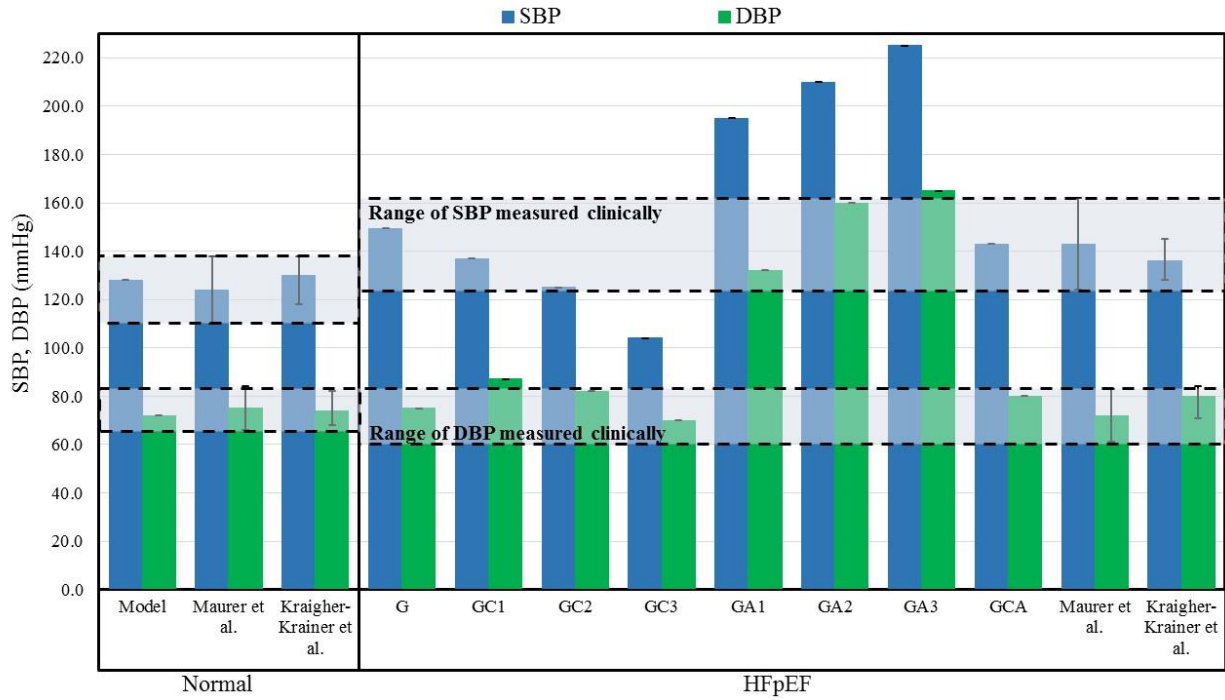


**Figure 3.7.** Comparison of model predictions of SBP and DBP in all the simulation cases with clinical measurements.<sup>93,112</sup>

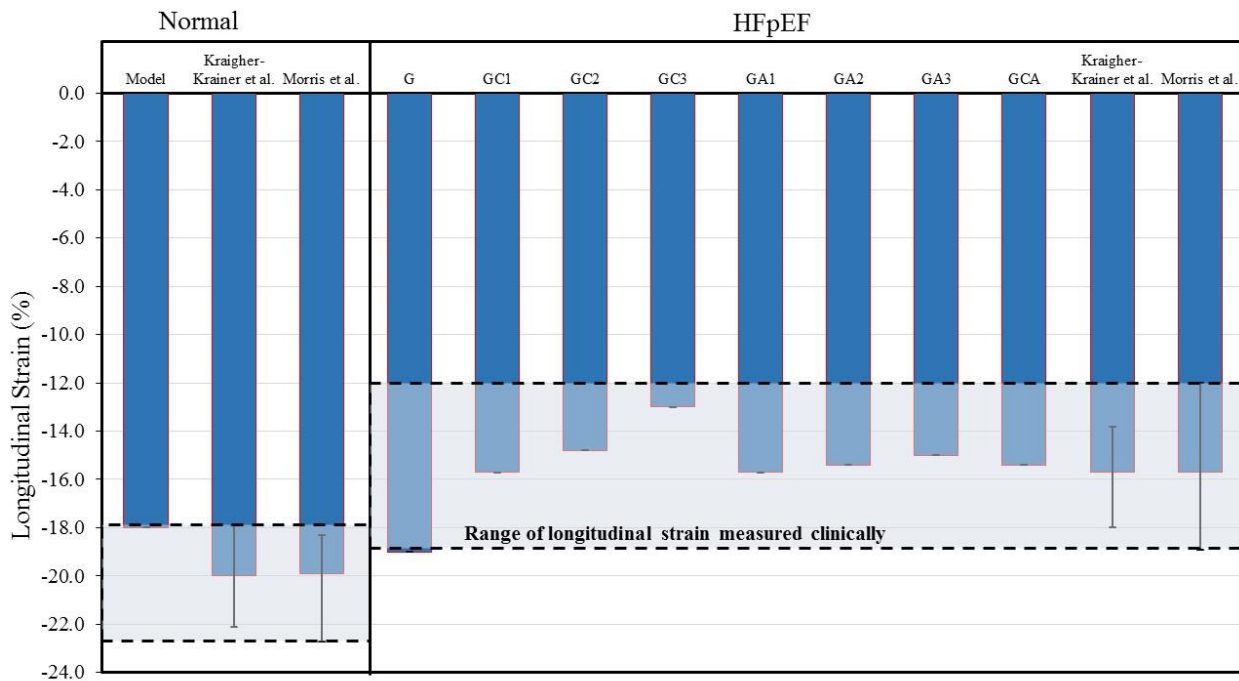


**Figure 3.8.** Comparison of model predictions of peak longitudinal strains with clinical measurements.<sup>93,118</sup>

### 3.4 Discussion

We used a previously described computational modeling framework<sup>144</sup> to determine if reduced longitudinal strain observed in patients with hypertension and HFpEF was due to reduced myocardial contractility or if it was related to accompanying altered geometry and/or afterload resistance. We first showed that a mere change in LV geometry and passive stiffness from those found in normal humans to those found in HFpEF patients without any changes of active myocardial tension generation leads to only subtle net changes in the ESPVR, indicative of preserved LV chamber contractility. That is, chamber contractility was not significantly affected by simultaneous increases in LV wall thickness and apex-to-base length<sup>112</sup>; such changes only produce a slight increase in the global peak circumferential and longitudinal strains, suggesting that myocardial strains are relatively insensitive to geometrical changes associated with HFpEF. We also note that we have also explored and found that the effects of passive stiffness on myocardial strains are small. Second, although a moderate reduction in active tension  $T_{\text{ref}}$  superimposed on a change in both the LV geometry and passive mechanical behavior (case *GCI*) reduced the myocardial strains, it still produced an increase in  $E_{\text{es}}$  relative to normal. Third, the impaired global longitudinal strains found in HFpEF patients<sup>93,118</sup> can be reproduced by a reduction in active tension or an increase in afterload but the latter was associated with a substantial increase in SBP and DBP that were well beyond the range measured in the patients. Finally, it was only with the combination of a decrease in myocardial contractility and a moderate increase in afterload (case *GCA*) that simultaneously produced an increase in SBP, a decrease in global longitudinal and circumferential strain, a maintenance of LV EF<sup>93</sup>, and an increase in  $E_{\text{es}}$ ,<sup>76</sup> all in the same magnitudes as found in HFpEF patients.

Due in part to the heterogeneity of clinical characteristics encountered in HFpEF patients, the pathophysiology of HFpEF is likely to be multifactorial<sup>30,135</sup> and arguably more complex than HFrEF. It is difficult, if not impossible, to unravel the relative contributions of these multiple factors to changes in longitudinal strain purely from clinical observations or experiments. Computational modeling, on the other hand, is an important tool that can serve this purpose. While there are some computational modeling studies on HFpEF,<sup>36,45,108</sup> these existing studies, to the best of our knowledge, have not comprehensively assessed the contributions of changes in afterload, tissue active tension and geometry to abnormalities in both hemodynamics (SBP and DBP) and functional indices ( $E_{es}$  and longitudinal strain) found in HFpEF patients.

Left ventricular end-systolic elastance,  $E_{es}$ , is widely considered to be the “gold standard” load-independent index for assessing LV chamber contractility.<sup>28</sup> In HFpEF patients,  $E_{es}$  is typically increased or normal compared to healthy subjects.<sup>22,76</sup> Increases as much as 154% (from 2.2 to 5.6 mmHg/ml)<sup>76</sup> have been reported. However, values of *myocardial* contractility-related indices such as longitudinal and circumferential strains,<sup>93</sup> radial strain<sup>169</sup> and myocardial velocities measured from tissue Doppler imaging are reported to be reduced.<sup>162</sup> As succinctly described by Bourlag et al.<sup>23</sup>: “*The coexistence of elevated  $E_{es}$  and reduced systolic function by other indices has been difficult to reconcile.*” As detailed above, the present findings reconcile these findings.

These model predictions compare favorably with measurements of myocyte active tension from biopsy samples of hypertensive patients exhibiting diastolic dysfunction and concentric LV remodeling.<sup>19,39</sup> Specifically in patients undergoing coronary bypass grafting, maximum developed isometric tension of isolated myocytes was found to be about 50% lower in those exhibiting hypertension, concentric remodeling but with normal EF compared to those without hypertension ( $10.67 \pm 1.38$  vs.  $20.64 \pm 3.29$  mN/mm<sup>2</sup>)<sup>39</sup>; this is regardless of whether the patients

had heart failure or not. Similarly, myocyte isometric tension was also found to be lower (though not statistically significant) in patients who had hypertension and diastolic heart failure compared to the recipients of heart transplants ( $20.3 \pm 7.5$  vs.  $24.2 \pm 12.4$  kN/m<sup>2</sup>).<sup>19</sup>

While we have shown that a decrease in longitudinal strain with preserved or increased  $E_{es}$  as found in HFpEF patients can be produced by a reduction in the tissue active tension  $T_{ref}$ , our model also predicted that this strain reduction can also be produced by an increase in ventricular afterload achieved by increasing the peripheral resistance parameter  $R_{per}$ . Indeed, hypertension is a major contributor to the development of HFpEF, with a prevalence of 55–86% in HFpEF patients.<sup>96</sup> Patients diagnosed with HFpEF typically have high SBP with some studies reporting average values of 149 mmHg,<sup>41</sup> 153 mmHg<sup>176</sup> and 136 mmHg.<sup>93</sup> The accompanied increase in afterload may be due (at least in part) to arterial stiffening,<sup>131,157</sup> which we have shown previously using a coupled ventricular-vascular modeling framework to produce a substantial increase in systolic blood pressure.<sup>143</sup> To achieve a decrease in longitudinal strain comparable to those found in HFpEF patients without any reduction in  $T_{ref}$  would, however, require an increase in  $R_{per}$  that produces a SBP of around 195-225 mmHg that is well beyond the range found in these patients. Based on our model predictions, it is, therefore, unlikely that the reduction in longitudinal strain found in HFpEF patients is due solely to an increase in afterload without any decrease in the active tension developed by the myocytes. It is likely that the concurrent increase in SBP and decrease in longitudinal strain is produced by a combination of an increase in afterload with reduced active tension of the myocytes (case *GCA*).

This finding is also largely consistent with previous modeling studies, with one suggesting that the active tension of myocytes is reduced at the subendocardial region but is increased at the

subepicardial region in the LV of HFpEF patients,<sup>36</sup> and the other suggesting the systolic contractile force is reduced in HFpEF due to abnormal calcium homeostasis.<sup>3</sup>

### **3.4.1 Limitations**

The current findings need to be interpreted within the context of potential limitations. First, we have assumed the LV geometry to be an idealized truncated ellipsoid (for simplicity), and consequently, did not consider any asymmetrical geometrical differences (e.g., focal hypertrophy of the interventricular septum<sup>78</sup>) or possible effects of the right ventricle. Second, we did not consider any alterations to myofiber orientation in HFpEF (employing a standard gradient of +60° at the endocardium to -60° at the epicardium) since there are no available data to suggest that these angles are altered. Third, we have focused only on peak myocardial strains and not the time course of the strain waveform that may be affected by impaired relaxation of the myocytes as found in some studies of HFpEF.<sup>23</sup> Fourth, we have only considered ventricular properties under resting conditions. However, symptoms and hemodynamic abnormalities of many HFpEF patients are manifested and exaggerated even during mild exertion. Whether this reflects an alteration of intrinsic ventricular properties or a more complex interplay between peripheral and ventricular properties is currently unknown and not addressed in the present analysis. Finally, we have focused largely on modeling features from the data acquired in a number of clinical studies<sup>93,112,118</sup> that do not distinguish between the time course of HFpEF. As such, the findings here reproduce the observations in a cross-section of HFpEF patients, and do not correspond to any specific etiology and or time point during disease progression. Future studies with longitudinal data will be able to help characterize the time course of the alteration of ventricular properties in HFpEF patients.

## CHAPTER 4

### **Image based biventricular modeling framework of pulmonary arterial hypertension (PAH)**

#### **4.1 Introduction**

Pulmonary arterial hypertension (PAH) is a debilitating disease that is characterized by an abnormally elevated pulmonary artery (PA) pressure ( $> 25$  mmHg). Without treatment PAH progresses rapidly and adversely affects the right ventricle (RV) function, eventually leading to heart failure and death<sup>69</sup>. The elevated PA and RV pressure due to a high afterload in PAH can cause unusual ventricular deformation, such as a left ventricular septal bow (LVSB) in which the septum wall bulges towards the left ventricle (LV). Moreover, long-term functional, structural, and geometrical changes such as enlargement of the RV also occur as the disease progresses. Left ventricular assist devices (LVAD) have been successfully used in the past to treat patients who have left heart failure. Recently, right ventricular assist device (RVAD) has been proposed as a treatment for PAH patients to unload the RV. Because the RV is different from the LV in terms of its structure, geometry and operation, the effects of RVAD on RV may be different from that of LVAD on the LV. Few studies, however, have investigated the effects of RVAD and all computational studies have neglected the effect of RVAD on the ventricular mechanics.

To address these limitations, we present a computational framework consisting of a patient-specific biventricular finite element (FE) model that is coupled to a lumped parameter model describing both the pulmonary and systemic circulations in a closed-loop system. The biventricular FE model was reconstructed from magnetic resonance (MR) images and the computational framework was calibrated against measurements of the pressure and volume waveforms acquired from two PAH patients with different stages of remodeling as well as a normal subject. An RVAD

model based on a realistic pump characteristic was also incorporated into the calibrated computational framework to investigate its effects on ventricular stresses and deformation in the patients. The framework described here lays the foundation for subsequent development of patient-specific computational heart models to elucidate the complex ventricular interdependence<sup>53</sup> and pulmonic-systemic interactions associated with PAH and its treatments. This work has been accepted in the journal mechanics research communications.

## 4.2 Methods

### 4.2.1 Image and data acquisition

Cine MR images from one normal human subject and two PAH patients were acquired using a 3T Philips scanner. The characteristics of these 3 patients are given in **Table 4.1**. Among the two PAH patients, the RV of one patient underwent severe remodeling, which was evident from the large RV end-diastolic volume (EDV) to LV EDV ratio<sup>7</sup>. We denote this patient as PAHR in this study. The second PAH patient had RV chamber size and RV EDV to LV EDV ratio close to that found in the normal subject. We denote this patient as PAHN. Right heart catheterization (RHC) was performed on the PAH patients to acquire the left and right ventricular, atrial and arterial pressure. All enrolled participants gave their written consent and all data were acquired in the National Heart Center of Singapore.

We segment the LV endocardial, RV endocardial and epicardial surfaces at different time points in the cardiac cycle from the short and long-axis views of the cine MR images of the PAH patients and normal subject using the medical image analysis software MeVisLab (<http://www.mevislab.de>)<sup>174</sup>. Patient-specific LV and RV cavity volume waveforms over a cardiac cycle were obtained from these surfaces. As in a previous study, these volume vs. time curves

**Table 4.1.** Characteristics of the normal and PAH patients

	<b>Normal</b>	<b>PAHR</b>	<b>PAHN</b>
HR, bpm	75	58	76
LV EDV, ml	83	84	84
LV ESV, ml	27	31	32
LV EF, %	67	63	62
MAP, mmHg	-	100	99.7
RV EDV, ml	102	147	79
RV ESV, ml	42	92	39
RV EF, %	59	37	51
RVEDV/LVEDV	1.2	1.75	0.95
mPAP, mmHg	-	47.7	32.3

<sup>a</sup>MAP (mean arterial pressure) and mPAP (mean pulmonary artery pressure) were calculated by the formula (systolic pressure + 2\*diastolic pressure)/3. <sup>b</sup>HR: heart rate; LV: left ventricle; RV right ventricle; EDV: end-diastolic volume; ESV: end-systolic volume; EF: ejection fraction; PAHR: PAH with remodeling (RVEDV/LVEDV >1.5); PAHN: PAH with normal RVEDV/LVEDV

were synchronized with the pressures measured from RHC in the PAH patients to obtain the LV and RV pressure-volume (PV) loops. Because invasive RHC was not performed on the normal subject, a normal RV pressure waveform and a scaled LV pressure waveform (with end-systolic pressure equal to 0.9 of the measured cuff pressure) were used as surrogate for the normal subject and paired with the measured cavity volumes to obtain the LV and RV PV loops<sup>174</sup>.

#### 4.2.2 Biventricular geometry and microstructure

Finite element meshes associated with the biventricular geometry for the three cases (Normal, PAHR and PAHN) were generated from the volume enclosed by the segmented epicardial, LV endocardial and RV endocardial surfaces at the cardiac time point corresponding to the lowest pressure using GMSH<sup>47</sup>. These meshes served as the unloaded configuration of the biventricular unit of the normal subject and PAH patients (**Figure 4.1**). Approximately 5800 quadratic tetrahedral elements and 18000 nodes were used in the FE meshes to discretize the biventricular geometries. Using a Laplace-Dirichlet Rule-Based algorithm<sup>17</sup>, the myofiber helix angle was prescribed to vary linearly in the transmural direction across the LV wall from 60° at the

endocardium to  $-60^\circ$  at the epicardium based on previous experimental measurements<sup>153</sup>. The RV free wall myofiber orientation was assumed to be same due to the lack of experimental measurements in humans.

### 4.2.3 Closed loop circulatory model

The biventricular FE models were coupled to a closed loop lumped parameter circulatory model that describes both systemic and pulmonary circulations (**Figure 4.2A**). The modeling framework consists of eight compartments with four cardiovascular components (ventricle, atrium, artery and vein) each in the systemic and pulmonary circulation. Conservation of total mass of blood in the circulatory model requires the net change of inflow and outflow rates of each compartment be related to the rate of change of the volume by the following relation

$$\frac{dV_{LV}(t)}{dt} = q_{mv}(t) - q_{av}(t), \quad (4.1a)$$

$$\frac{dV_{sa}(t)}{dt} = q_{av}(t) - q_{sa}(t), \quad (4.1b)$$

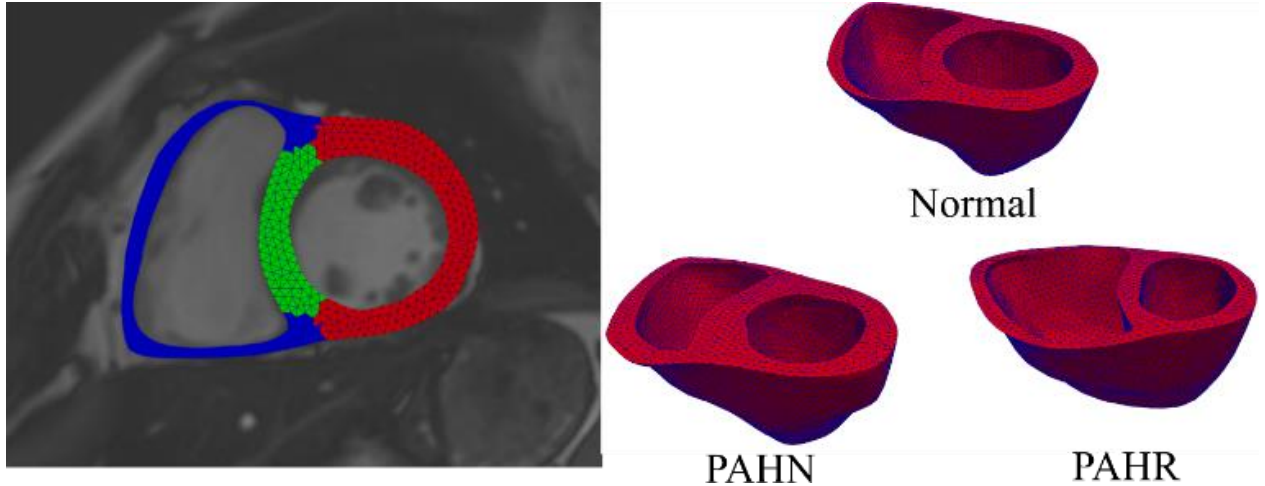


**Figure 4.1.** Left: Biventricular FE geometry reconstructed from MR images with LVFW (red), septum (green), and RVFW (blue) material regions. Right: Unloaded FE geometry of normal, PAHN and PAHR cases respectively.



$$\frac{dV_{pv}(t)}{dt} = q_{pa}(t) - q_{pv}(t), \quad (4.1g)$$

$$\frac{dV_{LA}(t)}{dt} = q_{pv}(t) - q_{mv}(t). \quad (4.1h)$$

In Eqn. (4.1),  $V_{LV}$ ,  $V_{sa}$ ,  $V_{sv}$ ,  $V_{RA}$ ,  $V_{RV}$ ,  $V_{pa}$ ,  $V_{pv}$  and  $V_{LA}$  are the volumes of the eight compartments with the subscripts denoting the left ventricle (LV), systemic artery (sa), systemic vein (sv), right atrium (RA), right ventricle (RV), pulmonary artery (pa), pulmonary vein (pv), and left atrium (LA), respectively. Flow rates at different segments of the circulatory model are denoted by  $q_{mv}$ ,  $q_{av}$ ,  $q_{sa}$ ,  $q_{sv}$ ,  $q_{tv}$ ,  $q_{pvv}$ ,  $q_{pa}$  and  $q_{pv}$  (**Figure 4.2A**), whereas flow rate of the RVAD is denoted by  $q_{RVAD}$ .

To model the RVAD, we used the pressure gradient – flow characteristics of the Synergy™ continuous flow miniature pump (CircuLite Inc, Saddle Brook, NJ) with operating speeds between 20 to 28krpm (**Figure 4.2B**). This pump has the characteristics that are well suited for RVAD application<sup>73</sup> and was applied in a previous study<sup>128</sup>. Flow through the RVAD was sourced from the RV and ejected to the pulmonary artery. For a particular operating speed, the RVAD flow rate was determined from the characteristics curve based on the pressure gradient across the pulmonary artery and RV i.e.,

$$q_{RVAD}(t) = \frac{-K_1[P_{pa}(t) - P_{RV}(t)] + K_2}{R_{can}}. \quad (4.2)$$

In Eqn. (4.2),  $K_1$  and  $K_2$  are constants determined from the RVAD pump characteristics at a prescribed operating speed,  $P_{pa}$  is the pulmonary artery pressure,  $P_{RV}$  is the RV pressure, and  $R_{can}$  is the total resistance of the inlet and outlet cannula connecting the pump to the RV and pulmonary artery, respectively. On the other hand, the systemic and pulmonary arteries and veins were

modelled using their electrical analogs based on Ohm's law. At each segment, the flowrate depends on the pressure gradient and resistance to the flow as described in the following equation

$$q_{mv}(t) = \begin{cases} \frac{P_{LA}(t) - P_{LV}(t)}{R_{mv}} & \text{when, } P_{LA}(t) \geq P_{LV}(t) \\ 0 & \text{when, } P_{LA}(t) < P_{LV}(t) \end{cases}, \quad (4.3a)$$

$$q_{av}(t) = \begin{cases} \frac{P_{LV}(t) - P_{Sa}(t)}{R_{av}} & \text{when, } P_{LV}(t) \geq P_{Sa}(t) \\ 0 & \text{when, } P_{LV}(t) < P_{Sa}(t) \end{cases}, \quad (4.3b)$$

$$q_{sa}(t) = \frac{P_{Sa}(t) - P_{Sv}(t)}{R_{sa}}, \quad (4.3c)$$

$$q_{sv}(t) = \frac{P_{Sv}(t) - P_{RA}(t)}{R_{sv}}, \quad (4.3d)$$

$$q_{tv}(t) = \begin{cases} \frac{P_{RA}(t) - P_{RV}(t)}{R_{tv}} & \text{when, } P_{RA}(t) \geq P_{RV}(t) \\ 0 & \text{when, } P_{RA}(t) < P_{RV}(t) \end{cases}, \quad (4.3e)$$

$$q_{pvv}(t) = \begin{cases} \frac{P_{RV}(t) - P_{pa}(t)}{R_{pvv}} & \text{when, } P_{RV}(t) \geq P_{pa}(t) \\ 0 & \text{when, } P_{RV}(t) < P_{pa}(t) \end{cases}, \quad (4.3f)$$

$$q_{pa}(t) = \frac{P_{pa}(t) - P_{pv}(t)}{R_{pa}}, \quad (4.3g)$$

$$q_{pv}(t) = \frac{P_{pv}(t) - P_{LA}(t)}{R_{pv}}. \quad (4.3h)$$

In Eqn. (4.3),  $R_{mv}$ ,  $R_{av}$ ,  $R_{tv}$  and  $R_{pvv}$  are the resistances associated with the mitral, aortic, tricuspid and pulmonary valves, respectively. On the other hand, the vessel resistances are denoted by  $R_{sa}$ ,  $R_{sv}$ ,  $R_{pa}$  and  $R_{pv}$ , respectively. To describe the compliance of the systemic and pulmonary vessels, we used the following pressure-volume relationships

$$P_{sa}(t) = \frac{V_{sa}(t) - V_{sa,0}}{C_{sa}}, \quad (4.4a)$$

$$P_{sv}(t) = \frac{V_{sv}(t) - V_{sv,0}}{C_{sv}}, \quad (4.4b)$$

$$P_{pa}(t) = \frac{V_{pa}(t) - V_{pa,0}}{C_{pa}}, \quad (4.4c)$$

$$P_{pv}(t) = \frac{V_{pv}(t) - V_{pv,0}}{C_{pv}}, \quad (4.4d)$$

where  $V_{sa,0}$ ,  $V_{sv,0}$ ,  $V_{pa,0}$ , and  $V_{pv,0}$  are the resting volumes of the systemic and pulmonary vessels, and  $C_{sa}$ ,  $C_{sv}$ ,  $C_{pa}$ , and  $C_{pv}$  are their corresponding total compliance.

Contraction of the LA and RA was modeled using a time varying elastance function that is given by the following pressure – volume relations

$$P_k(t) = e(t)P_{es,k}(V_k(t)) + (1 - e(t))P_{ed,k}(V_k(t)), \quad (4.5a)$$

where,

$$P_{es,k}(V_k(t)) = E_{es,k}(V_k(t) - V_{0,k}), \quad (4.5b)$$

$$P_{ed,k}(V_k(t)) = A_k (e^{B_k(V_k(t) - V_{0,k})} - 1). \quad (4.5c)$$

In Eqn. (4.5), the subscript  $k$  denotes either *LA* or *RA*. The volume, end-systolic elastance, and volume-intercept of the end-systolic pressure-volume relationship (ESPVR) of the corresponding atrium are denoted by  $V_k$ ,  $E_{es,k}$  and  $V_{0,k}$ , respectively. The parameters  $A_k$  and  $B_k$  define the atrium curvilinear end-diastolic pressure volume relationship (EDPVR) and the driving function is defined as

$$e(t) = \begin{cases} \frac{1}{2} \left( \sin \left[ \left( \frac{\pi}{t_{max}} \right) t - \frac{\pi}{2} \right] + 1 \right); & 0 < t \leq 3/2 t_{max} \\ \frac{1}{2} e^{-(t-3/2 t_{max})/\tau}; & t > 3/2 t_{max}, \end{cases}, \quad (4.6)$$

where  $t_{max}$  is the point of maximal chamber elastance and  $\tau$  is the time constant of relaxation.

Last, the relationships between pressure and volume of the LV and RV were computed from the biventricular FE model (see next section), which can be expressed as a non-closed form function i.e.,

$$P_{RV}(t), P_{LV}(t) = f^{BiV}(V_{LV}(t), V_{RV}(t)). \quad (4.7)$$

#### 4.2.4 Finite element formulation

The weak form associated with the biventricular FE model was derived based on minimization of the following Lagrangian functional

$$\begin{aligned} \mathcal{L}(\mathbf{u}, p, P_{LV}, P_{RV}, \mathbf{c}_1, \mathbf{c}_2) = & \int_{\Omega_0} W(\mathbf{u}) dV - \int_{\Omega_0} p(J - 1) dV - P_{LV}(V_{LV,cav}(\mathbf{u}) - V_{LV}) + \\ & P_{RV}(V_{RV,cav}(\mathbf{u}) - V_{RV}) - \mathbf{c}_1 \cdot \int_{\Omega_0} \mathbf{u} dV - \mathbf{c}_2 \cdot \int_{\Omega_0} \mathbf{X} \times \mathbf{u} dV, \end{aligned} \quad (4.8)$$

where  $\Omega_0$  is the reference configuration of the biventricular unit,  $\mathbf{u}$  is the displacement field,  $P_{LV}$  and  $P_{RV}$  are, respectively, the Lagrange multipliers that constrain the LV cavity volume  $V_{LV,cav}(\mathbf{u})$  to a prescribed value  $V_{LV}$  and the RV cavity volume  $V_{RV,cav}(\mathbf{u})$  to a prescribed value  $V_{RV}$ <sup>124</sup>. We note that  $V_{LV}$  and  $V_{RV}$  are prescribed from the closed-loop circulatory model in Eqn. (4.7). The Lagrange multiplier  $p$  was used to enforce incompressibility of the tissue (i.e., Jacobian of the deformation gradient tensor  $J = 1$ ). The vectors  $\mathbf{c}_1$  and  $\mathbf{c}_2$  are Lagrange multipliers applied to constrain, respectively, the rigid body translation (i.e., zero mean translation) and rotation (i.e., zero mean rotation)<sup>125</sup>. In Eqn. (4.8),  $\mathbf{X}$  denotes a material point in  $\Omega_0$  and  $W$  is the

strain energy function of the myocardial tissue. The cavity volume of the LV and RV were obtained from the displacement field by using the following functional relationship ( $k = LV$  or  $RV$ )

$$V_{k,cav}(\mathbf{u}) = \int_{\Omega_{inner,k}} dv_k = -\frac{1}{3} \int_{\Gamma_{inner,k}} \mathbf{x} \cdot \mathbf{n} da_k, \quad (4.9)$$

where  $\Omega_{inner,k}$  is the volume enclosed by the inner surface  $\Gamma_{inner,k}$  of the LV or RV, and  $\mathbf{n}$  denotes the outward unit normal vector of those surfaces. Taking the first variation of the Lagrangian functional given in Eqn. (4.8) leads to

$$\begin{aligned} \delta\mathcal{L}(\mathbf{u}, p, P_{LV,cav}, P_{RV,cav}, \mathbf{c}_1, \mathbf{c}_2) = & \int_{\Omega_0} (\mathbf{P} - p\mathbf{F}^{-T}) : \nabla \delta\mathbf{u} dV - \int_{\Omega_0} \delta p (J - 1) dV - (P_{LV,cav} + \\ & P_{RV,cav}) \int_{\Omega_0} \text{cof}(\mathbf{F}) : \nabla \delta\mathbf{u} dV - \delta P_{LV,cav} (V_{LV,cav}(\mathbf{u}) - V_{LV}) - \delta P_{RV,cav} (V_{RV,cav}(\mathbf{u}) - V_{RV}) - \\ & \delta\mathbf{c}_1 \cdot \int_{\Omega_0} \mathbf{u} dV - \delta\mathbf{c}_2 \cdot \int_{\Omega_0} \mathbf{X} \times \mathbf{u} dV - \mathbf{c}_1 \cdot \int_{\Omega_0} \delta\mathbf{u} dV - \mathbf{c}_2 \cdot \int_{\Omega_0} \mathbf{X} \times \delta\mathbf{u} dV. \end{aligned} \quad (4.10)$$

In Eqn. (4.10),  $\mathbf{P}$  is the first Piola Kirchhoff stress tensor and  $\mathbf{F}$  is the deformation gradient tensor. The variations of the displacement field, Lagrange multiplier for enforcing incompressibility and volume constraint, zero mean translation and rotation are denoted by  $\delta\mathbf{u}$ ,  $\delta p$ ,  $\delta P_{LV,cav}$ ,  $\delta P_{RV,cav}$ ,  $\delta\mathbf{c}_1$ , and  $\delta\mathbf{c}_2$ , respectively. Together with the constraint that the basal deformation at  $z = 0$  is in-plane in the biventricular unit, the solution of the Euler-Lagrange problem was obtained by finding  $\mathbf{u} \in H^1(\Omega_0)$ ,  $p \in L^2(\Omega_0)$ ,  $P_{LV,cav} \in \mathbb{R}$ ,  $P_{RV,cav} \in \mathbb{R}$ ,  $\mathbf{c}_1 \in \mathbb{R}^3$ ,  $\mathbf{c}_2 \in \mathbb{R}^3$  that satisfies

$$\delta\mathcal{L}(\mathbf{u}, p, P_{LV,cav}, P_{RV,cav}, \mathbf{c}_1, \mathbf{c}_2) = 0, \quad (4.11a)$$

$$\mathbf{u}(x, y, 0) \cdot \mathbf{n}|_{base} = 0, \quad (4.11b)$$

for all  $\delta\mathbf{u} \in H^1(\Omega_0)$ ,  $\delta p \in L^2(\Omega_0)$ ,  $\delta P_{LV,cav} \in \mathbb{R}$ ,  $\delta P_{RV,cav} \in \mathbb{R}$ ,  $\delta\mathbf{c}_1 \in \mathbb{R}^3$ ,  $\delta\mathbf{c}_2 \in \mathbb{R}^3$ .

#### 4.2.5 Mechanical behavior of the cardiac tissue

Mechanical behavior of the myocardial tissue was described by an active stress formulation in which the first Piola stress tensor  $\mathbf{P}$  in Eqn. (4.10) was additively decomposed into a passive and an active component, i.e.

$$\mathbf{P} = \mathbf{P}_p + P_a \mathbf{e}_f \otimes \mathbf{e}_{f_0}. \quad (4.12)$$

In Eqn. (4.12),  $\mathbf{P}_p$  is the passive stress tensor,  $P_a$  is the magnitude of the active stress, whereas  $\mathbf{e}_f$  and  $\mathbf{e}_{f_0}$  are the local basis vectors that define the cardiac muscle fiber directions in the current and reference configuration, respectively. The passive stress tensor  $\mathbf{P}_p$  is related to the strain energy function  $W_p$  and deformation gradient tensor  $\mathbf{F}$  by

$$\mathbf{P}_p = \frac{dW_p}{d\mathbf{F}}. \quad (4.13)$$

A Fung-type transversely-isotropic hyperelastic strain energy function<sup>57</sup>

$$W_p = \frac{1}{2} C (e^Q - 1), \quad (4.14a)$$

with

$$Q = b_{ff} E_{ff}^2 + b_{xx} (E_{ss}^2 + E_{nn}^2 + E_{sn}^2 + E_{ns}^2) + b_{fx} (E_{fn}^2 + E_{nf}^2 + E_{fs}^2 + E_{sf}^2). \quad (4.14b)$$

was prescribed. In Eqn. (4.14b),  $E_{ij}$  with  $(i, j) \in (f, s, n)$  denote the components of the Green-Lagrange strain tensor  $\mathbf{E} = \frac{1}{2} (\mathbf{F}^T \mathbf{F} - \mathbf{I})$  with  $f, s, n$  denoting the myofiber, sheet and sheet normal directions, respectively. Material parameters of the Fung-type constitutive model are  $C$ ,  $b_{ff}$ ,  $b_{xx}$  and  $b_{fx}$ .

To describe the active stress behavior, a previously developed active contraction model<sup>80</sup> was used. The magnitude of the active stress  $P_a$  was described by

$$P_a = \frac{l_s}{l_{s0}} f^{iso}(l_c) f^{twitch}(t, l_s) (l_s - l_c) E_a, \quad (4.15)$$

where  $l_s$  is the sarcomere length,  $l_c$  is the length of the contractile element,  $l_{s0}$  is the sarcomere length in a prescribed reference state (relaxed sarcomere length), and  $E_a$  is the stiffness of the serial elastic element. The function  $f^{iso}(l_c)$  denotes the dependency of the isometrically developed active stress on  $l_c$  and is given by

$$f^{iso}(l_c) = \begin{cases} T_0 \tanh^2[a_6(l_c - a_7)] & \text{when, } l_c < a_7 \\ 0 & \text{when, } l_c > a_7 \end{cases}, \quad (4.16)$$

where  $T_0$  is a model parameter that scales the active tension. Both  $a_6$  and  $a_7$  are model parameters.

The time course of the active tension development is controlled by

$$f^{twitch}(t, l_s) = \begin{cases} 0 & \text{when, } t < 0 \\ \tanh^2\left(\frac{t}{t_r}\right) \tanh^2\left(\frac{t_{max}-t}{t_d}\right) & \text{when, } 0 < t < t_{max} \\ 0 & \text{when, } t > 0, \end{cases} \quad (4.17a)$$

$$t_{max} = b(l_s - l_d). \quad (4.17b)$$

In Eqn. (4.17),  $t_r$  is the activation rise time constant,  $t_d$  is the activation decay time constant,  $b$  relates activation duration  $t_{max}$  to the sarcomere length  $l_s$ , and  $l_d$  is the sarcomere length at the start of the activation time, i.e., when  $t_{max} = 0$ . The time course of the contractile element  $l_c$  was expressed by an ordinary differential equation

$$\frac{\partial l_c}{\partial t} = [E_a(l_s - l_c) - 1]v_0, \quad (4.18)$$

where  $v_0$  is the unloaded shortening velocity. The sarcomere length  $l_s$  was calculated from the myofiber stretch  $\lambda$  and the relaxed sarcomere length  $l_{s0}$  by

$$\lambda = \sqrt{\mathbf{e}_{f_0} \cdot \mathbf{F}^T \mathbf{F} \mathbf{e}_{f_0}}, \quad (4.19a)$$

$$l_s = \lambda l_{s0}. \quad (4.19b)$$

#### 4.2.6 Model parameterization and simulation of the cardiac cycles

In the 3 cases, the biventricular FE models were divided into three material regions, namely the LV free wall (LVFW), the septum and the RV free wall (RVFW). Similar to a previous study<sup>40</sup>, passive stiffness  $C$  and contractility  $T_0$  were prescribed to be the same in the LVFW and septum (denoted as  $C_{LV}$  and  $T_{0,LV}$ ) but had different values in the RVFW (denoted as  $C_{RV}$  and  $T_{0,RV}$ ). For each FE models, the parameters were adjusted to fit the experimentally measured LV and RV PV loops, volume and pressure waveforms throughout the cardiac cycle. Specifically, the LV and RV end diastolic pressures were matched by adjusting the passive parameters  $C_{LV}$  and  $C_{RV}$ . The regional contractility parameters ( $T_{0,LV}$ ,  $T_{0,RV}$ ) were adjusted to match the LV and RV systolic pressures and stroke volumes. On the other hand, the contraction model parameters  $t_r$ ,  $t_d$  and  $b$  were adjusted to match the time course of the volume and pressure waveforms measured in the LV and RV. Circulatory model parameters (resistances and compliances) were also adjusted to match the systolic pressure (afterload), preload and systemic and pulmonary vein pressures. All the model parameters are listed in **Table 4.2**. The model is implemented using FEnICS<sup>6</sup> and the code is publicly available ([https://bitbucket.org/shaviksh/biv\\_rvad/src/master/](https://bitbucket.org/shaviksh/biv_rvad/src/master/)).

Steady-state pressure-volume loop was established by running the simulation over several cardiac cycles. The cardiac cycle time was prescribed based on the measured heart rate in each of the cases.

**Table 4.2.** Model parameters for Normal and PAH cases.

	<b>Normal</b>	<b>PAHR</b>	<b>PAHN</b>
Passive material model	$C_{LV} = 0.1\text{Pa}$ , $C_{RV} = 1.0\text{Pa}$	$C_{LV} = 4.0\text{Pa}$ , $C_{RV} = 30\text{Pa}$	$C_{LV} = 7\text{Pa}$ , $C_{RV} = 57\text{Pa}$
Active contraction model	$T_{0,LV} = 800\text{kPa}$ , $T_{0,RV} = 195\text{kPa}$ , $t_r = 310\text{ms}$ , $t_d = 150\text{ms}$ , $b = 0.22\text{ms}\cdot\mu\text{m}^{-1}$	$T_{0,LV} = 500\text{kPa}$ , $T_{0,RV} = 220\text{kPa}$ , $t_r = 320\text{ms}$ , $t_d = 100\text{ms}$ , $b = 0.24\text{ms}\cdot\mu\text{m}^{-1}$	$T_{0,LV} = 650\text{kPa}$ , $T_{0,RV} = 430\text{kPa}$ , $t_r = 320\text{ms}$ , $t_d = 100\text{ms}$ , $b = 0.24\text{ms}\cdot\mu\text{m}^{-1}$
Circulatory model	$C_{sa} = 0.005\text{Pa}\cdot\text{ml}$ , $C_{pa} = 0.2\text{Pa}\cdot\text{ml}$ , $C_{sv} = 0.3\text{Pa}\cdot\text{ml}$ , $C_{pv} = 0.09\text{Pa}\cdot\text{ml}$ , $R_{sa} = 132\text{kPa}\cdot\text{ms}\cdot\text{ml}^{-1}$ , $R_{pa} = 7\text{kPa}\cdot\text{ms}\cdot\text{ml}^{-1}$ , $R_{sv} = R_{pv} = 2\text{kPa}\cdot\text{ms}\cdot\text{ml}^{-1}$ , $R_{av} = 3\text{kPa}\cdot\text{ms}\cdot\text{ml}^{-1}$ , $R_{mv} = 0.9\text{kPa}\cdot\text{ms}\cdot\text{ml}^{-1}$ , $R_{tv} = 0.4\text{kPa}\cdot\text{ms}\cdot\text{ml}^{-1}$ , $R_{pvv} = 2\text{kPa}\cdot\text{ms}\cdot\text{ml}^{-1}$ , $V_{sa,0} = 610\text{ml}$ , $V_{pa,0} = 50\text{ml}$ , $V_{sv,0} = 3315\text{ml}$ , $V_{pv,0} = 400\text{ml}$	$C_{sa} = 0.0055\text{Pa}\cdot\text{ml}$ , $C_{pa} = 0.006\text{Pa}\cdot\text{ml}$ , $C_{sv} = 0.3\text{Pa}\cdot\text{ml}$ , $C_{pv} = 0.09\text{Pa}\cdot\text{ml}$ , $R_{sa} = 265\text{kPa}\cdot\text{ms}\cdot\text{ml}^{-1}$ , $R_{pa} = 115\text{kPa}\cdot\text{ms}\cdot\text{ml}^{-1}$ , $R_{sv} = R_{pv} = 2\text{kPa}\cdot\text{ms}\cdot\text{ml}^{-1}$ , $R_{av} = 3\text{kPa}\cdot\text{ms}\cdot\text{ml}^{-1}$ , $R_{mv} = 0.9\text{kPa}\cdot\text{ms}\cdot\text{ml}^{-1}$ , $R_{tv} = 0.4\text{kPa}\cdot\text{ms}\cdot\text{ml}^{-1}$ , $R_{pvv} = 2\text{kPa}\cdot\text{ms}\cdot\text{ml}^{-1}$ , $V_{sa,0} = 610\text{ml}$ , $V_{pa,0} = 400\text{ml}$ , $V_{sv,0} = 3335\text{ml}$ , $V_{pv,0} = 415\text{ml}$	$C_{sa} = 0.0053\text{Pa}\cdot\text{ml}$ , $C_{pa} = 0.0055\text{Pa}\cdot\text{ml}$ , $C_{sv} = 0.3\text{Pa}\cdot\text{ml}$ , $C_{pv} = 0.09\text{Pa}\cdot\text{ml}$ , $R_{sa} = 206\text{kPa}\cdot\text{ms}\cdot\text{ml}^{-1}$ , $R_{pa} = 82\text{kPa}\cdot\text{ms}\cdot\text{ml}^{-1}$ , $R_{sv} = R_{pv} = 2\text{kPa}\cdot\text{ms}\cdot\text{ml}^{-1}$ , $R_{av} = 3\text{kPa}\cdot\text{ms}\cdot\text{ml}^{-1}$ , $R_{mv} = 0.9\text{kPa}\cdot\text{ms}\cdot\text{ml}^{-1}$ , $R_{tv} = 0.4\text{kPa}\cdot\text{ms}\cdot\text{ml}^{-1}$ , $R_{pvv} = 2\text{kPa}\cdot\text{ms}\cdot\text{ml}^{-1}$ , $V_{sa,0} = 590\text{ml}$ , $V_{pa,0} = 425\text{ml}$ , $V_{sv,0} = 3550\text{ml}$ , $V_{pv,0} = 280\text{ml}$

Specifically, a cycle time of 800ms (equivalent to 75 bpm), 1030ms (equivalent to 58 bpm) and 790ms (equivalent to 76 bpm) was prescribed in the simulations for the normal subject, PAHR and PAHN, respectively.

#### 4.2.7 Post processing of septum curvature

Regional curvature  $\kappa$  of the LVFW and septum was computed at each time point of the cardiac cycle by first fitting a curve to the 2D slice of the LV endocardial surface taken at the mid-ventricular level (halfway between the apex and the base) of the deformed mesh (**Fig. 4.2C**). Based on the fitted plane curve  $y = f(x)$  in the Cartesian coordinate system, the local curvature was then computed by

$$\kappa = \frac{|y''|}{(1+y'^2)^{3/2}} \quad (4.20)$$

where  $y'$  and  $y''$  are the 1<sup>st</sup> and 2<sup>nd</sup> derivative of the function  $y = f(x)$ .

## 4.3 Results

### 4.3.1 Comparison between simulations and measurements

The PV loops, volume and pressure waveforms of the LV and RV predicted by the model were closely matched with the measured data for the normal subject as well as the PAH patients (**Figure 4.3**). Specifically, the coefficient of determination  $R^2$  associated with the fitting of volume and pressure at all cardiac time points are 0.983 and 0.978, respectively (**Figure 4.3A**). Compared to the normal subject, the peak RV pressure was 2.5 times higher in the PAHR case (76 mmHg vs. 30 mmHg) and 1.8 times higher in the PAHN case (55 mmHg vs. 30 mmHg). The peak LV pressure was also increased slightly in the PAH patients compared to the normal (133 mmHg in PAHR and 137 mmHg in PAHN vs. 124 mmHg in normal). The LV end-diastolic and end-systolic volumes (EDV and ESV) were comparable between the normal and PAH cases, resulting in a large ejection fraction (EF) for all the cases (63% in PAHR and 62% in PAHN vs. 67% in normal). However, the PAHR case had significantly larger RV EDV (147 ml vs. 102 ml) and RV ESV (92 ml vs. 42 ml) compared to normal (and PAHN), which resulted in a substantially lower RV EF (37% vs. 59%). On the other hand, PAHN had slightly lower RV EDV (79 ml vs. 102 ml) and slightly larger RV ESV (39 ml vs. 42 ml) than the normal, which also resulted in a lower RV EF (51% vs. 59%).

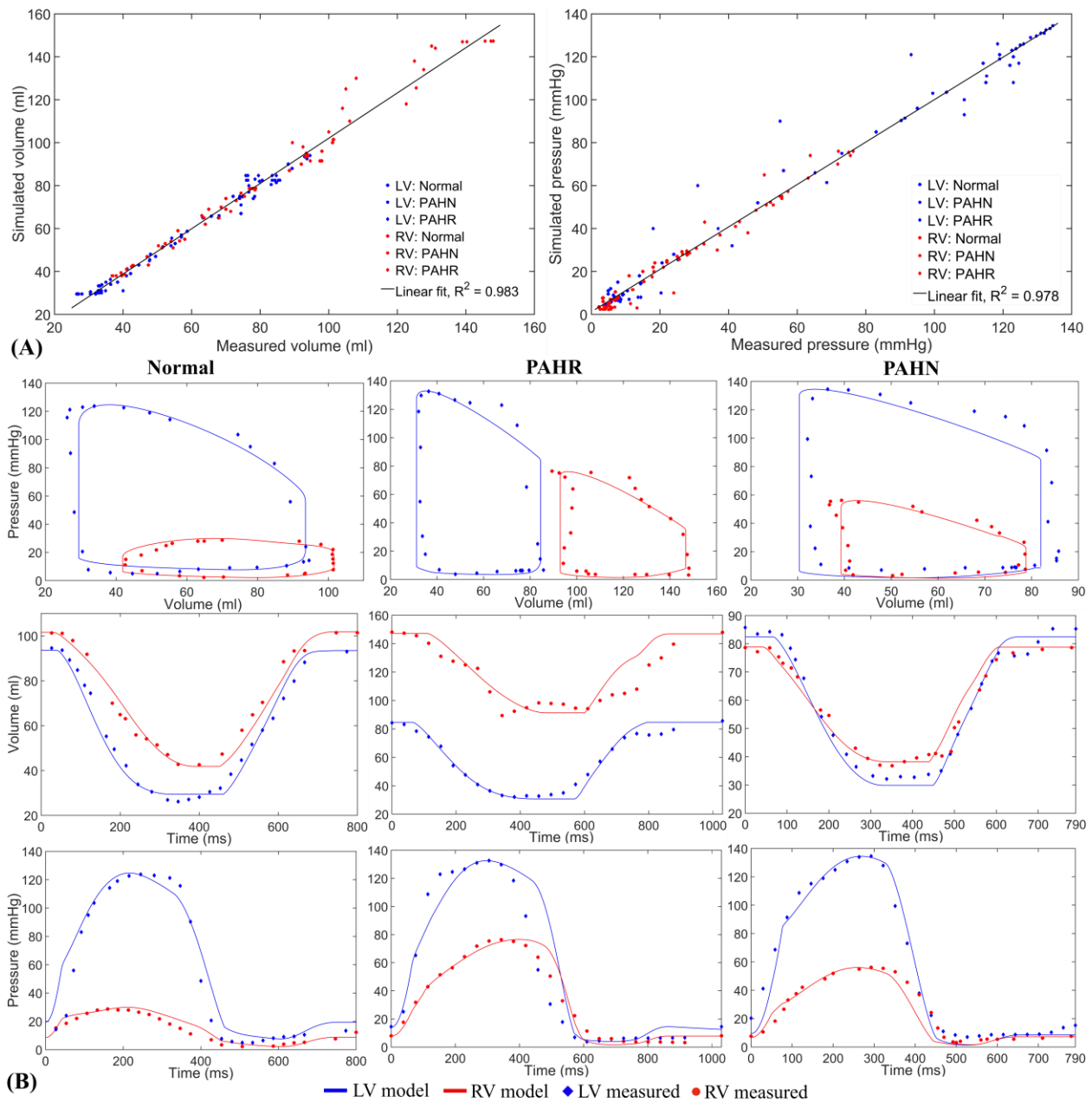


**Figure 4.3.** (A) Scatter plot of the simulated vs. measured volume (left) and pressure (right) at all cardiac time points for the three cases. A  $y = x$  line is also plotted to show the zero-error reference. (B) Measurements and model predictions of LV and RV PV loops (first row), volume waveforms (2<sup>nd</sup> row) and pressure waveforms (3<sup>rd</sup> row) for the normal, PAH patient with severe RV remodeling (PAHR) and PAH patient with normal RV (PAHN).

### 4.3.2 Effect of RVAD on hemodynamics

Implantation of RVAD in the PAH patients produced a triangular shaped RV PV loop without any isovolumic (contraction and relaxation) phases as well as a lower RV EDV and RV ESV compared to the baseline (no RVAD) (**Figure 4.4A**). With increasing RVAD speed, both RV EDV and RV ESV decreased progressively, with the PAHR case undergoing a larger decrease compared to the PAHN case. At the highest RVAD speed of 28 krpm, RV EDV was reduced by 18% and 11%, respectively, in the PAHR case (121 ml vs. 147 ml at baseline) and the PAHN case (70 ml vs. 79 ml at baseline). In the PAHR case, the RV peak pressure decreased moderately with increasing RVAD speed whereas it increased slightly in the PAHN case when RVAD speed was increased. Both LV EDV and peak pressure (**Figure 4.4B**) increased with RVAD speed for both PAH cases, and the increase was more evident in the PAHR case compared to the PAHN case. Cardiac output (CO) steadily improved for PAHR with RVAD flow reaching to 3.33 L/min. at 28krpm compared to 3.09 L/min. at baseline (no RVAD). In contrast, CO remained fairly constant at different RVAD operating speed up to 28 krpm in the PAHN case.

In terms of arterial hemodynamics, both PA diastolic and mean pressures (**Figure 4.4C**) increased with increasing RVAD speed. Specifically, at an RVAD speed of 28 krpm, the PA diastolic pressure increased by 69% (58.4 mmHg vs. 34.5 mmHg) and the mean PA pressure increased by 32% (63.3 mmHg vs. 48 mmHg) compared to baseline (no RVAD) in the PAHR case. The increase is more in the PAHN case at the same operating speed, where the PA diastolic pressure increased by 88% (41.4 mmHg vs. 22 mmHg) and mean PA pressure increased by 42% (46.6 mmHg vs. 32.8 mmHg). In addition, the RA pressure decreased by 40% (4.8 mmHg vs. 8 mmHg) for PAHR compared to baseline (no RVAD) at 28krpm, whereas, for PAHN case it

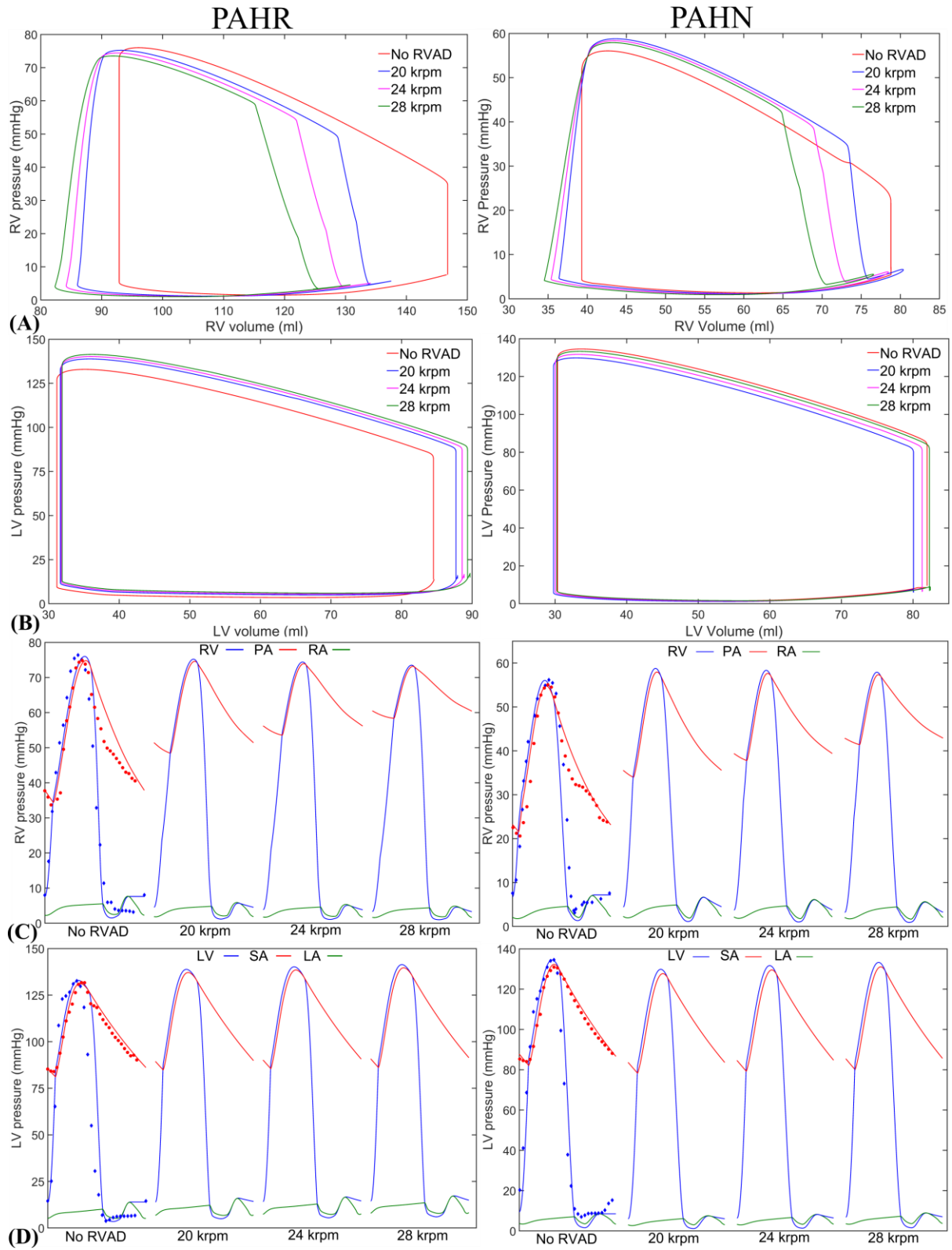


**Fig. 4.4.** (A) RV, (B) LV PV loops. (C) RV, PA and RA pressure waveforms. (D) LV, SA and LA pressure waveforms for the PAHR and PAHN cases with different RVAD speed. Scattered points show the measurements.

decreased by only 20% (5.6 mmHg vs. 7mmHg) at the same RVAD speed. Compared to PA pressure, the change in aortic pressure was very small in both cases (**Figure 4.4D**).

### **4.3.3 Effect of RVAD on septum curvature**

The septum has substantially lower curvature  $\kappa$  in the PAH cases compared to that in the normal case (**Figure 4.5A**). Septum curvature in the PAH patients was also lower compared to the LVFW curvature, which is opposite of what is found in the normal subject. The PAHR case with severely dilated RV had the lowest LVFW and septum curvatures. To eliminate the size effect, we also computed the normalized septum curvature by dividing the septum curvature with that average curvature over the entire LV (**Figure 4.5B**). We found that the PAH patients had lower normalized septum curvature over all cardiac time points. Implantation of the RVAD, on the other hand, increased the septum curvature for both PAH patients, particularly during the filling (diastolic) phase (**Figure 4.5B**). The overall increase in the septum curvature is evident in the mid-ventricular short-axis slices taken from the PAHR and PAHN cases (**Figure 4.5C**), revealing that the septum moved towards the RV when RVAD was operated at 28krpm.

### **4.3.4 Effect of RVAD on myofiber stress**

Average myofiber stresses in the LVFW, septum and RVFW were higher in both PAH cases compared to the normal (**Figure 4.6**). Peak fiber stresses (over a cardiac cycle) were highest in the PAHR case in all 3 regions (values given in the figure insets). Implantation of RVAD reduced only the myofiber stress at the RVFW in the PAHR case. At an RVAD speed of 28krpm, the peak myofiber stress was reduced by 12% in the RVFW (86.3 vs 98 kPa in the baseline). In the PAHN case, the average LVFW, septum and RVFW myofiber stresses all remained relatively unchanged with RVAD.

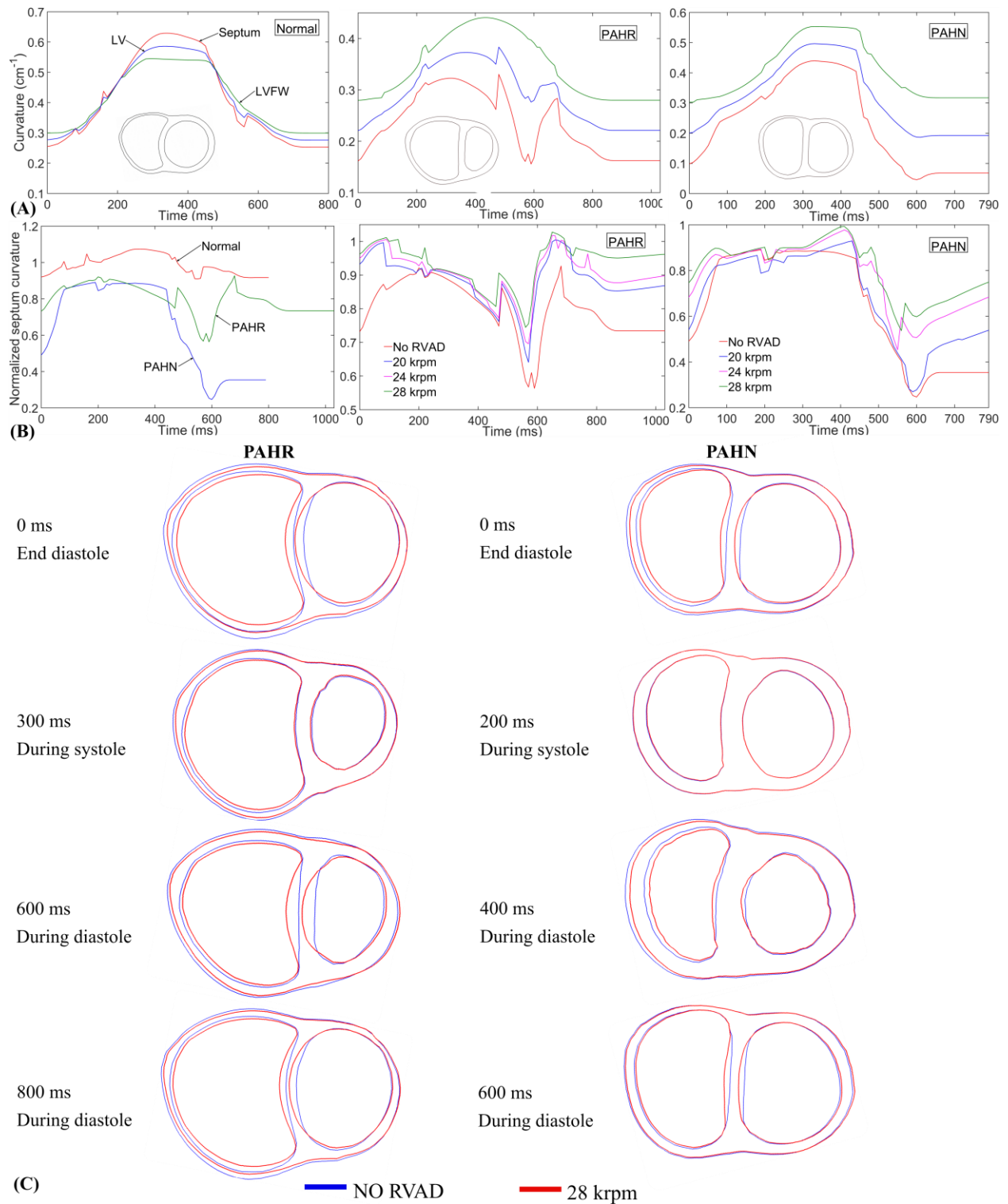


**Figure 4.5.** (A) LVFW, septum and LV curvature for normal, PAHR and PAHN cases, (B) comparison of the normalized septum curvature between normal, PAHR and PAHN cases (left), normalized septum curvature for PAHR (middle) and PAHN (right) cases with different RVAD speeds, (C) mid-ventricular short-axis slice of the PAHR (left) and PAHN (right) cases showing the motion of septal wall with RVAD over a cardiac cycle.

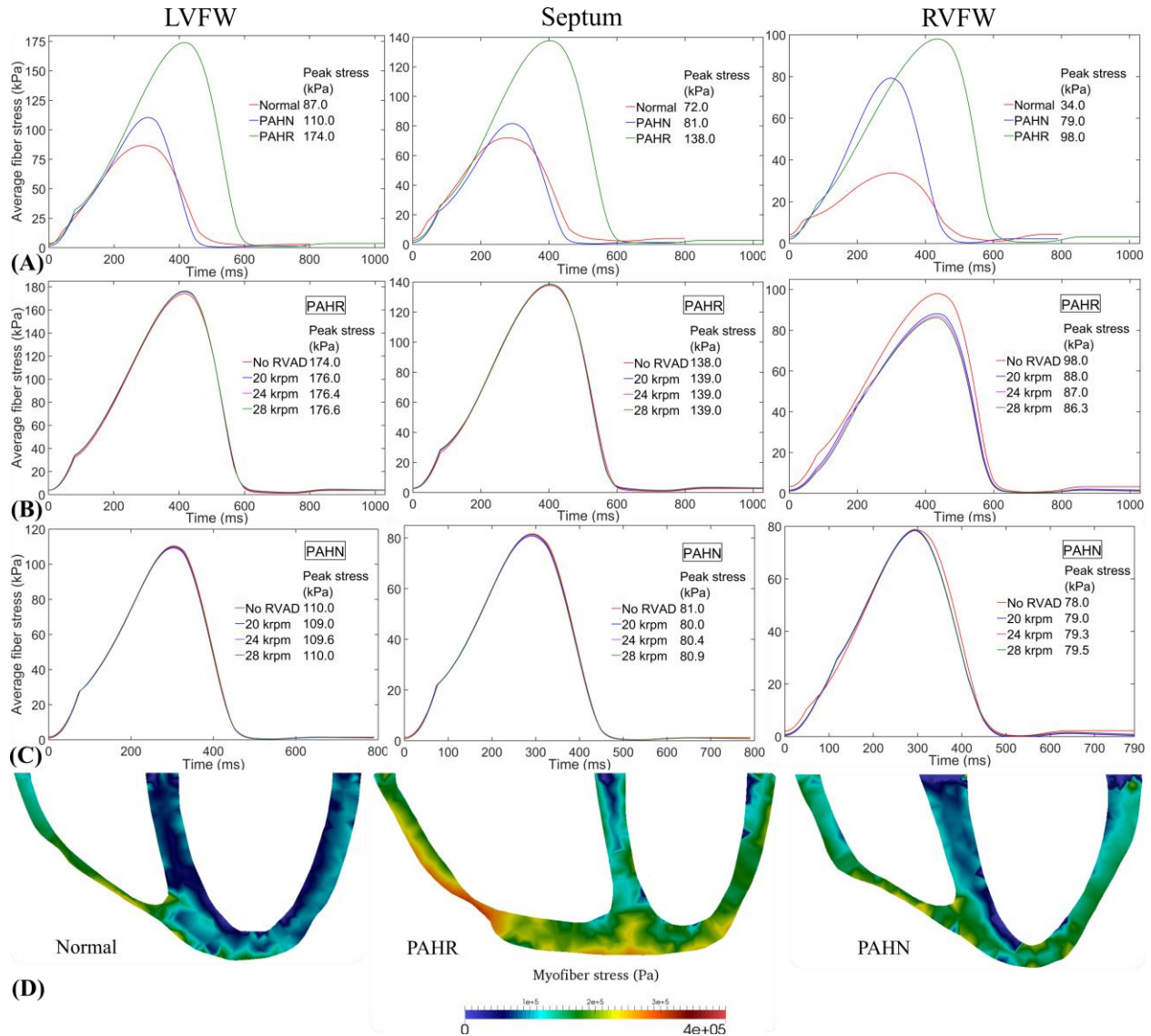


**Figure 4.6.** Average LVFW (left), Septum (middle) and RVFW (right) fiber stress (A) in the normal, PAHR and PAHN. (B) PAHR case with different RVAD speed. (C) PAHN case with different RVAD speed. (D) Myofiber stress shown by color map in long-axis slices at mid-ventricular level in Normal, PAHR and PAHN cases at end-systole.

#### 4.4 Discussion

We have developed a computational framework that couples an image-based biventricular FE model to a lumped parameter representation of the pulmonary and systemic circulations in a closed-loop system. Based on biventricular geometries that were reconstructed from the MR images of two PAH patients and a normal subject, the computational framework was calibrated

and matched well with the corresponding patient-specific measurements of 1) PV loops, 2) LV and RV volume waveforms and, 3) LV and RV pressure waveforms. The calibrated computational framework was used to simulate the effects of RVAD on the hemodynamics and ventricular mechanics of the two PAH patients, with different degree of RV remodeling. The major findings of this study suggest that 1) the effects of RVAD depend on the degree of RV remodeling in PAH and 2) the improvement in RV mechanics and septal curvature by RVAD are accompanied by alterations in arterial hemodynamics that may be detrimental.

The modeling results show that the spatially-averaged stresses in the LVFW, septum and RVFW are all increased in both PAH cases compared to normal subject, with the largest increase of ~190% found in the RVFW of the PAHR case (i.e., PAH patient with severe RV remodeling). Similar results showing that LVFW stress is increased in PAH are also found in a previous study<sup>174</sup>. Abnormalities in the septal wall motion was also found in the PAH cases, which are manifested as a bulging movement of the septum wall towards the LV (i.e., left ventricular septal bow) that is a well-known feature of this disease<sup>111</sup>. As a result, septum curvature computed at the mid-ventricular level are substantially lower in the PAH cases compared to the normal case, indicative that the septum in these cases are more “flattened”.

The effects of RVAD on the two PAH cases can be different or similar depending on the quantity of interest. In terms of similar features, the models show that RVAD 1) reduces both RV EDV and RV ESV, 2) improves CO, 3) decreases RA pressure and 4) increases the septum curvature during the filling phase of the cardiac cycle in both PAHN and PAHR cases, all with greater effects found in the latter case. In terms of difference, we found that RVAD produces 1) a slight increase in the RV peak pressure in the PAHN case but a small reduction in that in the PAHR case, and 2) only a reduction in the RVFW myofiber stress in the PAHR case by about 12% at an

operating speed of 28 krpm and no change in the myofiber stresses in the PAHN case at different operating speeds. We note that even with the 12% reduction in RVFW myofiber stress in the PAHR case after RVAD implantation, the resultant myofiber stress is still about 153% higher than that found in the normal case. Nevertheless, these findings suggest that RVAD may produce more benefits when implanted in PAH patients exhibiting severe RV remodeling.

The positive effects of RVAD as described above, however, are compromised by an increase in the mean and diastolic PA pressure as well as LV EDV, which are all present in the two PAH cases. The increase in PA pressure (mean and diastolic) is, however, more prominent in the PAHN case. Specifically, the increase in PA pressure can severely damage the pulmonary vasculature, which can produce pulmonary hemorrhage or pulmonary edema<sup>136</sup>. These findings are consistent with previous case reports<sup>55,130</sup> and a study based on lumped parameter circulatory model<sup>128</sup>, which all reported an increase in the mean and diastolic PA pressures with RVAD implantation in PAH patients.

Taken together, our finding that the effects of RVAD on hemodynamics and ventricular mechanics are not the same in PAH patients with different degree of remodeling suggests that the decision concerning the implantation of this device and its operation may need to be determined and optimized individually for each patient depending on disease progression. Moreover, the beneficial effects of RVAD (e.g., reduction of RV myofiber stress in PAH patients with severe RV remodeling) may also need to be balanced against its adverse effects on arterial hemodynamics. Indeed, while RVAD has been implanted in patients who have right heart failure caused by RV infarction or LV assist device (LVAD) implantation<sup>43,75,91,97,115</sup>, this device has not been used in PAH patients due to the high risk of pulmonary hemorrhage resulting from high RVAD flow. This is especially because the pump used in RVAD is generally designed to support the LV with higher

flow even though newer pump design with lower flow rate<sup>73</sup> and partial-assist pumps<sup>50</sup> have been recently proposed to assist the RV in providing sufficient flow for circulation without damaging the pulmonary vasculature.

As shown in this study, the image-based computational framework can help evaluate patient-specific effects of PAH and RVAD implantation not only on ventricular hemodynamics, deformation and myofiber stresses but also on arterial hemodynamics and wall stresses when coupled with a FE model of the vasculature as we have done previously<sup>143</sup>. Previous computational heart models<sup>13,51,174</sup> developed to investigate PAH in humans do not consider the bi-directional coupling between the heart and both the pulmonary and systemic circulation. On the other hand, a computational study that investigate the effects of RVAD in PAH patients<sup>128</sup> is based entirely on a lumped parameter modeling framework, which cannot be used to evaluate regional ventricular stresses and deformation (e.g., septal curvature). The image-based computational framework presented here, which couples patient-specific biventricular FE model with a closed-loop pulmonary and systemic circulatory model, overcomes all these limitations and enables us to assess the effects of remodeling in PAH and different RVAD operating speed on regional myofiber stresses, biventricular deformation and hemodynamics. The computational framework can be extended in future to include a FE model of the pulmonary vasculature to develop more insights in PAH, particularly, in understanding the complex ventricular interdependence and ventricular-vascular coupling associated with this disease.

#### **4.4.1 Limitations**

There are some limitations associated with this study. First, the zero-stress unloaded biventricular geometry was reconstructed from the MR images corresponding to the lowest pressure in diastole. While previous studies have either assumed the unloaded geometry to correspond to that obtained

at end systole<sup>167</sup> or mid systole<sup>79</sup>, or have computed it from the end diastolic geometry using unloading algorithms based on some prescribed material properties<sup>5,40</sup>, there are, unfortunately, no general consensus in the literature on what is the best approach to approximate the unloaded geometry. Second, we have used a “rule-based” method to prescribe the local myofiber direction, which varies transmurally from  $60^\circ$  at the endocardium to  $-60^\circ$  at the epicardium in the biventricular FE for both the normal subject as well as the PAH patients. Thus, we did not take into account possible changes in the myofiber direction during RV remodeling<sup>64</sup> that may occur in humans. Nevertheless, as we have focused on comparing the effects of RVAD on the overall heart function in PAH patients, we do not expect these limitations and assumptions to highly impact the findings of our study.

## CHAPTER 5

### Multi-organ finite element model for simulating ventricular-vascular interaction

#### 5.1 Introduction

It is well known that ventricular-arterial interaction plays a very important role in the normal functioning of the cardiovascular system. In-depth study of this interaction, however, has been limited due to the absence of detailed computational modeling framework that can physiologically couple these two organs. Finite element models of the LV have been widely used in the literature for years to study its mechanics as well as organ-scale physiological behaviors in the cardiac cycle<sup>83,101,144,164,174</sup>. In these models, the aorta is usually represented within the lumped parameter circulatory model by its electrical analog, which cannot separate the effects its geometry, microstructure, and constituents' mechanical behavior have on the LV's operating behavior *in vivo* and vice versa.

To overcome these limitations, we describe here a novel computational framework that is capable of coupling high spatial resolution FE models of both the vasculature and the heart to describe bidirectional ventricular-arterial coupling in the systemic circulation. Using realistic geometries and microstructure of the LV and aorta, we show that the framework is able to reproduce features that are consistent with measurements made in both compartments. We also performed a parameter study to show how mechanical and geometrical changes in the aorta affect the heart function and vice versa.

Later, the modeling framework is extended to include the pulmonary circulation. The image based biventricular model is developed by using high resolution FE models of aorta, pulmonary artery and heart which are coupled to lumped parameter circulatory model in both pulmonary and systemic circulation. The part of the study is published in *frontiers in physiology*<sup>143</sup>.

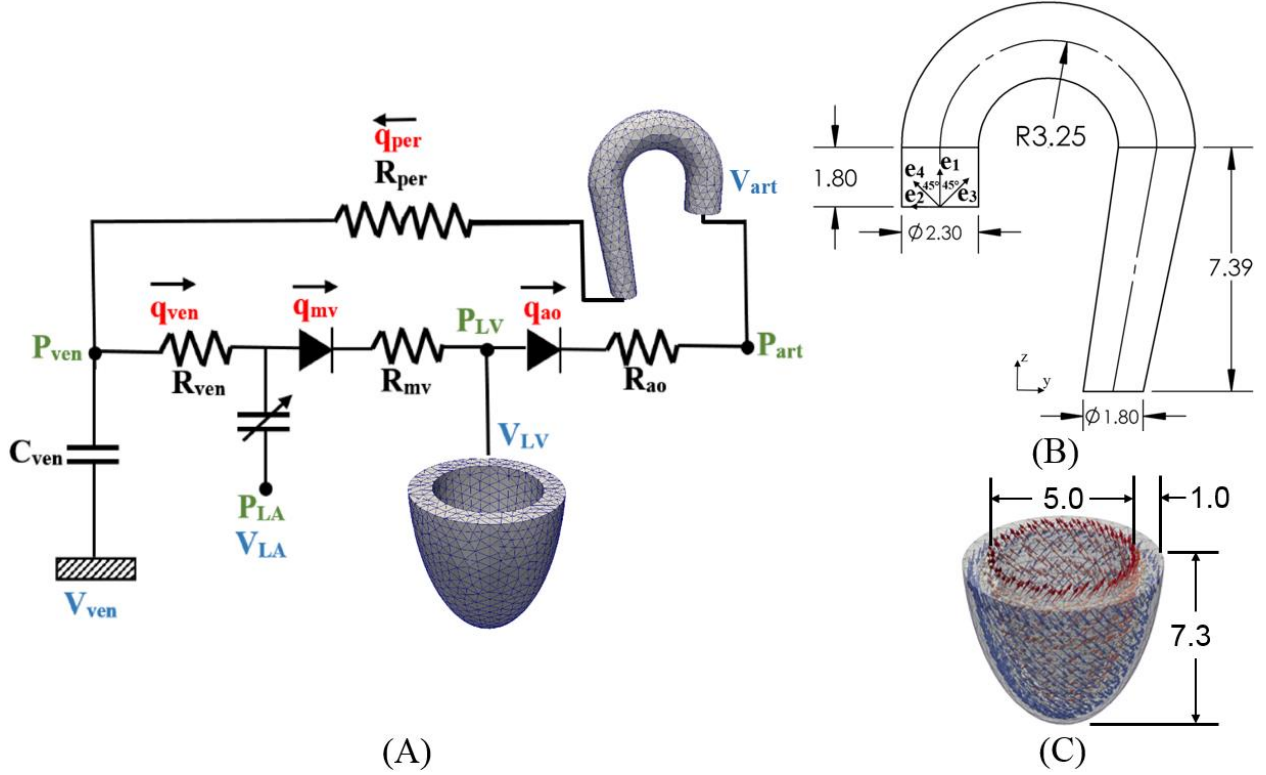


**Figure 5.1.** (A) Schematic diagram of the ventricular-arterial modeling framework, (B) unloaded aorta geometry with  $e_k$  ( $k = 1 - 4$ ) showing the directions of the four collagen fiber families, (C) unloaded LV geometry with fiber directions varying from  $60^\circ$  at the endocardium to  $-60^\circ$  at the epicardium wall (all dimensions are in cm).

## 5.2 Methods

### 5.2.1 Closed-loop systemic circulatory model

Finite element models of the aorta and LV were coupled via a closed-loop modeling framework describing the systemic circulatory system. Other components of the circulatory system were modeled using electrical analogs (**Figure 5.1A**). Mass of blood was conserved by the following equations relating the rate of volume change in each storage compartment of the circulatory system to the inflow and outflow rates

$$\frac{dV_{LA}(t)}{dt} = q_{ven}(t) - q_{mv}(t); \quad (5.1a)$$

$$\frac{dV_{LV}(t)}{dt} = q_{mv}(t) - q_{ao}(t); \quad (5.1b)$$

$$\frac{dV_{art}(t)}{dt} = q_{ao}(t) - q_{per}(t); \quad (5.1c)$$

$$\frac{dV_{ven}(t)}{dt} = q_{per}(t) - q_{ven}(t), \quad (5.1d)$$

where  $V_{LA}$ ,  $V_{LV}$ ,  $V_{art}$ , and  $V_{ven}$  are volumes of each compartment, and  $q_{ven}$ ,  $q_{mv}$ ,  $q_{ao}$ , and  $q_{per}$  are flow rates at different segments (**Figure 5.1A**). Flowrate at different segments of the circulatory model depends on their resistance to flow ( $R_{ao}$ ,  $R_{per}$ ,  $R_{ven}$ , and  $R_{mv}$ ) and the pressure difference between the connecting storage compartments (i.e., pressure gradient). The flow rates are given by

$$q_{ao}(t) = \begin{cases} \frac{P_{LV,cav}(t) - P_{art,cav}(t)}{R_{ao}} & \text{when, } P_{LV,cav}(t) \geq P_{art,cav}(t) \\ 0 & \text{when, } P_{LV,cav}(t) < P_{art,cav}(t) \end{cases}; \quad (5.2a)$$

$$q_{per}(t) = \frac{P_{art,cav}(t) - P_{ven}(t)}{R_{per}}; \quad (5.2b)$$

$$q_{ven}(t) = \frac{P_{ven}(t) - P_{LA}(t)}{R_{ven}}; \quad (5.2c)$$

$$q_{mv}(t) = \begin{cases} \frac{P_{LA}(t) - P_{LV,cav}(t)}{R_{mv}} & \text{when, } P_{LA}(t) \geq P_{LV,cav}(t) \\ 0 & \text{when, } P_{LA}(t) < P_{LV,cav}(t) \end{cases}. \quad (5.2d)$$

Pressure in each storage compartment is a function of its volume. A simplified pressure volume relationship,

$$P_{ven}(t) = \frac{V_{ven}(t) - V_{ven,0}}{C_{ven}}, \quad (5.3)$$

was prescribed for the veins, where  $V_{ven,0}$  is a constant resting volume of the veins and  $C_{ven}$  is the total compliance of the venous system. On the other hand, pressure in the left atrium  $P_{LA}(t)$  was

prescribed to be a function of its volume  $V_{LA}(t)$  by the following equations that describe its contraction using a time-varying elastance function  $e(t)$ :

$$P_{LA}(t) = e(t)P_{es,LA}(V_{LA}(t)) + (1 - e(t))P_{ed,LA}(V_{LA}(t)) \quad , \quad (5.4)$$

where

$$P_{es,LA}(V_{LA}(t)) = E_{es,LA}(V_{LA}(t) - V_{0,LA}) \quad , \quad (5.5a)$$

$$P_{ed,LA}(V_{LA}(t)) = A_{LA} (e^{B_{LA}(V_{LA}(t) - V_{0,LA})} - 1) \quad , \quad (5.5b)$$

and,

$$e(t) = \begin{cases} \frac{1}{2} \left( \sin \left[ \left( \frac{\pi}{t_{max}} \right) t - \frac{\pi}{2} \right] + 1 \right); & 0 < t \leq 3/2 t_{max} \\ \frac{1}{2} e^{-(t - 3/2 t_{max})/\tau}; & t > 3/2 t_{max} \end{cases} \quad . \quad (5.5c)$$

In Eqs. (5.5a-b),  $E_{es,LA}$  is the end-systolic elastance of the left atrium,  $V_{0,LA}$  is the volume axis intercept of the end-systolic pressure volume relationship (ESPVR), and both  $A_{LA}$  and  $B_{LA}$  are parameters of the end-diastolic pressure volume relationship (EDPVR) of the left atrium. The driving function  $e(t)$  is given in Eq. (5c) in which  $t_{max}$  is the point of maximal chamber elastance and  $\tau$  is the time constant of relaxation. The values of  $E_{es,LA}$ ,  $V_{0,LA}$ ,  $A_{LA}$ ,  $B_{LA}$ ,  $t_{max}$  and  $\tau$  are listed in **Table 5.1**.

Finally, pressure in the other two storage compartments, namely, LV and aorta, depends on their corresponding volume through non-closed form functions

$$P_{LV,cav}(t) = f^{LV}(V_{LV}(t)) \quad , \quad (5.6)$$

$$P_{art,cav}(t) = f^{art}(V_{art}(t)) \quad . \quad (5.7)$$

**Table 5.1.** Parameters of time varying elastance model for the left atrium

Parameter	Unit	Values
End-systolic elastance, $E_{es,LA}$	Pa/ml	60
Volume axis intercept, $V_{0,LA}$	ml	10
Scaling factor for EDPVR, $A_{LA}$	Pa	58.67
Exponent for EDPVR, $B_{LA}$	ml <sup>-1</sup>	0.049
Time to end-systole, $t_{max}$	msec	200
Time constant of relaxation, $\tau$	msec	35

**Table 5.2.** Parameters of the closed loop lumped parameter circulatory framework

Parameter	Unit	Values
Aortic valve resistance, $R_{ao}$	Pa ms ml <sup>-1</sup>	2000
Peripheral resistance, $R_{per}$	Pa ms ml <sup>-1</sup>	125000
Venous resistance, $R_{ven}$	Pa ms ml <sup>-1</sup>	2000
Mitral valve resistance, $R_{mv}$	Pa ms ml <sup>-1</sup>	2000
Venous compliance, $C_{ven}$	ml Pa	0.3
Resting volume for vein, $V_{ven,0}$	ml	3200

The functional relationship between pressure and volume in the LV and aorta were obtained using the FE method as described in the next section. An explicit time integration scheme was used to solve Eq. (5.1). Steady-state pressure-volume loop was established by running the simulation over several cardiac cycles, each with a cycle time of 800ms (equivalent to 75 bpm). All the parameter values used in the circulatory model are listed in **Table 5.2**.

### 5.2.2 Finite element formulation of the left ventricle and aorta

Finite element formulation of the other two storage compartments can be generalized from the minimization of the following Lagrangian functional with the subscript  $k = LV$  denoting the LV and  $k = art$  denoting the aorta

$$\begin{aligned} \mathcal{L}_k(\mathbf{u}_k, p_k, P_{k,\text{cav}}, \mathbf{c}_{1,k}, \mathbf{c}_{2,k}) = & \int_{\Omega_{0,k}} W_k(\mathbf{u}_k) dV - \int_{\Omega_{0,k}} p_k (J_k - 1) dV - P_{k,\text{cav}} (V_{k,\text{cav}}(\mathbf{u}_k) - \\ & V_k) - \mathbf{c}_{1,k} \cdot \int_{\Omega_{0,k}} \mathbf{u}_k dV - \mathbf{c}_{2,k} \cdot \int_{\Omega_{0,k}} \mathbf{X}_k \times \mathbf{u}_k dV. \end{aligned} \quad (5.8)$$

In the above equation,  $\mathbf{u}_k$  is the displacement field,  $P_{k,\text{cav}}$  is the Lagrange multiplier to constrain the cavity volume  $V_{k,\text{cav}}(\mathbf{u}_k)$  to a prescribed value  $V_k$ <sup>124</sup>,  $p_k$  is a Lagrange multiplier to enforce incompressibility of the tissue (i.e., Jacobian of the deformation gradient tensor  $J_k = 1$ ), and both  $\mathbf{c}_{1,k}$  and  $\mathbf{c}_{2,k}$  are Lagrange multipliers to constrain rigid body translation (i.e., zero mean translation) and rotation (i.e., zero mean rotation)<sup>125</sup>. The functional relationship between the cavity volumes of the LV and aorta to their respective displacement fields is given by

$$V_{k,\text{cav}}(\mathbf{u}_k) = \int_{\Omega_{\text{inner}}} dv = -\frac{1}{3} \int_{\Gamma_{\text{inner}}} \mathbf{x}_k \cdot \mathbf{n}_k da, \quad (5.9)$$

where  $\Omega_{\text{inner}}$  is the volume enclosed by the inner surface  $\Gamma_{\text{inner}}$  and the basal surface at  $z = 0$ , and  $\mathbf{n}_k$  is the outward unit normal vector.

Pressure-volume relationships of the LV and aorta required in the lumped parameter circulatory model (i.e., Eqs. (5.6) and (5.7)) were defined by the solution obtained from minimizing the functional. Taking the first variation of the functional in Eq. (5.8) leads to the following expression:

$$\begin{aligned} \delta \mathcal{L}_k(\mathbf{u}_k, p_k, P_{k,\text{cav}}, \mathbf{c}_{1,k}, \mathbf{c}_{2,k}) = & \int_{\Omega_{0,k}} (\mathbf{P}_k - p_k \mathbf{F}_k^{-T}) : \nabla \delta \mathbf{u}_k dV - \int_{\Omega_{0,k}} \delta p_k (J_k - 1) dV - \\ & P_{k,\text{cav}} \int_{\Omega_{0,k}} \text{cof}(\mathbf{F}_k) : \nabla \delta \mathbf{u}_k dV - \delta P_{k,\text{cav}} (V_{k,\text{cav}}(\mathbf{u}_k) - V_k) - \delta \mathbf{c}_{1,k} \cdot \int_{\Omega_{0,k}} \mathbf{u}_k dV - \delta \mathbf{c}_{2,k} \cdot \\ & \int_{\Omega_{0,k}} \mathbf{X}_k \times \mathbf{u}_k dV - \mathbf{c}_{1,k} \cdot \int_{\Omega_{0,k}} \delta \mathbf{u}_k dV - \mathbf{c}_{2,k} \cdot \int_{\Omega_{0,k}} \mathbf{X}_k \times \delta \mathbf{u}_k dV. \end{aligned} \quad (5.10)$$

In Eq. (5.10),  $\mathbf{P}_k$  is the first Piola Kirchhoff stress tensor,  $\mathbf{F}_k$  is the deformation gradient tensor,  $\delta \mathbf{u}_k$ ,  $\delta p_k$ ,  $\delta P_{k,\text{cav}}$ ,  $\delta \mathbf{c}_{1,k}$ ,  $\delta \mathbf{c}_{2,k}$  are the variation of the displacement field, Lagrange multipliers for enforcing incompressibility and volume constraint, zero mean translation and

rotation, respectively. The Euler-Lagrange problem then becomes finding  $\mathbf{u}_k \in H^1(\Omega_{0,k})$ ,  $p_k \in L^2(\Omega_{0,k})$ ,  $P_{k,cav} \in \mathbb{R}$ ,  $\mathbf{c}_{1,k} \in \mathbb{R}^3$ ,  $\mathbf{c}_{2,k} \in \mathbb{R}^3$  that satisfies

$$\delta \mathcal{L}_k(\mathbf{u}_k, p_k, P_{k,cav}, \mathbf{c}_{1,k}, \mathbf{c}_{2,k}) = 0 \quad (5.11)$$

and  $\mathbf{u}_k(x, y, 0) \cdot \mathbf{n}|_{k,base} = 0$  (for constraining the basal deformation to be in-plane)  $\forall \delta \mathbf{u}_k \in H^1(\Omega_{0,k})$ ,  $\delta p_k \in L^2(\Omega_{0,k})$ ,  $\delta P_{k,cav} \in \mathbb{R}$ ,  $\delta \mathbf{c}_{1,k} \in \mathbb{R}^3$ ,  $\delta \mathbf{c}_{2,k} \in \mathbb{R}^3$ .

An explicit time integration scheme was used to solve the ODEs in Eq. (5.1). Specifically, compartment volumes ( $V_{LA}, V_{LV}, V_{art}, V_{ven}$ ) at each timestep  $t_i$  was determined from their respective values and the segmental flow rates ( $q_{ven}, q_{mv}, q_{ao}, q_{per}$ ) at previous timestep  $t_{i-1}$  in Eq. (5.1). The computed compartment volumes at  $t_i$  were used to update the corresponding pressures ( $P_{LA}, P_{LV}, P_{art}, P_{ven}$ ). Pressures in the left atrium ( $P_{LA}$ ) and veins ( $P_{ven}$ ) were computed from Eq. (4.4) and (4.3), respectively. On the other hand, pressures in the LV ( $P_{LV,cav}$ ) and aorta ( $P_{art,cav}$ ) were computed from the FE solutions of Eq. (4.11) (for  $k = LV$  and  $art$ ) with the volumes ( $V_{LV}, V_{art}$ ) at timestep  $t_i$  as input. We note here that ( $P_{LV,cav}, P_{art,cav}$ ) are scalar Lagrange multipliers in the FE formulation for constraining the cavity volumes to the prescribed values ( $V_{LV}, V_{art}$ ). The computed pressures at timestep  $t_i$  were then used to update the segmental flow rates in Eq. (5.2) that will be used to compute the compartment volumes at timestep  $t_{i+1}$  in the next iteration.

### 5.2.3 Geometry and microstructure of the LV

The LV geometry was described using a half prolate ellipsoid that was discretized with 1325 quadratic tetrahedral elements. The helix angle associated with the myofiber direction  $\mathbf{e}_{f_0}$  was

varied with a linear transmural variation from  $60^\circ$  at the endocardium to  $-60^\circ$  at the epicardium in the LV wall based on previous experimental measurements<sup>153</sup> (**Figure 5.1C**).

#### 5.2.4 Constitutive law of the LV

An active stress formulation was used to describe the LV's mechanical behavior in the cardiac cycle. In this formulation, the stress tensor  $\mathbf{P}_{LV}$  can be decomposed additively into a passive component  $\mathbf{P}_{LV,p}$  and an active component  $\mathbf{P}_{LV,a}$  (i.e.,  $\mathbf{P}_{LV} = \mathbf{P}_{LV,a} + \mathbf{P}_{LV,p}$ ). The passive stress tensor was defined by  $\mathbf{P}_{LV,p} = dW_{LV}/d\mathbf{F}_{LV}$ , where  $W_{LV}$  is a strain energy function of a Fung-type transversely-isotropic hyperelastic material<sup>57</sup> given by

$$W_{LV} = \frac{1}{2}C(e^Q - 1), \quad (5.12a)$$

where,

$$Q = b_{ff}E_{ff}^2 + b_{xx}(E_{ss}^2 + E_{nn}^2 + E_{sn}^2 + E_{ns}^2) + b_{fx}(E_{fn}^2 + E_{nf}^2 + E_{fs}^2 + E_{sf}^2). \quad (5.12b)$$

In Eq. (5.12),  $E_{ij}$  with  $(i, j) \in (f, s, n)$  are components of the Green-Lagrange strain tensor  $\mathbf{E}_{LV}$  with  $f, s, n$  denoting the myocardial fiber, sheet and sheet normal directions, respectively. Material parameters of the passive constitutive model are denoted by  $C$ ,  $b_{ff}$ ,  $b_{xx}$  and  $b_{fx}$ .

The active stress  $\mathbf{P}_{LV,a}$  was calculated along the local fiber direction using a previously developed active contraction model<sup>38,58</sup>,

$$\mathbf{P}_{LV,a} = T_{max} \frac{ca_0^2}{ca_0^2 + Eca_{50}^2} C_t \mathbf{e}_f \otimes \mathbf{e}_{f_0} \quad (5.13)$$

In the above equation,  $\mathbf{e}_f$  and  $\mathbf{e}_{f_0}$  are, respectively, the local vectors defining the muscle fiber direction in the current and reference configurations,  $T_{max}$  is the isometric tension achieved at the

longest sarcomere length and  $Ca_0$  denotes the peak intracellular calcium concentration. The length dependent calcium sensitivity  $E Ca_{50}$  and the variable  $C_t$  are given by

$$E Ca_{50} = \frac{(Ca_0)_{max}}{\sqrt{\exp(B(l-l_0))-1}} \quad , \quad (5.14a)$$

$$C_t = \frac{1}{2}(1 - \cos\omega). \quad (5.14b)$$

In Eq. (5.14a),  $B$  is a constant,  $(Ca_0)_{max}$  is the maximum peak intracellular calcium concentration and  $l_0$  is the sarcomere length at which no active tension develops. The variable  $\omega$  in Eq. (5.14b) is given by

$$\omega = \begin{cases} \pi \frac{t}{t_0}, & 0 \leq t < t_0; \\ \pi \frac{t-t_0+t_r}{t_r}, & t_0 \leq t < t_0 + t_r; \\ 0, & t_0 + t_r \leq t. \end{cases} \quad (5.15)$$

In the above equation,  $t_0$  is the time taken to reach peak tension and  $t_r$  is the duration of relaxation that depends linearly on the sarcomere length  $l$  by

$$t_r = ml + b, \quad (5.16)$$

where  $m$  and  $b$  are constants. The sarcomere length  $l$  can be calculated from the myofiber stretch  $\lambda_{LV}$  by

$$\lambda_{LV} = \sqrt{\mathbf{e}_{f_0} \cdot \mathbf{C}_{LV} \mathbf{e}_{f_0}}, \quad (5.17a)$$

$$l = \lambda_{LV} l_r. \quad (5.17b)$$

In Eq. (5.17a),  $\mathbf{C}_{LV} = \mathbf{F}_{LV}^T \mathbf{F}_{LV}$  is the right Cauchy-Green deformation tensor and  $l_r$  is the relaxed sarcomere length. Parameter values associated with the LV model are tabulated in **Table 5.3**.

**Table 5.3.** Parameters of the LV model.

Parameter	Description	Value
$C$	material parameter	100.0
$b_{ff}$	material parameter	29.9
$b_{xx}$	material parameter	13.3
$b_{fx}$	material parameter	26.6
$T_{max}$	isometric tension under maximal activation, kPa	200.7
$Ca_0$	peak intracellular calcium concentration, $\mu\text{M}$	4.35
$(Ca_0)_{max}$	maximum peak intracellular calcium concentration, $\mu\text{M}$	4.35
$B$	governs shape of peak isometric tension-sarcomere length relation, $\mu\text{m}^{-1}$	4.75
$l_0$	sarcomere length at which no active tension develops, $\mu\text{m}$	1.58
$t_0$	time to peak tension, msec	171
$m$	slope of linear relaxation duration-sarcomere length relation, msec $\mu\text{m}^{-1}$	1049
$b$	time-intercept of linear relaxation duration-sarcomere length relation, msec	1500
$l_r$	relaxed sarcomere length, $\mu\text{m}$	1.85

### 5.2.5 Geometry and microstructure of the aorta

An idealized geometry of the aorta extending from the heart to the thoracic region from a previous study<sup>165</sup> was used here. The geometry was discretized using 1020 quadratic tetrahedral elements. The aorta diameter was assumed to be constant in the first segment starting from the aortic root to the middle of the aortic arch, and then gradually decreased towards the thoracic region. Aortic wall thickness was kept constant (**Figure 5.1B**).

### 5.2.6 Constitutive law of the aorta

Stress tensor in the aortic wall was defined by  $\mathbf{P}_{art} = dW_{art}/d\mathbf{F}_{art}$ , where  $W_{art}$  is the sum of the strain energy functions associated with those from the key tissue constituents, namely, elastin-

dominated matrix  $W_e$ , collagen fiber families  $W_{c,k}$  and vascular smooth muscle cells (SMC)  $W_m$ <sup>15,177</sup>, i.e.,

$$W_{\text{art}} = W_e + \sum_{k=1}^4 W_{c,k} + W_m. \quad (5.18)$$

Strain energy function of the elastin-dominated amorphous matrix is given by

$$W_e = M_e \left( \frac{c_1}{2} \right) (\text{tr}(\mathbf{C}_{\text{art}}) - 3), \quad (5.19)$$

where  $M_e$  is the mass per unit volume of the elastin in the tissue,  $c_1$  is a material parameter and,  $\mathbf{C}_{\text{art}} = \mathbf{F}_{\text{art}}^T \mathbf{F}_{\text{art}}$  is the right Cauchy-Green deformation tensor associated with the aorta.

Four collagen fiber families were considered here. The first and second families of collagen fibers ( $k = 1$  and  $2$ ) were oriented in the longitudinal and circumferential directions, whereas the third and fourth families of collagen fibers ( $k = 3$  and  $4$ ) were oriented, respectively, at an angle  $\alpha = 45^\circ$  and  $-45^\circ$  with respect to the longitudinal axis (**Figure 5.1B**). We assumed the same strain energy function for all the families of collagen fibers that is given by

$$W_{c,k} = M_k \frac{c_2}{4c_3} \left\{ \exp \left[ c_3 (\lambda_k^2 - 1)^2 \right] - 1 \right\}. \quad (5.20)$$

In Eq. (5.20),  $M_k$  is the mass per unit volume of  $k^{\text{th}}$  family of collagen fibers,  $\lambda_k$  is the corresponding stretch of those fibers, and both  $c_2$  and  $c_3$  are the material parameters. The stretch in the  $k^{\text{th}}$  family of collagen fibers was defined by  $\lambda_k = \sqrt{\mathbf{e}_{k0} \cdot \mathbf{C}_{\text{art}} \mathbf{e}_{k0}}$ , where  $\mathbf{e}_{k0}$  is the local unit vector defining the corresponding fibers orientation.

Strain energy function of the smooth muscle cells  $W_m$  was additively decomposed into one describing its passive mechanical behavior  $W_{m,p}$  and one describing its active behavior  $W_{m,a}$  (i.e.,  $W_m = W_{m,p} + W_{m,a}$ ). The passive strain energy function is given by

$$W_{m,p} = M_m \frac{c_4}{4c_5} \left\{ \exp \left[ c_5 (\lambda_m^2 - 1)^2 \right] - 1 \right\}. \quad (5.21)$$

Here,  $M_m$  is the mass per unit volume of the smooth muscle in the tissue,  $\lambda_m$  is the stretch of the smooth muscle, whereas  $c_4$  and  $c_5$  are the material parameters. The smooth muscle cells were assumed to be perfectly aligned in the circumferential direction. Its stretch is therefore equivalent to that of the second family of collagen fibers i.e.,  $\lambda_m = \lambda_2$ . We used the following strain energy function<sup>177</sup> to describe the active tone of vascular smooth muscle,

$$W_{m,a} = M_m \frac{S_m}{\rho} \left[ \lambda_m + \frac{(\lambda_M - \lambda_m)^3}{3(\lambda_M - \lambda_0)^2} \right]. \quad (5.22)$$

In Eq. (5.22),  $S_m$  is the stress at maximum contraction,  $\rho$  is the density of the tissue,  $\lambda_M$  is the prescribed stretch at which the contraction is maximum and  $\lambda_0$  is the prescribed stretch at which active force generation ceases. Mass per unit volume for the different constituents were calculated using following relations

$$M_e = \phi_e \rho, \quad (5.23a)$$

$$M_m = \phi_m \rho, \quad (5.23b)$$

$$M_k = \phi_k (1 - \phi_e - \phi_m) \rho, \quad (5.23c)$$

where  $\phi_e, \phi_m, \phi_k$  denotes the mass fraction for elastin, smooth muscle cells and  $k^{\text{th}}$  family of collagen fibers. It was assumed that 20% of the total collagen mass was distributed equally towards the longitudinal and circumferential fiber families and the remaining 80% was distributed equally to  $\alpha = 45^\circ$  and  $-45^\circ$  fiber directions. Constitutive parameters, mass fraction of each constituents and other parameters of the aorta model are listed in **Table 5.4**. The coupled LV-aorta modeling framework, including solving the FE equations associated with the LV and aorta models, was implemented using the open-source FE library FEnICS<sup>6</sup>.

**Table 5.4.** Parameters of the aorta model

Elastin	$c_1 = 160 \text{ kPa} , \phi_e = 0.306$
Collagen families	$c_2 = 0.08 \text{ kPa} , c_3 = 2.54, \phi_c = 0.544 (\phi_1 = 0.1\phi_c , \phi_2 = 0.1\phi_c, \phi_3 = 0.4\phi_c, \phi_4 = 0.4\phi_c)$
SMC	$c_4 = 0.01 \text{ kPa} , c_5 = 7.28, \phi_m = 0.15$
Others	$\rho = 1050 \text{ kg/m}^3, S_m = 54 \text{ kPa}, \lambda_M = 1.4, \lambda_0 = 0.8$

**Table 5.5.** Mass fractions of the aorta constituents for different cases investigated in the study. (For collagen fibers, the distribution of mass in four collagen fiber families was kept the same, i.e.,  $\phi_1 = 0.1\phi_c , \phi_2 = 0.1\phi_c, \phi_3 = 0.4\phi_c, \phi_4 = 0.4\phi_c$  for all cases).

Case	Mass fractions of the constituents	Comment
Baseline	Same as Table 5.4	No change
Without active	Same as Table 5.4	No active tone in SM, $S_m = 0$
M <sub>1</sub>	$\phi_e = 0.122, \phi_m = 0.061, \phi_c = 0.816$	Collagen increased by 50%, Elastin and SMC decreased proportionally
M <sub>2</sub>	$\phi_e = 0.49, \phi_m = 0.24, \phi_c = 0.272$	Collagen decreased by 50%, Elastin and SMC increased proportionally

### 5.3 Results

A baseline case was established using the LV-aorta coupling framework so that LV pressure-volume loop and aorta pressure-diameter curve were consistent with measurements in the normal human systemic circulation under physiological conditions. Specifically, model prediction of the LV ejection fraction (EF) was 56%, which is within the normal range in humans (**Figure 5.2B**). Similarly, end-diastolic (ED) and end-systolic (ES) diameters of the aorta in the baseline case (**Figure 5.2C**) were comparable to in-vivo measurements<sup>54,119</sup>. We note here that diameter of the aorta mentioned in subsequent text refers to its inner diameter. Pressure waveforms of the LV, aorta, and LA (**Figure 5.3**) in the baseline case were also within the normal range with an aortic pulse pressure of 50 mmHg (systolic: 128 mmHg, diastolic: 78 mmHg).

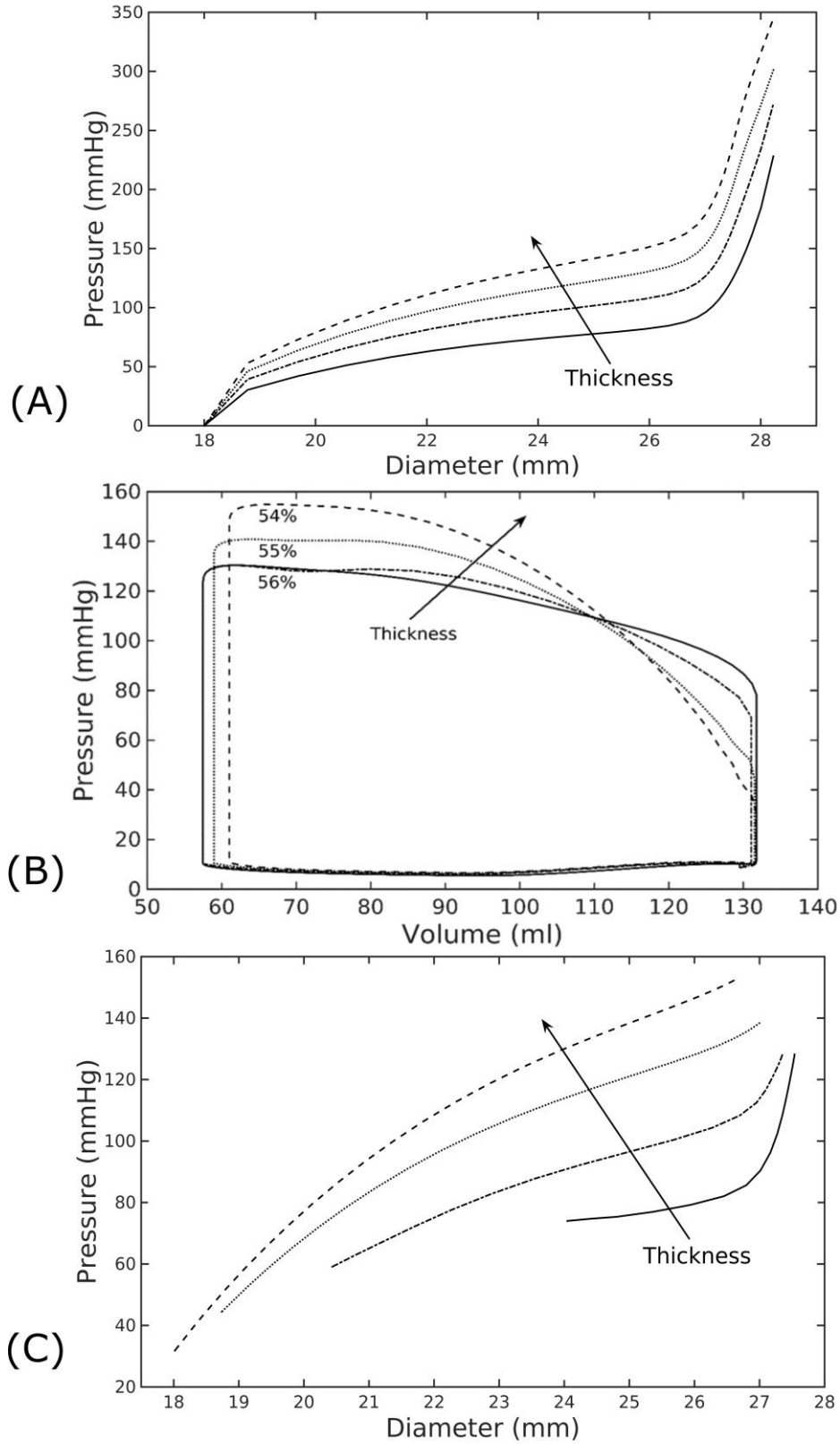


**Figure 5.2.** Effects of a change in aorta wall thickness on (A) its *ex-vivo* pressure-diameter relationship, (B) LV pressure-volume loop and (C) pressure - diameter both operating *in-vivo*.

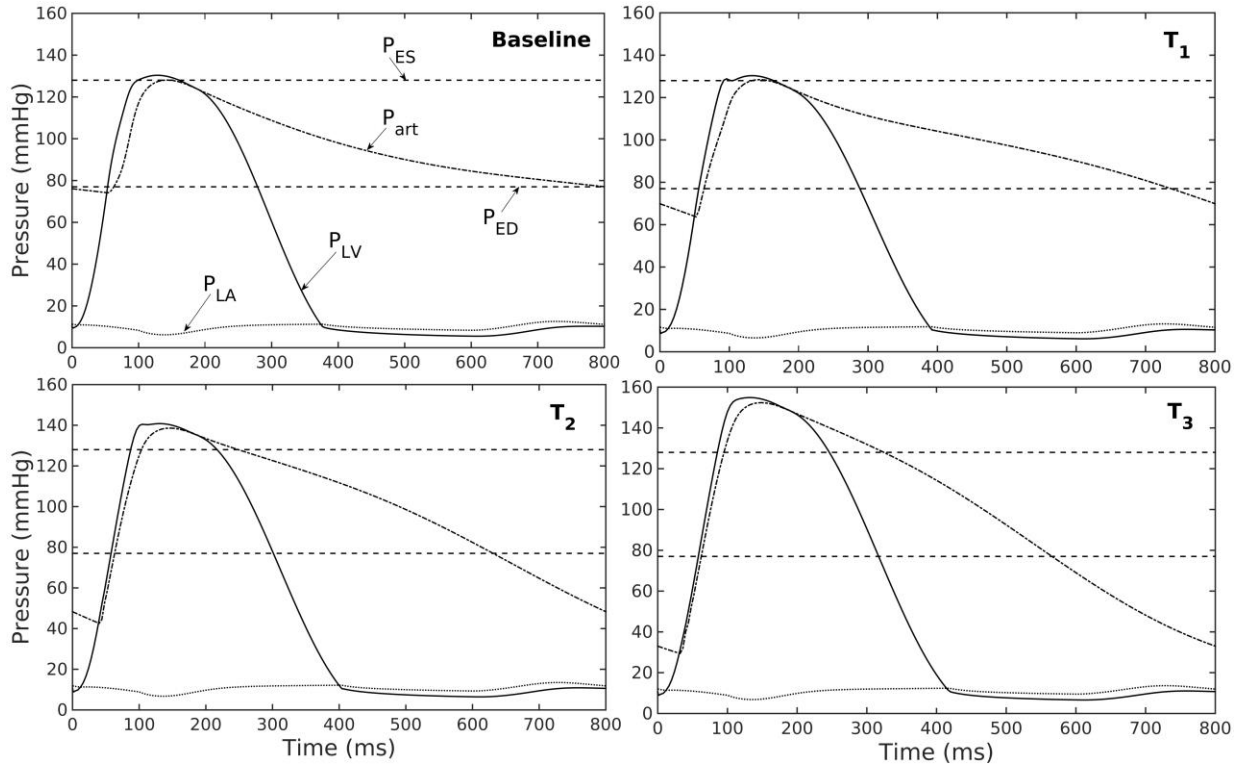


**Figure 5.3.** Pressure in LV, aorta and LA during cardiac cycle with increasing aorta wall thickness in ascending order from the Baseline to  $T_3$  case.

### 5.3.1 Effects of a change in aorta wall thickness

Varying the wall thickness in the aorta model led to changes in not only the aorta mechanical behavior but also the LV function (**Figure 5.2**). The aorta became stiffer (less compliant) with increasing wall thickness as reflected by an increase in the slope of the pressure-diameter curves (**Figure 5.2A**). When operating *in vivo* as simulated in the LV-aorta coupling framework, increasing the aorta wall thickness led to a lower LV EF, a higher peak systolic pressure of the LV (**Figure 5.2B**) and a leftward shift in the aorta pressure - diameter relationship with smaller diameter at ED and ES (**Figure 5.2C**). An increase in aorta ED wall thickness from 1.8 mm (baseline) to 5.4 mm ( $T_3$  case) was accompanied by an increase in pulse pressure from 50 mmHg (in the baseline case) to 120 mmHg. In comparison, the mean aortic pressure changed by only about 10 mmHg (decreased from 102 mmHg to 93 mmHg) for the same increase in wall thickness.

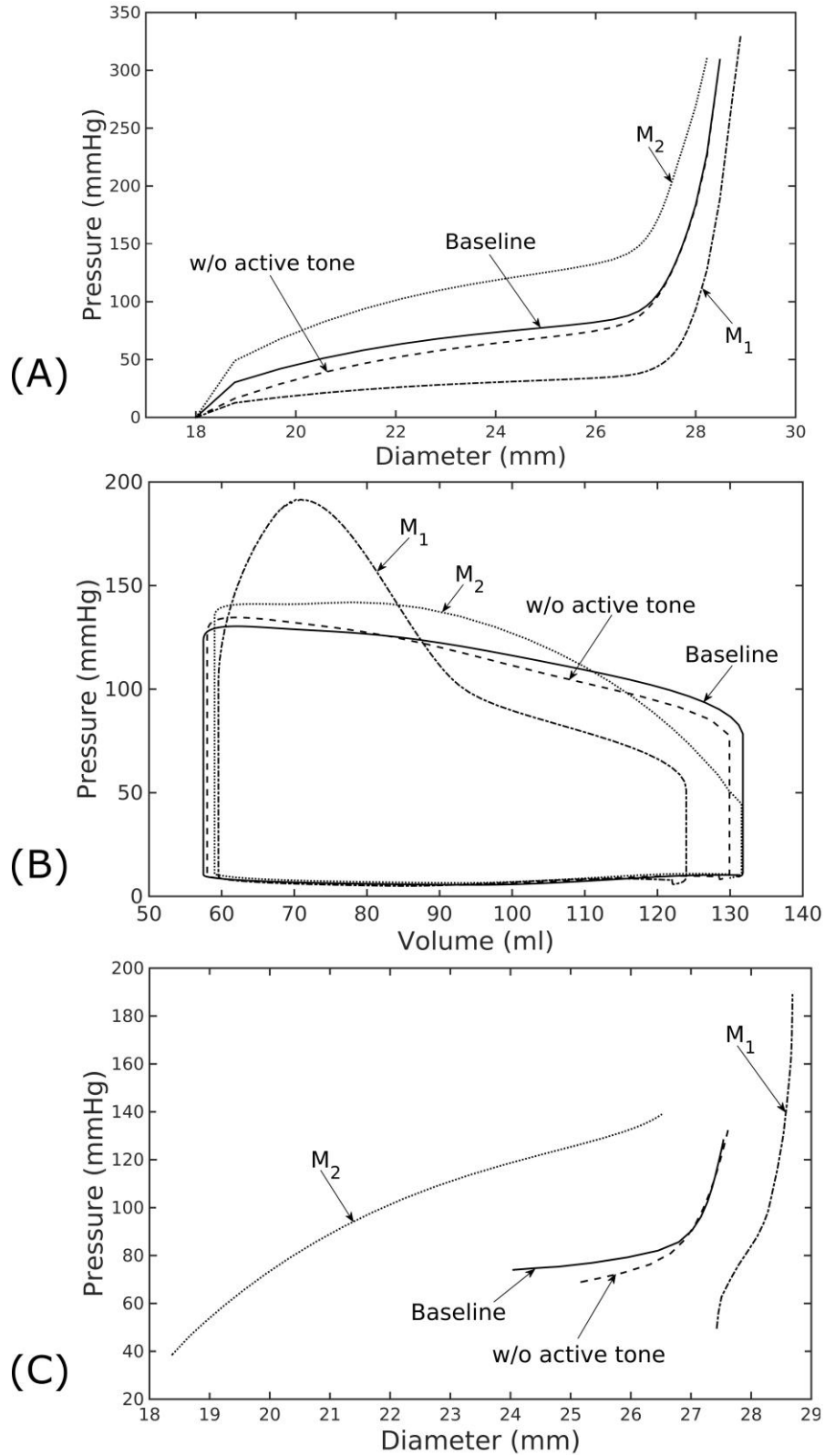


**Figure 5.4.** Effects of active tone and aorta constituent mass fractions on (A) its *ex-vivo* pressure–diameter relationship, (B) LV pressure–volume loop and (C) pressure - diameter both operating *in-vivo*. (Refer to **Table 5.5** for cases).

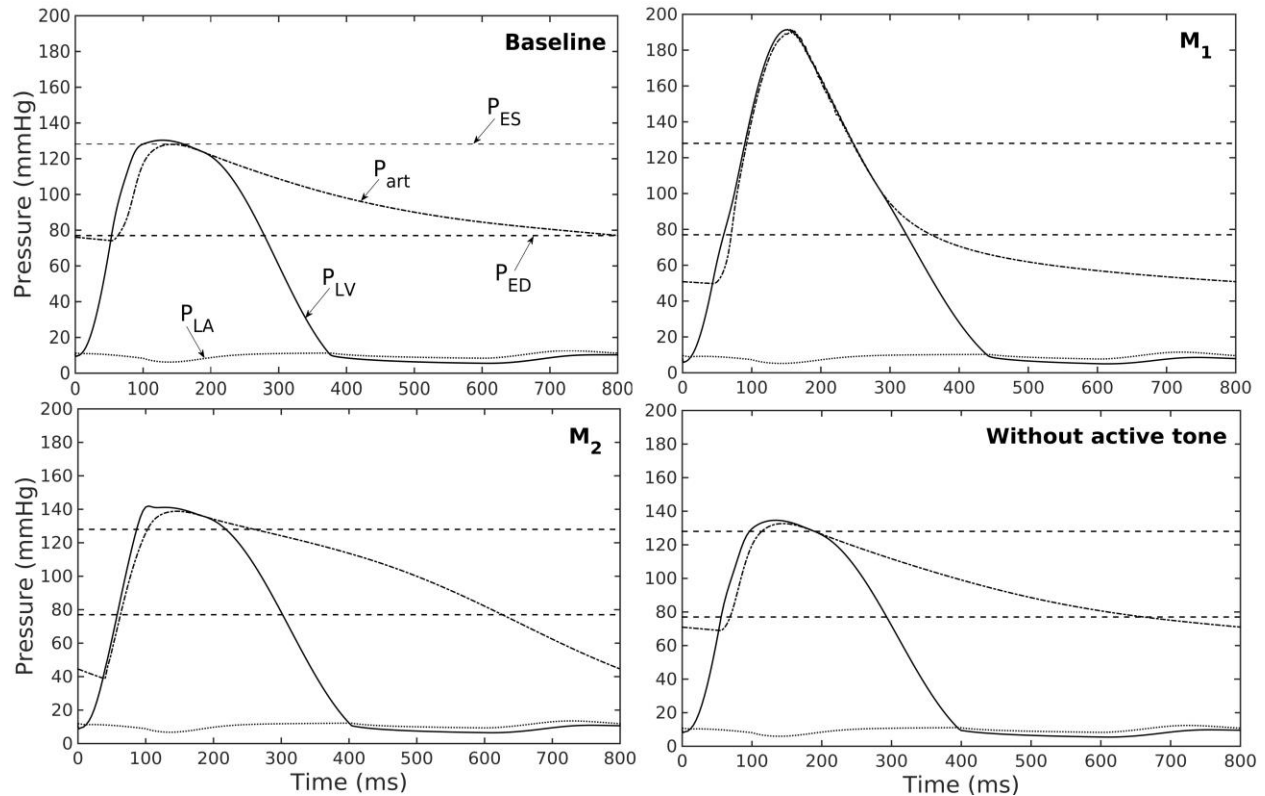


**Figure 5.5.** Pressure in LV, aorta and LA during cardiac cycle for different aorta constituent mass fractions and active tone.

### 5.3.2 Effect of changes in mass fractions of the aorta constituents

Similarly, varying mass fraction of the constituents in the aorta wall (see **Table 5.5** for the different cases) also led to changes in both the aorta and LV functions. Increasing collagen mass fraction with a corresponding decrease in SMC and elastin mass fractions (case  $M_1$ ) led to a predominantly exponential pressure - diameter response of the aorta that became extremely steep at larger diameter (i.e., > 28 mm) (**Figure 5.4A**). This is because the collagen fibers are stiffer than other constituents at large strain. Under *in vivo* operating condition (as simulated in the LV-aorta coupling framework), an increase in collagen mass fraction resulted in a higher peak systolic pressure and a reduced LV EF (**Figure 5.4B**). The exponential mechanical response (shown in **Figure 5.4A**) of the aorta with higher collagen mass fraction was also reflected in the ejection phase of the LV pressure-volume loop, where the pressure-volume curve became steeper towards

end-of-systole. With a higher collagen mass fraction, the aorta also operated at a larger diameter than the baseline *in vivo* (**Figure 5.4C**). Pulse pressure in the aorta with higher collagen mass fraction was much higher and dropped more rapidly when compared to the baseline case (**Figure 5.5**).

Conversely, reducing collagen mass fraction and increasing elastin and SMC mass fraction proportionally (case M<sub>2</sub>) led to a dominant neo-Hookean type pressure - diameter behavior, particularly, at smaller diameter (< 25 mm). Under *in vivo* operating condition, the peak pressure increased slightly but EF remained nearly unchanged in the LV (**Figure 5.4B**). The aorta also appeared to be more compliant *in vivo* with a larger change in aortic diameter (~ 8.1 mm), especially when compared to case M<sub>1</sub> that has a higher collagen mass fraction (~ 1.3 mm) (**Figure 5.4C**). On the other hand, the aorta also operated at smaller ED and ES diameters than the baseline. Pressure waveforms of the aorta, LV and LA were not significantly changed compared to the baseline (**Figure 5.5**).

In the absence of SMC's active tone, the aorta became slightly more compliant than the baseline at diameter smaller than 27 mm (**Figure 5.4A**). Thus, for a given pressure, the diameter was larger than the baseline. Under *in vivo* operating condition, this change led to a slight increase in the LV and aorta pressure at ES than the baseline (**Figure 5.4B, C**). On the other hand, LV and aorta pressure at ED decreased without the active tone (**Figure 5.4B, C**), resulting in an increase in the aortic pulse pressure compared to baseline (**Figure 5.5**).

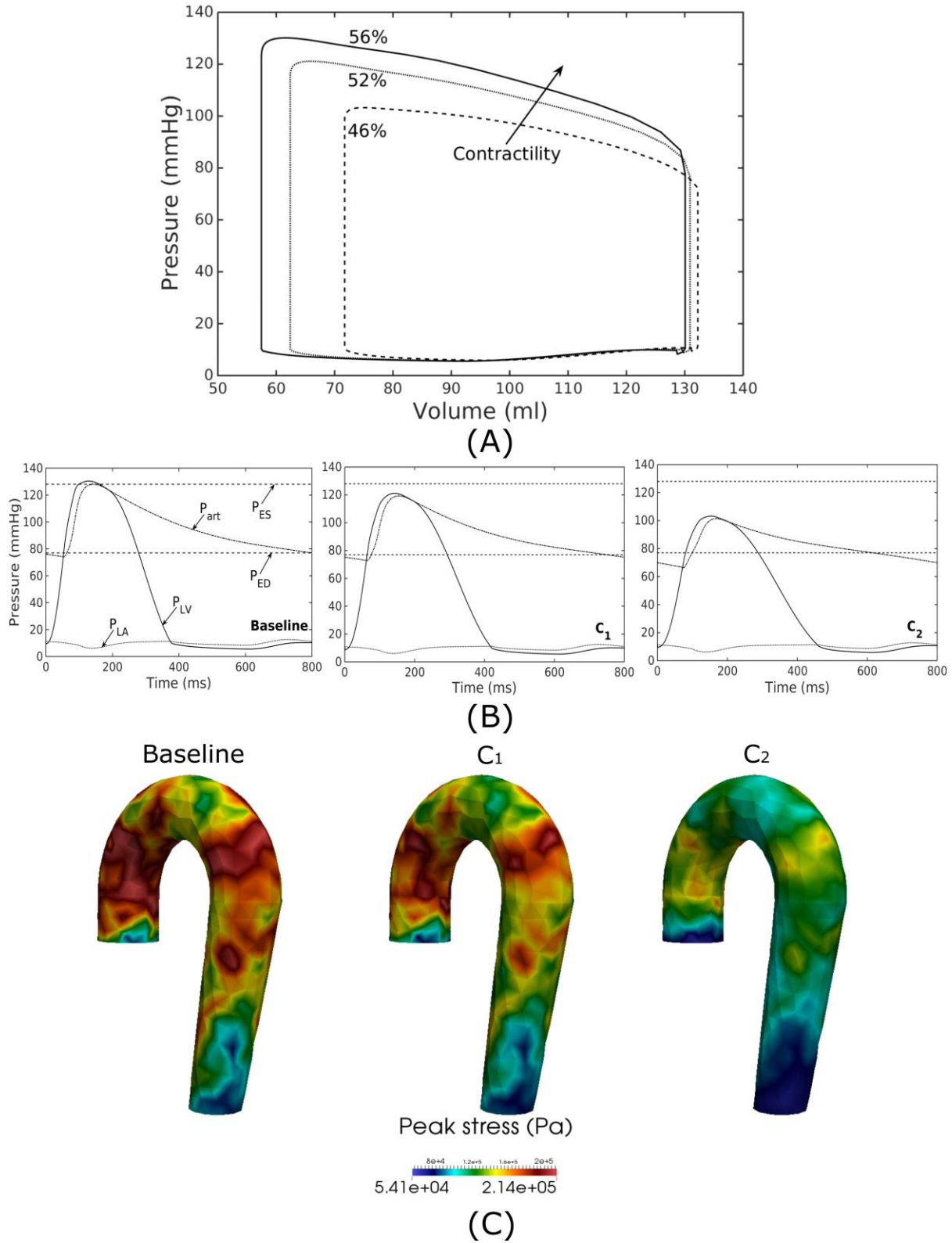


**Figure 5.6.** Effects of changes in LV contractility on (A) pressure-volume loop, (B) pressure waveform in LV, aorta and LA during cardiac cycle, and (C) peak stress in aorta. Contractility decreases in the following order: Baseline, C<sub>1</sub>, C<sub>2</sub>.

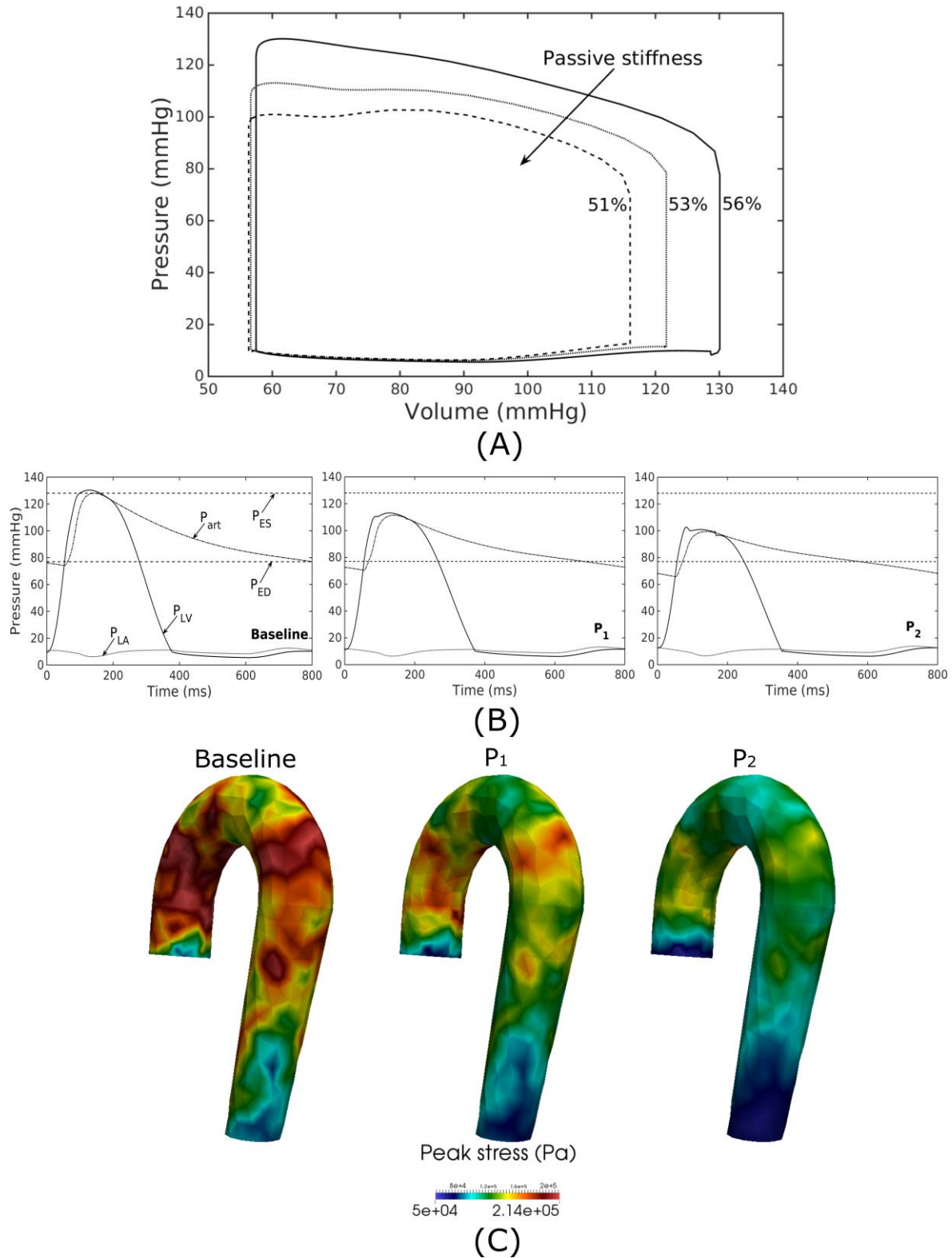


**Figure 5.7.** Effects of changes in LV passive stiffness on (A) pressure-volume loop, (B) pressure waveform in LV, aorta and LA during cardiac cycle, and (C) peak stress in aorta. Passive stiffness increases in the following order: Baseline, P<sub>1</sub>, P<sub>2</sub>.

### 5.3.3 Effects of a change in LV contractility

Reducing LV contractility ( $T_{max}$ ) led to a decrease in its peak systolic pressure, end systolic volume and EF (**Figure 5.6A**). Pressure also dropped accordingly (**Figure 5.6B**) in the aorta together with the peak stress (**Figure 5.6C**). With a reduction in LV contractility by 50 % (from 200.7 to 100.4 kPa), aorta peak stress was reduced by about 50% compared to the baseline case (from 214 to 110 kPa). The stress was calculated as a root of the sum of the square of all components of the Cauchy stress tensor. Reducing LV contractility also led to changes in the aorta diameter. As a result of lower LV contractility, the aortic pressure decreased that led to less expansion and a decrease in both its ED (from 24.0 mm in baseline to 22.5 mm in case C<sub>2</sub>) and ES diameter (from 27.5 mm in baseline to 27.0 mm in case C<sub>2</sub>).

### 5.3.4 Effects of a change in LV passive stiffness

Increasing the LV passive stiffness (parameter  $C$ ) in Eq. (4.12a) led to a stiffer end diastolic pressure – volume relationship that was accompanied by a reduction in preload, peak systolic pressure and EF (as end systolic volume remained nearly unchanged) in the chamber (**Figure 5.7A**). These changes were translated to a decrease in aortic pressure and peak stress (**Figure 5.7B, C**) as well as a reduction in its ED (from 24.0 mm in baseline to 22.4 mm in case P<sub>2</sub>) and ES (from 27.5 mm in baseline to 27.1 mm in case P<sub>2</sub>) diameters.

## 5.4 Discussion

Finite element models of the LV have been widely used in the literature to study its mechanics as well as organ-scale physiological behaviors in the cardiac cycle<sup>83,101,144,164,174</sup>. In these models, the aorta is usually represented within the lumped parameter circulatory model by its electrical analog, which cannot separate the effects its geometry, microstructure, and constituents' mechanical

behavior have on the LV's operating behavior *in vivo* and vice versa. To the best of our knowledge, this is the first computational modeling framework in which FE models of the aorta and LV are coupled in a closed-loop fashion. This framework enables us to take into detailed account of the geometrical, microstructural, and mechanical behavior of the LV and aorta. We have shown here that the coupled LV - aorta FE framework is able to capture physiological behaviors in both the LV and aorta that are consistent with *in vivo* measurements. We also showed that the framework can reasonably predict the effects of changes in geometry and microstructural details the two compartments have on each other over the cardiac cycle.

Using a detailed FE model of the aorta has enabled us to separate the contributions of the key load bearing constituents (elastin, collagen fibers and SMCs) have on its mechanical behavior. The aorta FE model predicted a pressure – diameter response in which the mechanical behavior of each constituent is clearly detectable (**Figure 5.2A**). For instance, mechanical behavior of aorta at lower diameter range (low stretch) is relatively compliant as it is largely endowed by elastin but exhibits a very stiff behavior at the higher diameter range (high stretch) when more collagen fibers are recruited. The behavior is consistent with previous experimental studies<sup>92,134,139</sup>. The pressure – diameter relationship predicted by our model (**Figure 5.2A**) resembled a S-shaped curve with a very stiff response after the inflection point that is a typical feature of large proximal arterial vessels<sup>14,159</sup>.

Our model predicted that an increase in aortic wall thickness led it to become more constricted with smaller ED and ES diameter under *in vivo* operating conditions when coupled to the LV in our modeling framework (**Figure 5.2C**). Systolic blood pressure and pulse pressure in the aorta increased as a result and was accompanied by a reduction in stroke volume and an increase in LV peak systolic pressure (**Figure 5.2B**). Although previous vascular studies suggest

that an increase in arterial wall thickness (that may be accompanied by an increase in stiffness) is a result from an increase blood pressure during aging, more recent evidence have suggested that stiffening is a cause for the increase in blood pressure in which a positive feedback loop between them proceeds gradually<sup>70</sup>. These features are consistent with those found in clinical and experimental studies. Specifically, it has been found that the mean aortic wall thickness increases with age<sup>104,137</sup> in human, which increases the risk of hypertension and atherosclerosis. Similarly, our model predicted that an increase in aortic wall thickness by 70 % elevates the aortic pressure over the hypertensive range ( $> 140$  mmHg) (**Figure 5.3**).

Changes in the aorta microstructure is a feature of pathological remodeling as well as aging. In the systemic vasculature, the proximal aorta has a compliant behavior that helps to keep the systolic blood pressure down. With aging, however, elastin degenerates and is replaced (i.e., compensated) by collagen in the aorta wall<sup>92,138,163</sup>. Consequently, the collagen fibers bear more of the load that substantially increases the aorta wall stiffness, especially at high stretch. A stiffer aorta leads to many adverse effects including elevated systolic and pulse pressure during ejection, faster decay in the aortic pressure waveform during diastole, and an increase in ventricular afterload that reduces the LV EF<sup>21</sup>. These behaviors are all captured in our framework when collagen and elastin mass fractions were increased and decreased, respectively. Specifically, these microstructural changes led to a reduction in EF (**Figure 5.4B**) and an increase in the aortic systolic and pulse pressure with a faster decay of aortic pressure waveform (**Figure 5.5**). Our framework also predicted that the aorta underwent more expansion *in vivo* and have a larger operating diameter when collagen mass fraction increases (**Figure 5.4C**), which is another key characteristic of aging<sup>14,35,110</sup>. Interestingly, changes in collagen mass fraction in the aorta (that lead to it stiffen at high stretch) also affects the shape of the LV pressure volume loop (**Figure 5.4B**, case M<sub>1</sub>).

Specifically, a rapid steepening of the LV pressure-volume curve near end-of-systole is predicted by our model when collagen mass fraction is increased. This result suggests that the shape of the LV pressure-volume loop may also reflect, to some extent, the accumulation of collagen fibers in the aorta during remodeling.

Our framework also predicted how changes in the contractility and passive stiffness of the LV affects the aorta function. A decrease in LV contractility led to lower LV EF, lower aortic systolic and pulse pressures, as well as a reduction in the aorta peak stress during the cardiac cycle (**Figure 5.6**). A change in contractility (or inotropic state of the myocardium) produced expected changes<sup>25,74</sup> in the LV pressure - volume loop and aortic pulse pressure. Similarly, the model predicted results from a change in the LV passive stiffness that are consistent with experimental observations (**Figure 5.7**). With increasing passive stiffness, LV EF decreases and is accompanied by a corresponding decrease in aortic systolic and pulse pressure, as well as peak stress. A change in the passive stiffness of LV due to, such as, an alteration of lusitropy, also shows similar changes in the LV pressure - volume loops<sup>25,74</sup> as well as aortic pressure.

Most clinical studies focus either on the behavior of the LV or aorta. While a number of studies have investigated ventricular - arterial coupling<sup>9,21,76,94</sup>, simplified indices (such as ratio of end-systolic volume to stroke volume) were used in them to describe this coupling. It is, however, impossible to separate the contribution of microstructure, mechanical behavior and geometry of the aorta (e.g., diameter or thickness) and LV to any changes in ventricular – arterial coupling. The framework described here helps overcome this limitation and may be useful for developing more insights of the ventricular – arterial interaction and will be extended in future to include the pulmonary vasculature for a more complete understanding of the interactions between the heart and vasculature under different physiological or pathological conditions.

### 5.4.1 Limitations

We have shown that our coupled LV-aorta FE modeling framework is capable of predicting behaviors that are consistent with measurements. There are, however, some limitations associated with our model. First, idealized geometries were used to represent the aorta and LV models. The idealized half-prolate geometry of the LV used here neglected any asymmetrical geometrical features while the aorta geometry was also simplified and had uniform thickness. Because wall thickness decreases slightly along the aorta<sup>114</sup>, its displacement with the given material parameters may be under-estimated. Second, we have assumed homogeneous material properties in our models. Given that studies have suggested that the mechanical properties may be inhomogeneous in the aorta<sup>86</sup> and LV<sup>87</sup>, the prescribed material parameters are bulk quantities. While thoracic aortic wall thickness and its stiffness varies, previous experimental studies reported that the aortic structural stiffness (multiplying the intrinsic stiffness by the aortic thickness) is relatively uniform in the circumferential and longitudinal directions<sup>89,90</sup>. Third, the dynamical behavior of fluid and its interaction with the vessel wall were neglected here, and as such, the framework did not take into account the spatial variation of pressure waveform along the aortic tree and shear stress on the luminal surface of the vessel. However, we do not expect this limitation to severely affect our result because wall shear stress in the human aorta ( $\sim 50 \text{ dyn/cm}^2$  or  $0.037 \text{ mmHg}$ )<sup>95</sup> is substantially lower than the pressure (normal stress) ( $60 - 120 \text{ mm Hg}$ ), and the arterial pressure increases by only about 10% from the ascending to the abdominal aorta<sup>149</sup>. Fourth, a rule based myofiber orientation in which the helix angle varies linearly across the myocardial wall was used to describe the LV microstructure. Fifth, remodeling of the aorta and LV was simulated by directly manipulating the parameters without consideration of any growth and remodeling mechanisms.

Last, we have considered only systemic circulation in this model and ignored the presence of the right ventricle and pulmonary circulatory system that may affect LV and aorta mechanics.

### **5.5 Extension to biventricular model with ventricular-vascular interaction**

As discussed in detail in chapter 1 (section 1.2.4), ventricular-vascular interaction (or, coupling) plays a very important role in the cardiovascular system and any deviations from optimal ventricular-vascular coupling are usually associated with the heart diseases<sup>21</sup>. Heart failure with preserved ejection fraction (HFpEF) has been associated with a progressively impaired coupling between the LV and the systemic arteries<sup>21,76</sup>. On the other hand, the interactions between the right ventricle (RV) and the pulmonary vasculature are key determinants of the clinical course of pulmonary arterial hypertension<sup>120</sup>, specifically, in the transition from compensated to decompensated remodeling of the RV. This interaction is currently not well-understood<sup>20</sup>. Therefore, we have developed a computational modeling framework that couples high resolution biventricular, aorta and pulmonary artery (PA) FE models to a closed-loop lumped parameter model of the systemic and pulmonary circulation. This modeling framework can accommodate 3D patient-specific FE models of ventricles, aorta and PA. Additionally, the ventricular and vascular (aorta and PA) models have realistic description of their microstructure with constitutive laws that can accurately describe their material behavior. The long-term goal is to develop a realistic and patient-specific 3D computational model and with proper parameterization, this model could be very useful to understand the ventricular-vascular interactions in both systemic and pulmonary circulation.

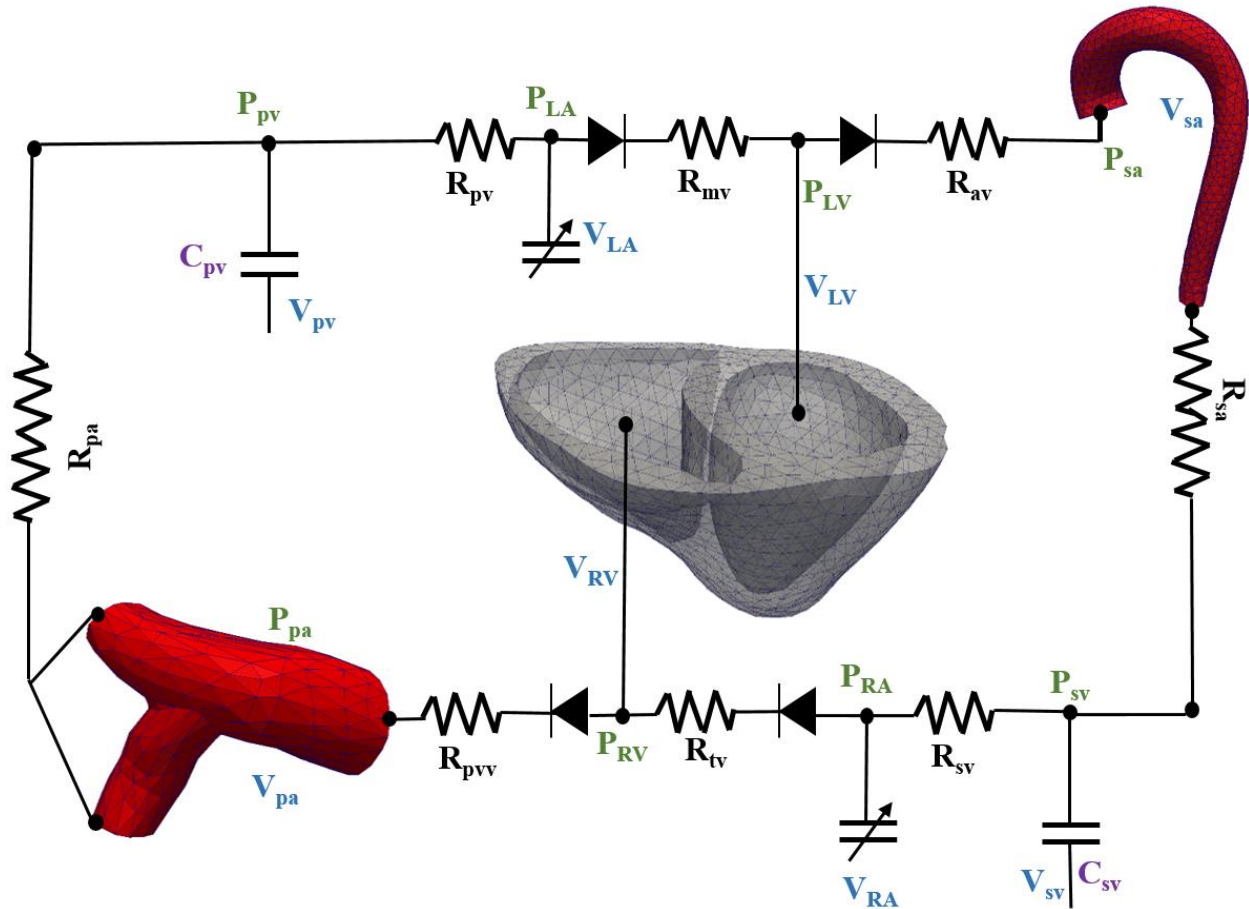


**Figure 5.8.** Schematic of the ventricular-vascular coupling modeling framework. Model consists of image-based high resolution biventricular, aorta and pulmonary artery FE models that are coupled to closed-loop lumped parameter model in systemic and pulmonary circulation.

### 5.5.1 Methods

The biventricular, aorta and PA FE models were reconstructed from the MR images of patients (**Figure 5.8**). For aorta we have considered the ascending part, the arch and the descending part up to the thoracic region. We have disregarded the small arteries (Innominate, left common carotid and left subclavian arteries) that branches out from the arch of aorta. On the other hand, we consider the main PA as well as both the truncated left and right PA branches that were reconstructed from MR images.

An active stress formulation was used to describe the mechanical behavior of ventricles in the cardiac cycle which is discussed in detail in chapter 4, section 4.2.5. In this formulation, the stress tensor  $\mathbf{P}$  was decomposed additively into a passive component  $\mathbf{P}_p$  and an active component  $\mathbf{P}_a$  (i.e.,  $\mathbf{P} = \mathbf{P}_a + \mathbf{P}_p$ ). The LV and RV myofiber direction was varied with linear transmural variation of the helix angle from  $60^\circ$  at the endocardium to  $-60^\circ$  at the epicardium based on previous experimental measurements<sup>153</sup>.

For aorta and PA, a membrane model was used in which the contributions of the key tissue constituents, namely, elastin-dominated matrix, collagen fiber families and vascular smooth muscle cells (SMC) were considered in the strain energy functions (Discussed in detail in section 5.2.6). Four collagen fiber families were considered here with the first and second families of collagen fibers oriented in the axial and circumferential directions, whereas the third and fourth families of collagen fibers were oriented, respectively, at an angle  $\alpha = 45^\circ$  and  $-45^\circ$  with respect to the axial direction.

The pressure-volume relationships of the ventricles, aorta and PA were obtained using the FE model. For left and right atrium, a time-varying elastance model was to establish the functional relationship between the pressure and volume. For, systemic and pulmonary veins, a linear pressure-volume relationship were assumed which depends on the compliance of the vessels.

Similar to the biventricular model discussed in chapter 4 section 4.2.3, the closed-loop lumped parameter model (**Figure 5.8**) consists of eight ordinary differential equations which related the rate of change of the volume of eight compartments to inflow and outflow. The eight flow equations were used to calculate the flow rates at different sections of the circulatory model by using the pressure and the resistance of the vessels. An explicit scheme was used to discretize

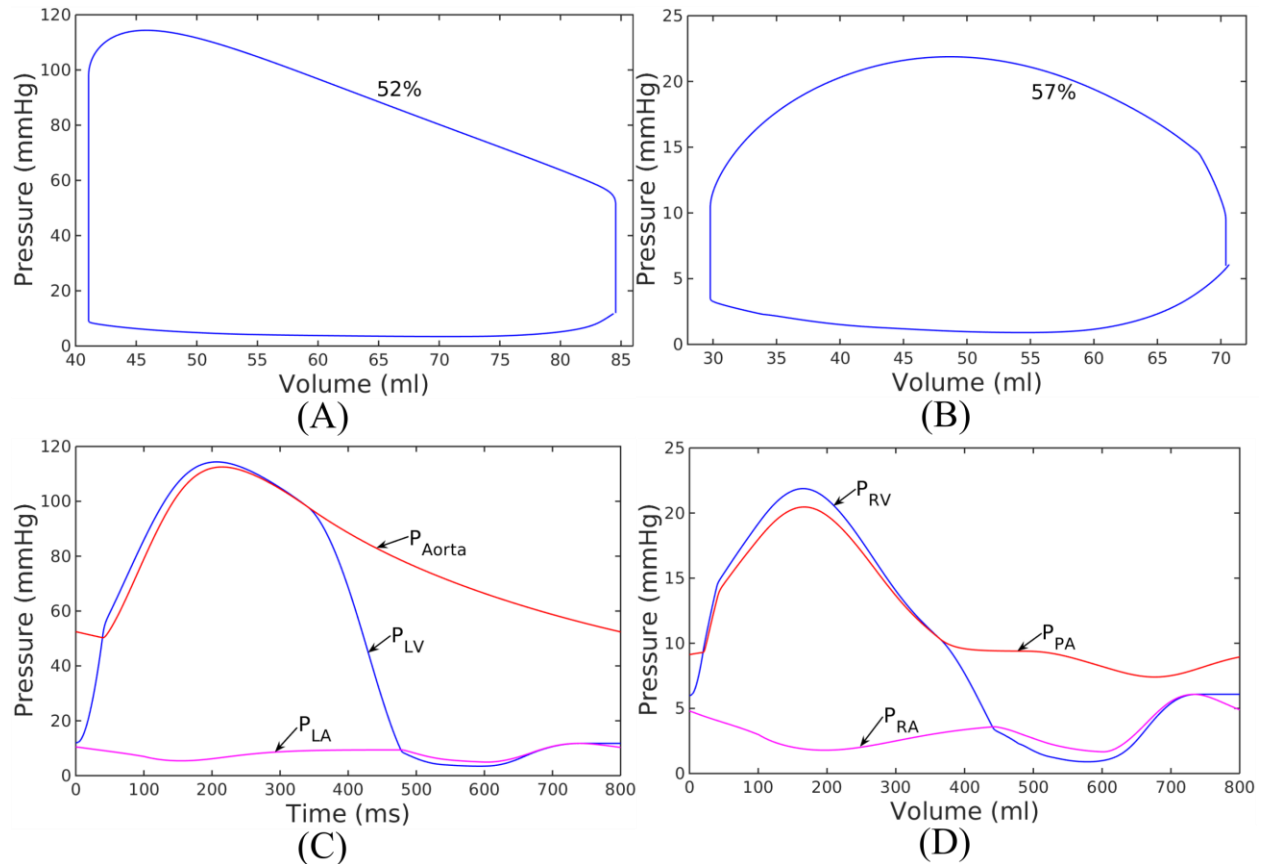


**Figure 5.9.** (A) LV, (B) RV PV loops, (C) LV, aorta and LA pressure waveforms, and (D) RV, PA and RA pressure waveforms as predicted by the model.

and simultaneously solve the eight ODEs. The modeling frame work was implemented using the open-source FE library FEniCS.

### 5.5.2 Results

We have calibrated our model to simulate the LV and RV loops and aorta and PA pressure waveforms that were consistent with measurements in the normal human (**Figure 5.9**). The LV and RV have EF of 52% and 57%, respectively ( $>50\%$ ). In addition, the LV, aorta, RV, and PA pressure waveforms fall within the range of measurements typically found in normal (**Figure 5.9C** and **D**).

### **5.5.3 Future work**

The results show that with proper calibration of the model parameters, our image-based modeling framework is able to predict the behaviors of the ventricles, aorta and PA that are consistent with the physiological principles. However, we need to improve some aspects of this model. The model can be calibrated to predict the pressure-diameter relationship of aorta and PA. In addition, the aorta and PA flow waveforms can be matched with the measured data.

After reasonably matching the geometry, pressure and volume waveforms of LV and RV, pressure and flow waveforms of aorta and PA as well as aorta and PA pressure-diameter relationship with measured data, our high-resolution patient specific modeling framework could be used to better understand the mechanics of these three organs and provide insights into ventricular-vascular interactions (or coupling) of the diseased heart in pulmonary and systemic circulation.

## CHAPTER 6

### Conclusions

In this dissertation, we have developed multiple computational modeling framework of human heart. In chapter 2, we have methodically validated a LV FE model that is driven by a cell-based descriptor of cross-bridge cycling against some well-established organ-level physiological behaviors. The model parameters were adjusted appropriately to confirm that it performs in a manner consistent with experimental observations on the impact of preload, afterload, and contractility on the ESPVR and  $MVO_2 - PVA$  relationships. Furthermore, the model can reproduce time-strain profiles that are consistent with physiological measurements. This model could be very useful to address important unanswered questions about human heart diseases that cannot be resolved through experimentation. We have demonstrated one such application in chapter 3.

In chapter 3, using our previously validated LV FE computational model (discussed in chapter 1), we replicated key aspects of ventricular geometry, chamber size, blood pressure LV EF and longitudinal strain reported in HFpEF patients. Optimal matching of model prediction to all these features was achieved only through simultaneous increases in ventricular afterload resistance and reduction of myocardial contractility. Thus, we conclude that the reduction of longitudinal strain does reflect a reduction of myocardial contractility in HFpEF and is not simply a reflection of increased afterload or altered geometry. This reinforces the previously proposed intriguing notion as to whether therapies that improve myocardial contractility could have a therapeutic role in HFpEF.

In chapter 4, we have developed an image based biventricular FE modeling framework that was coupled to a closed-loop lumped parameter model of systemic and pulmonary circulation. We have successfully calibrated our model to match the patient specific measurements of two PAH

patients with different stage of RV remodeling. The calibrated computational framework was used to simulate the effects of RVAD on the hemodynamics and mechanics of two PAH patients. We have found that RVAD improves RV mechanics and septum curvature which was more pronounced in the PAH patient with severely remodeled RV. However, the positive effects are accompanied with an increase in PA pressure that could be detrimental for these patients. The findings of our study suggest that the implantation of RVAD and its operation may need to be determined and optimized individually for each patient depending on disease progression.

Finally, in chapter 5, we presented a computational model that couples FE models of the LV and aorta to describe ventricular-arterial interaction in the systemic circulation. With appropriate calibration, our model was able to simulate how alterations in the geometrical or microstructural change of the aorta affect the LV and vice versa. The modeling framework is extended to include image-based FE models of the ventricles, aorta and pulmonary artery. This novel patient-specific computational framework will be refined in future and could be very useful to develop more insights on the complex ventricular interdependence and ventricular-vascular interactions (or coupling) associated with diseased hearts.

## BIBLIOGRAPHY

## BIBLIOGRAPHY

1. Adeniran I, Hancox JC, Zhang H. Effect of cardiac ventricular mechanical contraction on the characteristics of the ECG: A simulation study. *J Biomed Sci Eng.* 2013;06(12):47-60. doi:10.4236/jbise.2013.612A007.
2. Adeniran I, Hancox JC, Zhang H. In silico investigation of the short QT syndrome, using human ventricle models incorporating electromechanical coupling. *Front Physiol.* 2013;4:166. doi:10.3389/fphys.2013.00166.
3. Adeniran I, MacIver DH, Hancox JC, Zhang H. Abnormal calcium homeostasis in heart failure with preserved ejection fraction is related to both reduced contractile function and incomplete relaxation: an electromechanically detailed biophysical modeling study. *Front Physiol.* 2015;6:78. doi:10.3389/fphys.2015.00078.
4. Aelen FW, Arts T, Sanders DG, et al. Relation between torsion and cross-sectional area change in the human left ventricle. *J Biomech.* 1997;30(3):207-212.
5. Aguado-Sierra J, Krishnamurthy A, Villongco C, et al. Patient-specific modeling of dyssynchronous heart failure: A case study. *Prog Biophys Mol Biol.* 2011;107(1):147-155. doi:10.1016/j.pbiomolbio.2011.06.014.
6. Alnæs M, Blechta J, Hake J, et al. The FEniCS Project Version 1.5. *Arch Numer Softw.* 2015;3(100). doi:10.11588/ANS.2015.100.20553.
7. Altmayer SPL, Joyce Han Q, Addetia K, Patel AR, Forfia PR, Han Y. Using all-cause mortality to define severe RV dilation with RV/LV volume ratio. *Sci Rep.* 2018. doi:10.1038/s41598-018-25259-1.
8. Angeja BG, Grossman W. Evaluation and management of diastolic heart failure. *Circulation.* 2003;107(5):659-663. <http://www.ncbi.nlm.nih.gov/pubmed/12578862>. Accessed November 9, 2018.
9. Antonini-Canterin F, Pavan D, Bello V, Nicolosi G, Poli S, Vriza O. The ventricular-arterial coupling: From basic pathophysiology to clinical application in the echocardiography laboratory. *J Cardiovasc Echogr.* 2013;23(4):91. doi:10.4103/2211-4122.127408.
10. Arts T, Delhaas T, Bovendeerd P, Verbeek X, Prinzen F. Adaptation to mechanical load determines shape and properties of heart and circulation: the CircAdapt model. *Am J Physiol Heart Circ Physiol.* 2005;288:1943-1954. doi:10.1152/ajpheart.00444.2004.
11. Asif M, Egan J, Vasani S, et al. An advanced glycation endproduct cross-link breaker can reverse age-related increases in myocardial stiffness. *Proc Natl Acad Sci.* 2000. doi:10.1073/pnas.040558497.
12. Avazmohammadi R, Hill M, Simon M, Sacks M. Transmural remodeling of right

- ventricular myocardium in response to pulmonary arterial hypertension. *APL Bioeng.* 2017;1(1):16105. doi:10.1063/1.5011639.
13. Avazmohammadi R, Mendiola EA, Soares JS, et al. A Computational Cardiac Model for the Adaptation to Pulmonary Arterial Hypertension in the Rat. *Ann Biomed Eng.* 2019;47(1):138-153.
  14. Bader H. Dependence of Wall Stress in the Human Thoracic Aorta on Age and Pressure. *Circ Res.* 1967;20(3):354 LP-361. <http://circres.ahajournals.org/content/20/3/354.abstract>.
  15. Baek S, Valentín A, Humphrey JD. Biochemomechanics of cerebral vasospasm and its resolution: II. Constitutive relations and model simulations. *Ann Biomed Eng.* 2007;35(9):1498-1509. doi:10.1007/s10439-007-9322-x.
  16. Bassingthwaite JB, Chizeck HJ, Atlas LE. Strategies and tactics in multiscale modeling of cell-to-organ systems. *Proc IEEE.* 2006;94(4):819-830. doi:10.1109/JPROC.2006.871775.
  17. Bayer JD, Blake RC, Plank G, Trayanova NA. A novel rule-based algorithm for assigning myocardial fiber orientation to computational heart models. *Ann Biomed Eng.* 2012;40(10):2243-2254. doi:10.1007/s10439-012-0593-5.
  18. Bhatia RS, Tu J V, Lee DS, et al. Outcome of heart failure with preserved ejection fraction in a population-based study. *N Engl J Med.* 2006;355(3):260-269. doi:10.1056/NEJMoa051530.
  19. Borbély A, Van Der Velden J, Papp Z, et al. Cardiomyocyte stiffness in diastolic heart failure. *Circulation.* 2005;111(6):774-781. doi:10.1161/01.CIR.0000155257.33485.6D.
  20. Borgdorff MAJ, Dickinson MG, Berger RMF, Bartelds B. Right ventricular failure due to chronic pressure load: What have we learned in animal models since the NIH working group statement? *Heart Fail Rev.* 2015;20(4):475-491. doi:10.1007/s10741-015-9479-6.
  21. Borlaug BA, Kass DA. Ventricular-Vascular Interaction in Heart Failure. *Cardiol Clin.* 2011;29(3):447-459. doi:10.1016/j.ccl.2011.06.004.
  22. Borlaug BA, Lam CSP, Roger VL, Rodeheffer RJ, Redfield MM. Contractility and ventricular systolic stiffening in hypertensive heart disease insights into the pathogenesis of heart failure with preserved ejection fraction. *J Am Coll Cardiol.* 2009;54(5):410-418. doi:10.1016/j.jacc.2009.05.013.
  23. Borlaug BA, Paulus WJ. Heart failure with preserved ejection fraction: pathophysiology, diagnosis, and treatment. *Eur Heart J.* 2011;32(6):670-679. doi:10.1093/eurheartj/ehq426.
  24. Borlaug BA, Paulus WJ. Heart failure with preserved ejection fraction: pathophysiology, diagnosis, and treatment. *Eur Heart J.* 2011;32(6):670-679. doi:10.1093/eurheartj/ehq426.
  25. Burkhoff D. Assessment of systolic and diastolic ventricular properties via pressure-

- volume analysis: a guide for clinical, translational, and basic researchers. *AJP Hear Circ Physiol*. 2005;289(2):H501-H512. doi:10.1152/ajpheart.00138.2005.
26. Burkhoff D. Explaining load dependence of ventricular contractile properties with a model of excitation-contraction coupling. *J Mol Cell Cardiol*. 1994;26(8):959-978. doi:10.1006/jmcc.1994.1117.
  27. Burkhoff D. Mechanical Properties of the Heart and Its Interaction with the Vascular System. *Heart*. 2011.
  28. Burkhoff D. Pressure-volume loops in clinical research. *J Am Coll Cardiol*. 2013. doi:10.1016/j.jacc.2013.05.049.
  29. Burkhoff D, de Tombe PP, Hunter WC, Kass DA. Contractile strength and efficiency of left ventricle are enhanced and efficiency by physiological afterload. *Am J Hear Circ Physiol*. 1991;260:569-578.
  30. Butler J, Hamo CE, Udelson JE, et al. Exploring New Endpoints for Patients with Heart Failure with Preserved Ejection Fraction. *Circ Hear Fail*. 2016. doi:10.1161/CIRCHEARTFAILURE.116.003358.
  31. Campbell SG, Flaim SN, Leem CH, McCulloch AD. Mechanisms of transmurally varying myocyte electromechanics in an integrated computational model. *Philos Trans A Math Phys Eng Sci*. 2008;366(1879):3361-3380. doi:10.1098/rsta.2008.0088.
  32. CDC N. Underlying Cause of Death 1999-2013. CDC WONDER Online Database.
  33. Chen WW, Gao H, Luo XY, Hill NA. Study of cardiovascular function using a coupled left ventricle and systemic circulation model. *J Biomech*. 2016. doi:10.1016/j.jbiomech.2016.03.009.
  34. Constantino J, Hu Y, Trayanova NA. A computational approach to understanding the cardiac electromechanical activation sequence in the normal and failing heart, with translation to the clinical practice of CRT. *Prog Biophys Mol Biol*. 2012;110(2-3):372-379. doi:10.1016/j.pbiomolbio.2012.07.009.
  35. Craiem D, Casciaro ME, Graf S, Chironi G, Simon A, Armentano RL. Effects of aging on thoracic aorta size and shape: A non-contrast CT study. In: *2012 Annual International Conference of the IEEE Engineering in Medicine and Biology Society*. Vol 2012. IEEE; 2012:4986-4989. doi:10.1109/EMBC.2012.6347112.
  36. Dabiri Y, Sack KL, Shaul S, Sengupta PP, Guccione JM. Relationship of transmural variations in myofiber contractility to left ventricular ejection fraction: Implications for modeling heart failure phenotype with preserved ejection fraction. *Front Physiol*. 2018. doi:10.3389/fphys.2018.01003.
  37. Dandel M, Lehmkühl H, Knosalla C, Suramashvili N, Hetzer R. Strain and strain rate imaging by echocardiography - basic concepts and clinical applicability. *Curr Cardiol*

- Rev.* 2009;5(2):133-148. doi:10.2174/157340309788166642.
38. Dang AB, Guccione JM, Mishell JM, et al. Akinetic myocardial infarcts must contain contracting myocytes: finite-element model study. *Am J Physiol Hear Circ Physiol.* 2005;288:H1844-50. doi:10.1152/ajpheart.00961.2003.
  39. Donaldson C, Palmer BM, Zile M, et al. Myosin cross-bridge dynamics in patients with hypertension and concentric left ventricular remodeling. *Circ Hear Fail.* 2012;5(6):803-811. doi:10.1161/CIRCHEARTFAILURE.112.968925.
  40. Finsberg H, Xi C, Tan J Le, et al. Efficient estimation of personalized biventricular mechanical function employing gradient-based optimization. *Int j numer method biomed eng.* 2018;34(7). doi:10.1002/cnm.2982.
  41. Fonarow GC, Stough WG, Abraham WT, et al. Characteristics, Treatments, and Outcomes of Patients With Preserved Systolic Function Hospitalized for Heart Failure. A Report From the OPTIMIZE-HF Registry. *J Am Coll Cardiol.* 2007;50(8):768-777. doi:10.1016/j.jacc.2007.04.064.
  42. Freed BH, Tsang W, Bhawe NM, et al. Right Ventricular Strain in Pulmonary Arterial Hypertension: A 2D Echocardiography and Cardiac Magnetic Resonance Study. *Echocardiography.* 2014:n/a-n/a. doi:10.1111/echo.12662.
  43. Furukawa K, Motomura T, Nose Y. Right Ventricular Failure After Left Ventricular Assist Device Implantation: The Need for an Implantable Right Ventricular Assist Device. *Artif Organs.* 2005;29(5):369-377. doi:10.1111/j.1525-1594.2005.29063.x.
  44. Gao H, Wang H, Berry C, Luo X, Griffith BE. Quasi-static image-based immersed boundary-finite element model of left ventricle under diastolic loading. *Int j numer method biomed eng.* 2014;30(11):1199-1222. doi:10.1002/cnm.2652.
  45. Genet M, Lee LC, Baillargeon B, Guccione JM, Kuhl E. Modeling Pathologies of Diastolic and Systolic Heart Failure. *Ann Biomed Eng.* 2016;44(1):112-127. doi:10.1007/s10439-015-1351-2.
  46. Genet M, Lee LC, Nguyen R, et al. Distribution of normal human left ventricular myofiber stress at end diastole and end systole: a target for in silico design of heart failure treatments. *J Appl Physiol.* 2014;117(2):142-152. doi:10.1152/jappphysiol.00255.2014.
  47. Geuzaine C, Remacle JF. Gmsh: A 3-D finite element mesh generator with built-in pre- and post-processing facilities. *Int J Numer Methods Eng.* 2009;79(11):1309-1331. doi:10.1002/nme.2579.
  48. Giamouzis G, Schelbert EB, Butler J. Growing evidence linking microvascular dysfunction with heart failure with preserved ejection fraction. *J Am Heart Assoc.* 2016;5(2). doi:10.1161/JAHA.116.003259.
  49. Göktepe S, Abilez OJ, Parker KK, Kuhl E. A multiscale model for eccentric and

- concentric cardiac growth through sarcomerogenesis. *J Theor Biol.* 2010;265(3):433-442. doi:10.1016/j.jtbi.2010.04.023.
50. Gomez-Arroyo J, Sandoval J, Simon MA, Dominguez-Cano E, Voelkel NF, Bogaard HJ. Treatment for pulmonary arterial hypertension-associated right ventricular dysfunction. *Ann Am Thorac Soc.* 2014. doi:10.1513/AnnalsATS.201312-425FR.
  51. Gomez AD, Zou H, Bowen ME, Liu X, Hsu EW, McKellar SH. Right Ventricular Fiber Structure as a Compensatory Mechanism in Pressure Overload: A Computational Study. *J Biomech Eng.* 2017. doi:10.1115/1.4036485.
  52. Gorcsan J, Tanaka H. Echocardiographic assessment of myocardial strain. *J Am Coll Cardiol.* 2011;58(14):1401-1413. doi:10.1016/j.jacc.2011.06.038.
  53. Gorter TM, Willems TP, van Melle JP. Ventricular interdependence in pulmonary arterial hypertension: providing small pieces of a complex puzzle. *Eur J Heart Fail.* 2015;17(1):1-2. doi:10.1002/ejhf.195.
  54. Greenfield JC, Patel DJ. Relation Between Pressure and Diameter in the Ascending Aorta of Man. *Circ Res.* 1962;10(5):778-781. doi:10.1161/01.RES.10.5.778.
  55. Gregoric ID, Chandra D, Myers TJ, Scheinin SA, Loyalka P, Kar B. Extracorporeal Membrane Oxygenation as a Bridge to Emergency Heart-Lung Transplantation in a Patient With Idiopathic Pulmonary Arterial Hypertension. *J Hear Lung Transplant.* 2008. doi:10.1016/j.healun.2008.01.016.
  56. Guccione JM, McCulloch AD. Mechanics of active contraction in cardiac muscle: Part I--Constitutive relations for fiber stress that describe deactivation. *J Biomech Eng.* 1993;115(1):72-81. doi:10.1115/1.2895473.
  57. Guccione JM, McCulloch AD, Waldman LK. Passive material properties of intact ventricular myocardium determined from a cylindrical model. *J Biomech Eng.* 1991;113(February):42-55. doi:10.1115/1.2894084.
  58. Guccione JM, Waldman LK, McCulloch a D. Mechanics of active contraction in cardiac muscle: Part II--Cylindrical models of the systolic left ventricle. *J Biomech Eng.* 1993;115(1):82-90. doi:10.1115/1.2895474.
  59. Gurev V, Constantino J, Rice JJ, Trayanova N a. Distribution of electromechanical delay in the heart: insights from a three-dimensional electromechanical model. *Biophys J.* 2010;99(3):745-754. doi:10.1016/j.bpj.2010.05.028.
  60. Gurev V, Lee T, Constantino J, Arevalo H, Trayanova NA. Models of cardiac electromechanics based on individual hearts imaging data: Image-based electromechanical models of the heart. *Biomech Model Mechanobiol.* 2011;10(3):295-306. doi:10.1007/s10237-010-0235-5.
  61. Gurev V, Pathmanathan P, Fattbert JL, et al. A high-resolution computational model of

- the deforming human heart. *Biomech Model Mechanobiol.* 2015;14(4):829-849. doi:10.1007/s10237-014-0639-8.
62. Hall JE. *Guyton and Hall Textbook of Medical Physiology (12e).*; 2011. doi:10.1007/s13398-014-0173-7.2.
  63. He K-L, Burkhoff D, Leng W-X, et al. Comparison of ventricular structure and function in Chinese patients with heart failure and ejection fractions >55% versus 40% to 55% versus. *Am J Cardiol.* 2009;103(6):845-851. doi:10.1016/j.amjcard.2008.11.050.
  64. Hill MR, Simon MA, Valdez-Jasso D, Zhang W, Champion HC, Sacks MS. Structural and Mechanical Adaptations of Right Ventricle Free Wall Myocardium to Pressure Overload. *Ann Biomed Eng.* 2014;42(12):2451-2465. doi:10.1007/s10439-014-1096-3.
  65. Hoit BD. Strain and strain rate echocardiography and coronary artery disease. *Circ Cardiovasc Imaging.* 2011;4(2):179-190. doi:10.1161/CIRCIMAGING.110.959817.
  66. Hsu MC, Bazilevs Y. Blood vessel tissue prestress modeling for vascular fluidstructure interaction simulation. In: *Finite Elements in Analysis and Design.* Vol 47. ; 2011:593-599. doi:10.1016/j.finel.2010.12.015.
  67. Hu Y, Gurev V, Constantino J, Bayer JD, Trayanova NA. Effects of Mechano-Electric Feedback on Scroll Wave Stability in Human Ventricular Fibrillation. Talkachova A, ed. *PLoS One.* 2013;8(4):e60287. doi:10.1371/journal.pone.0060287.
  68. Hu Y, Gurev V, Constantino J, Trayanova N. Optimizing cardiac resynchronization therapy to minimize ATP consumption heterogeneity throughout the left ventricle: A simulation analysis using a canine heart failure model. *Heart Rhythm.* 2014;11:1063-1069. doi:10.1016/j.hrthm.2014.03.021.
  69. Humbert M, Sitbon O, Yaïci A, et al. Survival in incident and prevalent cohorts of patients with pulmonary arterial hypertension. *Eur Respir J.* 2010;36(3):549-555. doi:10.1183/09031936.00057010.
  70. Humphrey JD, Harriuson DG, Figueroa CA, Lacolley P, Laurent S. Central artery stiffness in hypertension and aging: A problem with cause and Consequence. *Circ Res.* 2016;118:379-381.
  71. Hunter PJ, McCulloch a D, ter Keurs HE. Modelling the mechanical properties of cardiac muscle. *Prog Biophys Mol Biol.* 1998;69(2-3):289-331.
  72. Jaïs X, Bonnet D. Treatment of pulmonary arterial hypertension. *Presse Med.* 2010;39 Suppl 1:S22-S32. doi:http://dx.doi.org/10.1056/NEJMra040291.
  73. Karimov JH, Sunagawa G, Horvath D, Fukamachi K, Starling RC, Moazami N. Limitations to Chronic Right Ventricular Assist Device Support. *Ann Thorac Surg.* 2016;102(2):651-658. doi:10.1016/j.athoracsur.2016.02.006.

74. Katz AM. Influence of altered inotropy and lusitropy on ventricular pressure-volume loops. *J Am Coll Cardiol*. 1988;11(2):438-445. doi:10.1016/0735-1097(88)90113-1.
75. Kaul TK, Kahn DR. Postinfarct refractory right ventricle: right ventricular exclusion. A possible option to mechanical cardiac support, in patients unsuitable for heart transplant. *J Cardiovasc Surg (Torino)*. 2000;41(3):349-355.  
http://www.ncbi.nlm.nih.gov/pubmed/10952322. Accessed February 14, 2019.
76. Kawaguchi M, Hay I, Fetcs B, Kass DA. Combined ventricular systolic and arterial stiffening in patients with heart failure and preserved ejection fraction: Implications for systolic and diastolic reserve limitations. *Circulation*. 2003;107(5):714-720.  
doi:10.1161/01.CIR.0000048123.22359.A0.
77. Kelly RP, Ting CT, Yang TM, et al. Effective arterial elastance as index of arterial vascular load in humans. *Circulation*. 1992;86(2):513-521. doi:10.1161/01.CIR.86.2.513.
78. Kelshiker M, Mayet J, Unsworth B, Okonko D. Basal Septal Hypertrophy. *Curr Cardiol Rev*. 2014. doi:10.2174/1573403X09666131202125424.
79. Kerckhoffs RCP, ed. *Patient-Specific Modeling of the Cardiovascular System*. New York, NY: Springer New York; 2010. doi:10.1007/978-1-4419-6691-9.
80. Kerckhoffs RCP, Bovendeerd PHM, Kotte JCS, Prinzen FW, Smits K, Arts T. Homogeneity of Cardiac Contraction Despite Physiological Asynchrony of Depolarization: A Model Study. *Ann Biomed Eng*. 2003;31(5):536-547.  
doi:10.1114/1.1566447.
81. Kerckhoffs RCP, McCulloch AD, Omens JH, Mulligan LJ. Effects of biventricular pacing and scar size in a computational model of the failing heart with left bundle branch block. *Med Image Anal*. 2009;13(2):362-369. doi:10.1016/j.media.2008.06.013.
82. Kerckhoffs RCP, Narayan SM, Omens JH, Mulligan LJ, McCulloch AD. Computational Modeling for Bedside Application. *Heart Fail Clin*. 2008;4(3):371-378.  
doi:10.1016/j.hfc.2008.02.009.
83. Kerckhoffs RCP, Neal ML, Gu Q, Bassingthwaighte JB, Omens JH, McCulloch AD. Coupling of a 3D finite element model of cardiac ventricular mechanics to lumped systems models of the systemic and pulmonic circulation. *Ann Biomed Eng*. 2007;35(1):1-18. doi:10.1007/s10439-006-9212-7.
84. Kerckhoffs RCP, Omens J, McCulloch AD. A single strain-based growth law predicts concentric and eccentric cardiac growth during pressure and volume overload. *Mech Res Commun*. 2012;42:40-50. doi:10.1016/j.mechrescom.2011.11.004.
85. Kerckhoffs RCP, Omens JH, McCulloch AD, Mulligan LJ. Ventricular dilation and electrical dyssynchrony synergistically increase regional mechanical nonuniformity but not mechanical dyssynchrony: a computational model. *Circ Heart Fail*. 2010;3(4):528-536. doi:10.1161/CIRCHEARTFAILURE.109.862144.

86. Kermani G, Hemmasizadeh A, Assari S, Autieri M, Darvish K. Investigation of inhomogeneous and anisotropic material behavior of porcine thoracic aorta using nano-indentation tests. *J Mech Behav Biomed Mater.* 2017;69:50-56. doi:10.1016/j.jmbbm.2016.12.022.
87. Khokhlova AD, Iribe G. Transmural Differences in Mechanical Properties of Isolated Subendocardial and Subepicardial Cardiomyocytes. *Bull Exp Biol Med.* 2016;162(1):48-50. doi:10.1007/s10517-016-3542-8.
88. Kim HJ, Vignon-Clementel IE, Figueroa CA, et al. On coupling a lumped parameter heart model and a three-dimensional finite element aorta model. *Ann Biomed Eng.* 2009;37(11):2153-2169. doi:10.1007/s10439-009-9760-8.
89. Kim J, Baek S. Circumferential variations of mechanical behavior of the porcine thoracic aorta during the inflation test. *J Biomech.* 2011:submitted. doi:10.1016/j.jbiomech.2011.04.022.
90. Kim J, Hong JW, Baek S. Longitudinal differences in the mechanical properties of the thoracic aorta depend on circumferential regions. *J Biomed Mater Res - Part A.* 2013;101A(5):1525-1529. doi:10.1002/jbm.a.34445.
91. Klima U, Ringes-Lichtenberg S, Warnecke G, Lichtenberg A, Struber M, Haverich A. Severe right heart failure after heart transplantation. A single-center experience. *Transpl Int.* 2005;18(3):326-332. doi:10.1111/j.1432-2277.2004.00059.x.
92. Kohn JC, Lampi MC, Reinhart-King CA. Age-related vascular stiffening: Causes and consequences. *Front Genet.* 2015;6(MAR). doi:10.3389/fgene.2015.00112.
93. Kraigher-Krainer E, Shah AM, Gupta DK, et al. Impaired systolic function by strain imaging in heart failure with preserved ejection fraction. *J Am Coll Cardiol.* 2014;63(5):447-455. doi:10.1016/j.jacc.2013.09.052.
94. Ky B, French B, May Khan A, et al. Ventricular-arterial coupling, remodeling, and prognosis in chronic heart failure. *J Am Coll Cardiol.* 2013;62(13):1165-1172. doi:10.1016/j.jacc.2013.03.085.
95. LaDisa JF, Dholakia RJ, Figueroa CA, et al. Computational simulations demonstrate altered wall shear stress in aortic coarctation patients treated by resection with end-to-end anastomosis. *Congenit Heart Dis.* 2011;6(5):432-443. doi:10.1111/j.1747-0803.2011.00553.x.
96. Lam CSP, Donal E, Kraigher-Krainer E, Vasan RS. Epidemiology and clinical course of heart failure with preserved ejection fraction. *Eur J Heart Fail.* 2011;13(1):18-28. doi:10.1093/eurjhf/hfq121.
97. Lampert BC, Teuteberg JJ. STATE OF ART Right ventricular failure after left ventricular assist devices. *J Hear Lung Transplant.* 2015;34:1123-1130. doi:10.1016/j.healun.2015.06.015.

98. Land S, Remedios CG, Holohan S, Smith NP, Kentish JC, Niederer SA. A model of cardiac contraction based on novel measurements of tension development in human cardiomyocytes. *J Mol Cell Cardiol.* 2017;106:1-23. doi:10.1016/j.yjmcc.2017.03.008.
99. Lau KD, Figueroa CA. Simulation of short-term pressure regulation during the tilt test in a coupled 3D–0D closed-loop model of the circulation. *Biomech Model Mechanobiol.* 2015;14(4):915-929. doi:10.1007/s10237-014-0645-x.
100. Lee LC, Genet · M, Acevedo-Bolton G, et al. A computational model that predicts reverse growth in response to mechanical unloading. *Biomech Model Mechanobiol.* 2015;14(2):217-229. doi:10.1007/s10237-014-0598-0.
101. Lee LC, Sundnes J, Genet M, Wenk JF, Wall ST. An integrated electromechanical-growth heart model for simulating cardiac therapies. *Biomech Model Mechanobiol.* 2016;15(4):791-803. doi:10.1007/s10237-015-0723-8.
102. Lee LC, Wall ST, Genet M, Hinson A, Guccione JM. Bioinjection treatment: Effects of post-injection residual stress on left ventricular wall stress. *J Biomech.* 2014. doi:10.1016/j.jbiomech.2014.06.026.
103. Lee LC, Wenk JF, Zhong L, et al. Analysis of patient-specific surgical ventricular restoration: importance of an ellipsoidal left ventricular geometry for diastolic and systolic function. *J Appl Physiol.* 2013;115(1):136-144. doi:10.1152/jappphysiol.00662.2012.
104. Li AE, Kamel I, Rando F, et al. Using MRI to Assess Aortic Wall Thickness in the Multiethnic Study of Atherosclerosis: Distribution by Race, Sex, and Age. *Am J Roentgenol.* 2004;182(3):593-597. doi:10.2214/ajr.182.3.1820593.
105. Lim KM, Constantino J, Gurev V, Zhu R, Shim EB, Trayanova NA. Comparison of the effects of continuous and pulsatile left ventricular-assist devices on ventricular unloading using a cardiac electromechanics model. *J Physiol Sci.* 2012;62(1):11-19. doi:10.1007/s12576-011-0180-9.
106. Lin K, Meng L, Collins JD, Chowdhary V, Markl M, Carr JC. Reproducibility of cine displacement encoding with stimulated echoes (DENSE) in human subjects. *Magn Reson Imaging.* 2016. doi:10.1016/j.mri.2016.08.009.
107. Liu J, Masurekar MR, Vatner DE, et al. Glycation end-product cross-link breaker reduces collagen and improves cardiac function in aging diabetic heart. *Am J Physiol Heart Circ Physiol.* 2003. doi:10.1152/ajpheart.00516.2003.
108. Luo C, Ramachandran D, Ware DL, Ma TS, Clark JW. Modeling left ventricular diastolic dysfunction: Classification and key indicators. *Theor Biol Med Model.* 2011. doi:10.1186/1742-4682-8-14.
109. MacIver DH, Townsend M. A novel mechanism of heart failure with normal ejection fraction. *Heart.* 2008. doi:10.1136/hrt.2006.114082.

110. Mao SS, Ahmadi N, Shah B, et al. Normal Thoracic Aorta Diameter on Cardiac Computed Tomography in Healthy Asymptomatic Adults. *Acad Radiol*. 2008;15(7):827-834. doi:10.1016/j.acra.2008.02.001.
111. Marcus JT, Vonk Noordegraaf A, Roeleveld RJ, et al. Impaired left ventricular filling due to right ventricular pressure overload in primary pulmonary hypertension: noninvasive monitoring using MRI. *Chest*. 2001;119(6):1761-1765. <http://www.ncbi.nlm.nih.gov/pubmed/11399703>. Accessed February 14, 2019.
112. Maurer MS, King DL, El-Khoury Rumbarger L, Packer M, Burkhoff D. Left heart failure with a normal ejection fraction: Identification of different pathophysiologic mechanisms. *J Card Fail*. 2005;11(3):177-187. doi:10.1016/j.cardfail.2004.10.006.
113. McKay RG, Aroesty JM, Heller G V, Royal HD, Warren SE, Grossman W. Assessment of the end-systolic pressure-volume relationship in human beings with the use of a time-varying elastance model. *Circulation*. 1986;74(1):97-104. doi:10.1161/01.CIR.74.1.97.
114. Mello J de, Orsi A, Padovani C. Structure of the aortic wall in the guinea pig and rat. *Braz J Morphol ....* 2004;21:35-38. <http://jms.org.br/PDF/v21n1a06.pdf>.
115. Moazami N, Pasque MK, Moon MR, et al. Mechanical support for isolated right ventricular failure in patients after cardiectomy. *J Hear Lung Transplant*. 2004;23(12):1371-1375. doi:10.1016/j.healun.2003.09.022.
116. Mondillo S, Galderisi M, Mele D, et al. Speckle-tracking echocardiography: a new technique for assessing myocardial function. *J Ultrasound Med*. 2011;30(1):71-83.
117. Moore CC, Lugo-Olivieri CH, McVeigh ER, Zerhouni EA. Three-dimensional systolic strain patterns in the normal human left ventricle: characterization with tagged MR imaging. *Radiology*. 2000;214(2):453-466. doi:10.1148/radiology.214.2.r00fe17453.
118. Morris DA, Ma X-X, Belyavskiy E, et al. Left ventricular longitudinal systolic function analysed by 2D speckle-tracking echocardiography in heart failure with preserved ejection fraction: a meta-analysis. *Open Hear*. 2017;4(2). doi:10.1136/openhrt-2017-000630.
119. Muraru D, Maffessanti F, Kocabay G, et al. Ascending aorta diameters measured by echocardiography using both leading edge-to-leading edge and inner edge-to-inner edge conventions in healthy volunteers. *Eur Heart J Cardiovasc Imaging*. 2014;15(4):415-422. doi:10.1093/ehjci/jet173.
120. Naeije R, Manes A. The right ventricle in pulmonary arterial hypertension. *Eur Respir Rev*. 2014. doi:10.1183/09059180.00007414.
121. Niederer SA, Smith NP. The Role of the Frank-Starling Law in the Transduction of Cellular Work to Whole Organ Pump Function: A Computational Modeling Analysis. *PLoS Comput Biol*. 2009;5(4). doi:10.1371/journal.pcbi.1000371.
122. Notomi Y, Lysyansky P, Setser RM, et al. Measurement of ventricular torsion by two-

- dimensional ultrasound speckle tracking imaging. *J Am Coll Cardiol*. 2005;45(12):2034-2041. doi:10.1016/j.jacc.2005.02.082.
123. Owan TE, Hodge DO, Herges RM, Jacobsen SJ, Roger VL, Redfield MM. Trends in prevalence and outcome of heart failure with preserved ejection fraction. *N Engl J Med*. 2006;355(3):251-259. doi:10.1056/NEJMoa052256.
  124. Pezzuto S, Ambrosi D. Active contraction of the cardiac ventricle and distortion of the microstructural architecture. *Int j numer method biomed eng*. 2014;30(12):1578-1596. doi:10.1002/cnm.2690.
  125. Pezzuto S, Ambrosi D, Quarteroni A. An orthotropic active-strain model for the myocardium mechanics and its numerical approximation. *Eur J Mech A/Solids*. 2014;48(1):83-96. doi:10.1016/j.euromechsol.2014.03.006.
  126. Ponikowski P, Voors AA, Anker SD, et al. 2016 ESC Guidelines for the diagnosis and treatment of acute and chronic heart failure. *Eur Heart J*. 2016;37(27):2129-2200m. doi:10.1093/eurheartj/ehw128.
  127. Provost J, Gurev V, Trayanova N, Konofagou EE. Mapping of cardiac electrical activation with electromechanical wave imaging: An in silico–in vivo reciprocity study. *Heart Rhythm*. 2011;8(5):752-759. doi:10.1016/j.hrthm.2010.12.034.
  128. Punnoose L, Burkhoff D, Rich S, Horn EM. Right ventricular assist device in end-stage pulmonary arterial hypertension: Insights from a computational model of the cardiovascular system. *Prog Cardiovasc Dis*. 2012. doi:10.1016/j.pcad.2012.07.008.
  129. Rain S, Handoko ML, Trip P, et al. Right ventricular diastolic impairment in patients with pulmonary arterial hypertension. *Circulation*. 2013;128(18):2016-2025, 1-10. doi:10.1161/CIRCULATIONAHA.113.001873.
  130. Rajdev S, Benza R, Misra V. Use of Tandem Heart as a temporary hemodynamic support option for severe pulmonary artery hypertension complicated by cardiogenic shock. *J Invasive Cardiol*. 2007;19(8):E226-9. <http://www.ncbi.nlm.nih.gov/pubmed/17712211>. Accessed February 13, 2019.
  131. Reddy YNV, Andersen MJ, Obokata M, et al. Arterial Stiffening With Exercise in Patients With Heart Failure and Preserved Ejection Fraction. *J Am Coll Cardiol*. 2017. doi:10.1016/j.jacc.2017.05.029.
  132. Reichel N. Right ventricular strain in pulmonary hypertension: flavor du jour or enduring prognostic index? *Circ Cardiovasc Imaging*. 2013;6(5):609-611. doi:10.1161/CIRCIMAGING.113.000936.
  133. Rice JJ, Wang F, Bers DM, de Tombe PP. Approximate model of cooperative activation and crossbridge cycling in cardiac muscle using ordinary differential equations. *Biophys J*. 2008;95(5):2368-2390. doi:10.1529/biophysj.107.119487.

134. Roach MR, Burton AC. The reason for the shape of the distensibility curves of arteries. *Can J Biochem Physiol.* 1957;35(8):681-690. <http://www.ncbi.nlm.nih.gov/pubmed/13460788>. Accessed November 13, 2017.
135. Roh J, Houstis N, Rosenzweig A. Why Don't We Have Proven Treatments for HFpEF? *Circ Res.* 2017;120(8):1243-1245. doi:10.1161/CIRCRESAHA.116.310119.
136. Rosenzweig EB, Chicotka S, Bacchetta M. Right ventricular assist device use in ventricular failure due to pulmonary arterial hypertension: Lessons learned. *J Hear Lung Transplant.* 2016;35(10):1272-1274. doi:10.1016/j.healun.2016.07.010.
137. Rosero EB, Peshock RM, Khera A, Claggett P, Lo H, Timaran CH. Sex, race, and age distributions of mean aortic wall thickness in a multiethnic population-based sample. *J Vasc Surg.* 2011;53(4):950-957. doi:10.1016/j.jvs.2010.10.073.
138. Schlatmann TJM, Becker AE. Histologic changes in the normal aging aorta: Implications for dissecting aortic aneurysm. *Am J Cardiol.* 1977;39(1):13-20. doi:10.1016/S0002-9149(77)80004-0.
139. Schriebl AJ, Zeindlinger G, Pierce DM, Regitnig P, Holzapfel GA. Determination of the layer-specific distributed collagen fibre orientations in human thoracic and abdominal aortas and common iliac arteries. *J R Soc Interface.* 2012;9(71):1275-1286. doi:10.1098/rsif.2011.0727.
140. Sengupta PP, Marwick TH. The Many Dimensions of Diastolic Function: A Curse or a Blessing? *JACC Cardiovasc Imaging.* 2018. doi:10.1016/j.jcmg.2017.05.015.
141. Shah AM. Ventricular remodeling in heart failure with preserved ejection fraction. *Curr Heart Fail Rep.* 2013;10(4):341-349. doi:10.1007/s11897-013-0166-4.
142. Shah AM, Claggett B, Sweitzer NK, et al. Prognostic Importance of Changes in Cardiac Structure and Function in Heart Failure With Preserved Ejection Fraction and the Impact of Spironolactone. *Circ Hear Fail.* 2015. doi:10.1161/CIRCHEARTFAILURE.115.002249.
143. Shavik SM, Jiang Z, Baek S, Lee LC. High spatial resolution multi-organ finite element modeling of ventricular-arterial coupling. *Front Physiol.* 2018;9:119. doi:10.3389/FPHYS.2018.00119.
144. Shavik SM, Wall ST, Sundnes J, Burkhoff D, Lee LC. Organ-level validation of a cross-bridge cycling descriptor in a left ventricular finite element model: Effects of ventricular loading on myocardial strains. *Physiol Rep.* 2017;5(21):e13392. doi:10.14814/phy2.13392.
145. Shavik SM, Wall ST, Sundnes J, Burkhoff D, Lee LC. Organ-level validation of a cross-bridge cycling descriptor in a left ventricular finite element model: effects of ventricular loading on myocardial strains. *Physiol Rep.* 2017;5(21). <http://physreports.physiology.org/content/5/21/e13392.abstract>.

146. Shimoda LA, Laurie SS. Vascular remodeling in pulmonary hypertension. *J Mol Med (Berl)*. 2013;91(3):297-309. doi:10.1007/s00109-013-0998-0.
147. Smiseth OA, Torp H, Opdahl A, Haugaa KH, Urheim S. Myocardial strain imaging: how useful is it in clinical decision making? *Eur Heart J*. 2015;37(15):1196-1207. doi:10.1093/eurheartj/ehv529.
148. Smith BW, Chase JG, Nokes RI, Shaw GM, Wake G. Minimal haemodynamic system model including ventricular interaction and valve dynamics. *Med Eng Phys*. 2004;26(2):131-139. doi:10.1016/j.medengphy.2003.10.001.
149. Smulyan H, Safar ME. Systolic blood pressure revisited. *J Am Coll Cardiol*. 1997;29(7):1407-1413.
150. Solomon SD, Zile M, Pieske B, et al. The angiotensin receptor neprilysin inhibitor LCZ696 in heart failure with preserved ejection fraction: A phase 2 double-blind randomised controlled trial. *Lancet*. 2012. doi:10.1016/S0140-6736(12)61227-6.
151. Somaratne JB, Berry C, McMurray JJ V, Poppe KK, Doughty RN, Whalley GA. The prognostic significance of heart failure with preserved left ventricular ejection fraction: A literature-based meta-analysis. *Eur J Heart Fail*. 2009;11(9):855-862. doi:10.1093/eurjhf/hfp103.
152. Strauer BE. Left ventricular systolic wall stress as a primary determinant of myocardial oxygen consumption : Comparative studies in patients with normal left ventricular function , with pressure and volume overload and with coronary heart disease \*)  
Vergleichende Un. 1977;3:8-10.
153. Streeter DD, Spotnitz HM, Patel DP, Ross J, Sonnenblick EH. Fiber orientation in the canine left ventricle during diastole and systole. *Circ Res*. 1969;24(3):339-347. doi:10.1161/01.RES.24.3.339.
154. Su MYM, Lin LY, Tseng YHE, et al. CMR-verified diffuse myocardial fibrosis is associated with diastolic dysfunction in HFpEF. *JACC Cardiovasc Imaging*. 2014;7(10):991-997. doi:10.1016/j.jcmg.2014.04.022.
155. Suga H, Hayashi T, Shirahata M. Ventricular systolic pressure-volume area as predictor of cardiac oxygen consumption. *Am J Physiol*. 1981;240:H39-H44.
156. Sundnes J, Wall S, Osnes H, Thorvaldsen T, McCulloch a D. Improved discretisation and linearisation of active tension in strongly coupled cardiac electro-mechanics simulations. *Comput Methods Biomech Biomed Engin*. 2012;(March 2013):37-41. doi:10.1080/10255842.2012.704368.
157. Tartire-Kesri L, Tartire JM, Logeart D, Beauvais F, Cohen Solal A. Increased proximal arterial stiffness and cardiac response with moderate exercise in patients with heart failure and preserved ejection fraction. *J Am Coll Cardiol*. 2012. doi:10.1016/j.jacc.2011.10.873.

158. Van Tassell BW, Arena R, Biondi-Zoccai G, et al. Effects of Interleukin-1 Blockade With Anakinra on Aerobic Exercise Capacity in Patients With Heart Failure and Preserved Ejection Fraction (from the D-HART Pilot Study). *Am J Cardiol.* 2014. doi:10.1016/j.amjcard.2013.08.047.
159. Towfiq BA, Weir J, Rawles JM. Effect of age and blood pressure on aortic size and stroke distance. *Br Heart J.* 1986;55(6):560-568. <http://www.pubmedcentral.nih.gov/articlerender.fcgi?artid=1236762&tool=pmcentrez&rendertype=abstract>.
160. Trayanova NA, Constantino J, Gurev V. Electromechanical models of the ventricles. *AJP Hear Circ Physiol.* 2011;301(2):H279-H286. doi:10.1152/ajpheart.00324.2011.
161. Tribouilloy C, Rusinaru D, Mahjoub H, et al. Prognosis of heart failure with preserved ejection fraction: A 5 year prospective population-based study. *Eur Heart J.* 2008;29(3):339-347. doi:10.1093/eurheartj/ehm554.
162. Trip P, Rain S, Handoko ML, et al. Clinical relevance of right ventricular diastolic stiffness in pulmonary hypertension. *Eur Respir J.* 2015;45(6):1603-1612. doi:10.1183/09031936.00156714.
163. Tsamis A, Krawiec JT, Vorp DA. Elastin and collagen fibre microstructure of the human aorta in ageing and disease: a review. *J R Soc Interface.* 2013;10(83):20121004. doi:10.1098/rsif.2012.1004.
164. Usyk TP, LeGrice IJ, McCulloch AD. Computational model of three-dimensional cardiac electromechanics. *Comput Vis Sci.* 2002;4(4):249-257. doi:10.1007/s00791-002-0081-9.
165. Vasava P, Jalali P, Dabagh M, Kolari PJ. Finite element modelling of pulsatile blood flow in idealized model of human aortic arch: Study of hypotension and hypertension. *Comput Math Methods Med.* 2012;2012. doi:10.1155/2012/861837.
166. Velagaleti RS, Gona P, Pencina MJ, et al. Left ventricular hypertrophy patterns and incidence of heart failure with preserved versus reduced ejection fraction. *Am J Cardiol.* 2014;113(1):117-122. doi:10.1016/j.amjcard.2013.09.028.
167. Walker JC, Ratcliffe MB, Zhang P, et al. MRI-based finite-element analysis of left ventricular aneurysm. *Am J Physiol Circ Physiol.* 2005;289(2):H692-H700. doi:10.1152/ajpheart.01226.2004.
168. Wall ST, Guccione JM, Ratcliffe MB, Sundnes JS. Electromechanical feedback with reduced cellular connectivity alters electrical activity in an infarct injured left ventricle: a finite element model study. *AJP Hear Circ Physiol.* 2012;302(1):H206-H214. doi:10.1152/ajpheart.00272.2011.
169. Wang J, Khoury DS, Yue Y, Torre-Amione G, Nagueh SF. Preserved left ventricular twist and circumferential deformation, but depressed longitudinal and radial deformation in patients with diastolic heart failure. *Eur Heart J.* 2008;29(10):1283-1289.

doi:10.1093/eurheartj/ehn141.

170. Wannenburg T, Schulman SP, Burkhoff D. End-systolic pressure-volume and MVO<sub>2</sub>-pressure-volume area relations of isolated rat hearts. *Am J Physiol Heart Circ Physiol*. 1992;262:1287-1293.
171. Wenk JF, Klepach D, Lee LC, et al. First evidence of depressed contractility in the border zone of a human myocardial infarction. *Ann Thorac Surg*. 2012;93(4):1188-1193. doi:10.1016/j.athoracsur.2011.12.066.
172. Wenk JF, Sun K, Zhang Z, et al. Regional Left Ventricular Myocardial Contractility and Stress in a Finite Element Model of Posterobasal Myocardial Infarction. *J Biomech Eng*. 2011;133(4):044501. doi:10.1115/1.4003438.
173. Winslow RL, Rice J, Jafri S, Marba E, Rourke BO. Mechanisms of Altered Excitation-Contraction Coupling in Canine Tachycardial-Induced Heart Failure, II: Model Studies. *Circ Res*. 1999;84:571-586.
174. Xi C, Latnie C, Zhao X, et al. Patient-Specific Computational Analysis of Ventricular Mechanics in Pulmonary Arterial Hypertension. *J Biomech Eng*. 2016;138(11):111001. doi:10.1115/1.4034559.
175. Yamagami K, Oka T, Wang Q, et al. Pirfenidone Exhibits Cardioprotective Effects by Regulating Myocardial Fibrosis and Vascular Permeability in Pressure Overloaded Hearts. *Am J Physiol Heart Circ Physiol*. 2015. doi:10.1152/ajpheart.00137.2015.
176. Yancy CW, Lopatin M, Stevenson LW, De Marco T, Fonarow GC. Clinical presentation, management, and in-hospital outcomes of patients admitted with acute decompensated heart failure with preserved systolic function: A report from the Acute Decompensated Heart Failure National Registry (ADHERE) database. *J Am Coll Cardiol*. 2006. doi:10.1109/DTIS.2013.6527774.
177. Zeinali-Davarani S, Sheidaei A, Baek S. A finite element model of stress-mediated vascular adaptation: application to abdominal aortic aneurysms. *Comput Methods Biomech Biomed Engin*. 2011:in print.
178. Zile MR, Baicu CF, Gaasch WH. Diastolic Heart Failure — Abnormalities in Active Relaxation and Passive Stiffness of the Left Ventricle. *N Engl J Med*. 2004;350(19):1953-1959. doi:10.1056/NEJMoa032566.
179. Zile MR, Gaasch WH, Carroll JD, et al. Heart failure with a normal ejection fraction: is measurement of diastolic function necessary to make the diagnosis of diastolic heart failure? *Circulation*. 2001;104:779-782. doi:10.1161/hc3201.094226.
180. Zou H, Xi C, Zhao X, et al. Quantification of Biventricular Strains in Heart Failure With Preserved Ejection Fraction Patient Using Hyperelastic Warping Method. *Front Physiol*. 2018;9:1295. doi:10.3389/fphys.2018.01295.

